Spring 2020

Imaging in karst terrain using the Electrical Resistivity Tomography (ERT) and Multi-Channel Analysis of Surface Waves (MASW) methods

Hassan Abdullah Alzahrani

Department: Geosciences and Geological and Petroleum Engineering

IMAGING IN KARST TERRAIN USING THE ELECTRICAL RESISTIVITY TOMOGRAPHY (ERT) AND MULTI-CHANNEL ANALYSIS OF SURFACE WAVES (MASW) METHODS

by

HASSAN ABDULLAH ALZAHRANI

A DISSERTATION

Presented to the Faculty of the Graduate School of the

MISSOURI UNIVERSITY OF SCIENCE AND TECHNOLOGY

In Partial Fulfillment of the Requirements for the Degree

DOCTOR OF PHILOSOPHY

in

GEOLOGICAL ENGINEERING

2020

Approved by:

Neil L. Anderson, Advisor
J David Rogers
Evgeniy Torgashov
Stephen S. Gao
Kelly H Liu

ABSTRACT

Electrical Resistivity Tomography (ERT) and Multi-channel Analysis of Surface Waves (MASW) methods were used to image the subsurface in karst terrain in the southeast of Missouri. A SuperSting R8 system was used to acquire the ERT profiles; a multi-channel engineering seismograph was used to acquire the MASW data. The latter data were used to constrain and verify the ERT interpreted depth to top-of-rock and soil thickness. The ERT data were used to delineate the soil/rock interface and to identify zones of anomalously high moisture content within the bedrock.

The primary objective of the research was to determine the cause of identified zones of high moisture content within the bedrock and to differentiate anomalously conductive zones that were mostly "man-made" from those that were mostly of "natural" origin. Field observations and air photographs were used for this purpose.

Herein, seven ERT profiles are presented. Five (5) of the low resistivity bedrock anomalies identified on these ERT profiles are classified as primarily "man-made"; the other four (4) are classified as primarily "natural" in origin. Based on the assessment of the entire ERT data set, it is concluded that there are no significant statistical differences between the ERT signatures of the "man-made" and "natural" zones of high moisture content. Determinations about the cause of low resistivity zones identified on ERT data is best done based on field observations and air photographs.

ACKNOWLEDGMENTS

My sincere thanks and gratitude to my advisor, Dr. Neil Anderson. Dr. Anderson never stopped encouraging me and advising me throughout the years I spent registered in the geological engineering PhD program at Missouri S&T.

I am also very thankful to my committee members, Dr. J. R. Rogers, Dr. Stephen Gao, Dr. Kelly Liu, and Dr. Evgeniy Torgashov, for their much-appreciated advice and support.

I would like to extend special appreciation to my lovely family. It is a unique experience to have my kids and wife with me while pursuing graduate studies. It is not simple or easy for an entire family to live with academic ups and downs and to keep being supportive. I appreciate what every member of my immediate family and my extended family did to help me to achieve this accomplishment.

Thanks for all those who made it possible for me to achieve my goals.

TABLE OF CONTENTS

Page

LIST OF ILLUSTRATIONS

LIST OF TABLES

Page

1. INTRODUCTION

Electrical resistivity tomography (ERT) and multi-channel analysis of surface waves (MASW) have proven to be indispensable geophysical technologies for studying regions dominated by carbonate rocks, such as in the southern Missouri region. These techniques provide reliable results and save time and money (Al Saaideh, 2017; Nwokebuihe, 2014).

Surface and subsurface water flow are the primary factors that shape the surface and subsurface topography in regions characterized by carbonate rocks. Water flow causes the development of karstic features such as sinkholes, underground drainage systems, cave systems, and solution-widened joints. Karstic features, particularly sinkholes, are known for the significant damage they cause to properties, establishments, and structures; the pollution of groundwater and subsurface soil they facilitate, and the roles they have played in the loss of human life, especially in collapse sinkholes. In order to create safer, long-term roads, dams, buildings, structures, and landfills, karst regions require careful investigation and assessment (Kidanu et al., 2016; Bashir et al., 2018; Bansah & Anderson, 2018; Obi, 2016 and Alfuqara, 2017).

This PhD research includes the use of electrical resistivity tomography (ERT) and multi-channel analysis of surface waves (MASW) methods. The ERT method was used to map subsurface conditions in the study area, including the nature and extent of karst features, seepage pathways, the depth to top-of-rock, soil and rock engineering properties, and soil and rock moisture content and thickness. The primary objective is to identify zones of anomalously high moisture content which have been created due to man-made activities

versus natural causes. The MASW method was used to map the variations in shear strength and the engineering properties of soil and rock. It was used also to constrain and verify the interpretation of the ERT data.

1.1. STUDY OBJECTIVES

1. Differentiate soil and rock based on ERT and MASW data;
2. Map the depth to top-of- rock and soil thicknesses in the study area;
3. Determine the engineering properties (shear-wave velocity) of soil and rock;
4. Map variations of the moisture content in the subsurface;
5. Identify causes of moisture variation in the subsurface;
6. Map seepage pathways in the subsurface;
7. Determine the nature and extent of karst features in the study area; and
8. Differentiate zones of anomalously high moisture content due to man-made activities versus natural causes.

1.2. IMPORTANCE OF THE RESEARCH

1. The study enhances understanding the nature and causes of moisture variations in the subsurface in karst terrain;
2. The research demonstrates the moisture variations are due to both man-made and natural causes;
3. Moisture variations due to man-made or natural causes will be differentiated, if possible;
4. The research confirms that geophysical methods are cost-effective and more

definitive than traditional subsurface investigation methods (boreholes and trenching);

5. Maps the seasonal variations in moisture content; and
6. Demonstrate that these imaging tools can be used to identify areas where karst features could develop.

1.3. PREVIOUS STUDIES

The study area is in Springfield plateau in southwestern Missouri. The plateau consists, in part, of 150 to 270 ft. of Burlington-Keokuk Formation carbonate rock. ERT and MASW are important geophysical techniques used to study subsurface conditions in regions of carbonate rocks. These regions are prone to the development of karstic features that constitute serious hazards and threats to people, property, soil, groundwater, and development (Kidanu et al. 2016., Al Saaideh, 2017; Bansah and Anderson, 2017 and Bashir et al., 2018), (Figure 1.1).

Considering the risks and hazards of karst features, Al Saaideh (2017) conducted a research study of a landfill in southwestern Missouri. ERT and MASW methods were used in this study.

The study identified probable sources of groundwater seepage pathways through and beneath the fly ash landfill and mapped the variations in moisture content above and below the fly ash liners.

The ERT image (Figure 1.2) suggests that some of the run-off from the flanks of the fly ash landfill seep into the soil and rock, primarily near the toe of the landfill along pathway 4.

Figure 1.1. 2006 Photograph of a collapsed sinkhole with a damaged house in Nixa Missouri (Anderson, 2006).

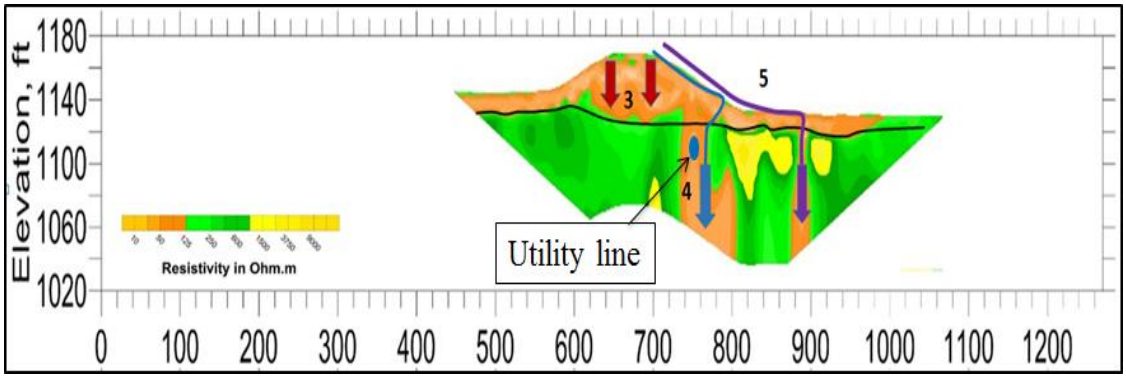

Figure 1.2. Seepage pathways highlighted in red, blue, and purple in a 3D electrical resistivity image of the subsurface along ERT traverse in a study in southeastern Missouri (Al Saaideh, 2017).

The study suggests that moisture seeps into joints in the rock more vertically than horizontally. Zones of high moisture content are characterized by resistivity values less than 125 Ω·m. These zones are generally indicative of very moist, weathered, and/or fractured rock or moist residual soil. The interpretation concluded that there was no

groundwater seepage or flow within or in proximity to the landfill and that there was no potential hazard of groundwater contamination.

Bansah and Anderson (2017) conducted research in southwestern Missouri to determine factors other than the dissolution of carbonates or evaporation of bedrock that could trigger or assist in the formation of sinkhole features. By using ERT, 3D surface terrain models, historical images, and borehole logs, they were able to conclude that anthropogenic activities were the major driving factors for the formation of karst features.

In a similar study, Kidanu et al. (2018) used a GIS-based spatial analysis, site-specific geophysical data (ERT and MASW), and borehole data to identify the physical factors that influence the formation and distribution of sinkholes. Their research determined that the relatively low resistivity values (sinkholes) in their study area are attributed to vertical seepage and associated piping of fine-grained soils through preexisting fractures that are often widened by dissolution. They further suggested that the sinkhole in their study developed along a natural north-south surface drainage pathway and that the subsurface structure of the sinkhole depicts a vertical zone of moisture flow and associated soil piping. From the nature of the overburden material and the characteristics of the sinkhole, they concluded that the sinkhole is predominantly a cover-subsidence sinkhole (gradual subsidence). Kidanu et al.'s (2018) findings of the gradual subsidence sinkhole type were confirmed by Alfuqara (2017) in the same southwestern Missouri region.

In an arid region investigation, Youssef et al. (2016) studied sinkholes that developed in Saudi Arabia during the humid season. These sinkholes were reactivated recently by natural and anthropogenic factors. Urban development encroached into the

natural seasonal channels, causing the diversion of flood waters into low-lying topographies and enhanced seepage of water into the subsurface. El Aal, A. A. (2017) identified and characterized near-surface cavities in the limestone of the Tuwaiq Mountains in Riyadh, KSA.

Expansion in agriculture caused the withdrawal of fossil water from deep aquifers to the surface and urbanization utilized domestic water, which indirectly reactivated the karst formation processes and resulted in sinkhole collapses.

2. STUDY AREA

2.1. LOCATION

The study area is in the southwestern part of Missouri (Figure 2.1). It is part of the Springfield Plateau, which is a sub-province of the Ozark Plateau physiographic region.

Figure 2.1. The study area in Missouri (Google Earth).

2.2. PHYSIOGRAPHIC & GEOLOGICAL SETTING

The study area is in the Springfield Plateau, which is a part of the larger Ozark Plateau (Figure 2.2 and Figure 2.3). The shallow bedrock generally consists of thick Mississippian-age Burlington-Keokuk limestone (Middendorf et al., 1987), which is a

cherty limestone that overlies the Ordovician and Cambrian-aged strata. The strata gently dip westward. The displacements of the faults existing in the area are less than 50 ft. The weathering process widely affected the limestone strata creating irregular surfaces that are covered by the residuum of the cherty clay, which exceeds 40 ft in some locations (Figure 2.4).

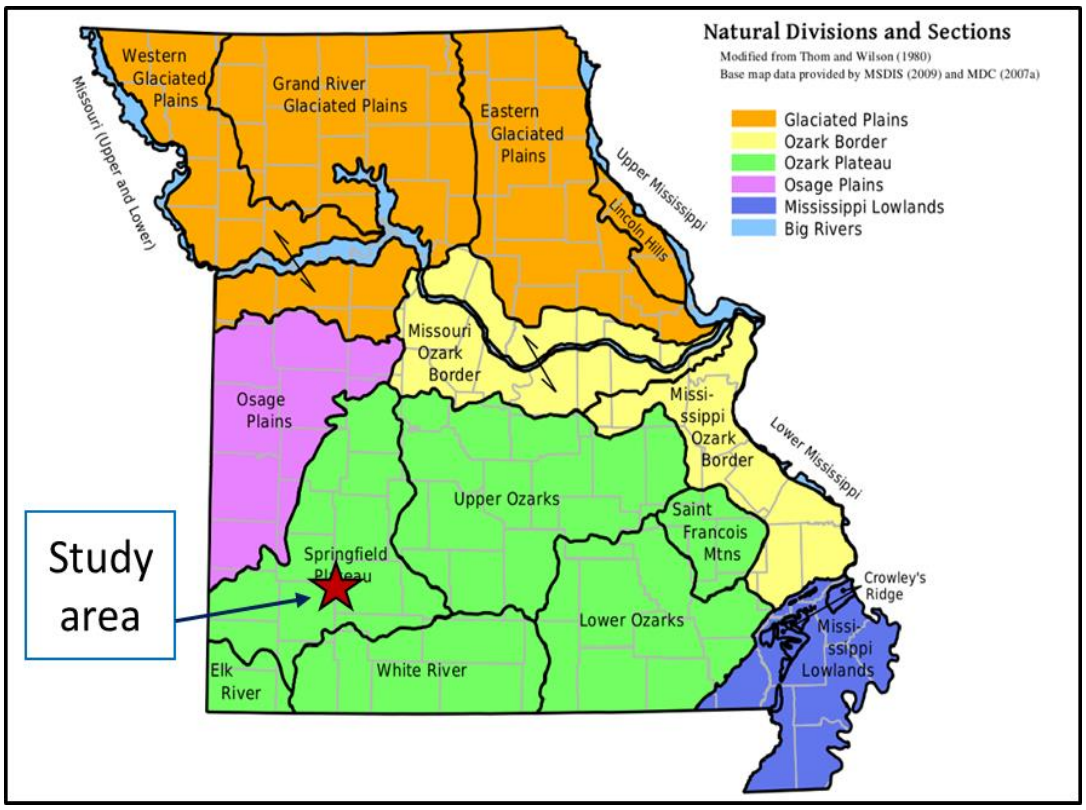

Figure 2.2. Natural divisions and sections of Missouri state (http://www.mdc.state.mo.us/nathis/natcom/natdiv/).

The geology in the study area is described by Middendorf et al. (1987) as pure, shallow marine calcium limestone of organic origin of the Mississippian-aged Burlington-Keokuk, which reaches a thickness of 200 ft and is widely affected by weathering (Figure 2.5 and Figure 2.6).

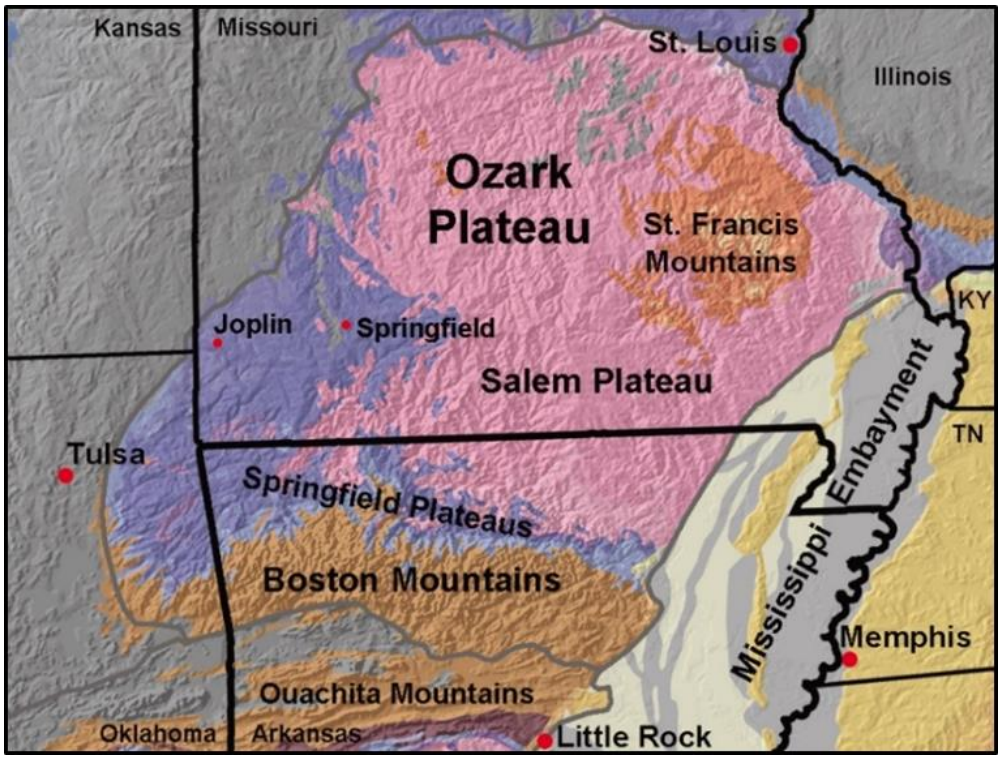

Figure 2.3. The Ozark Plateau sub-divisions (http://gotbooks.miracosta.edu/geology/images2/ozarks.jpg).

Figure 2.4. This figure shows the soil mantle on the weathered bedrock (Anderson, 2016).

Soil in the area was identified as clay residuum. In the area of southwest Springfield, the soil is mapped as cherty clay residuum consisting of clay loam to silty clay loam containing sub-angular to angular fragments of chert, up to one foot in diameter as individual clasts and relict cherty layers (James et al., 1992).

Vandike (1993) summarized the sequence stratigraphy of the formation of the study area. Table 2.1 is detailing the system, series, group, formation, and thickness, indicating that the thickness of Burlington carbonate rocks, which represent the Osagean Series of the Mississippian System top, varies between 150 to 270 ft.

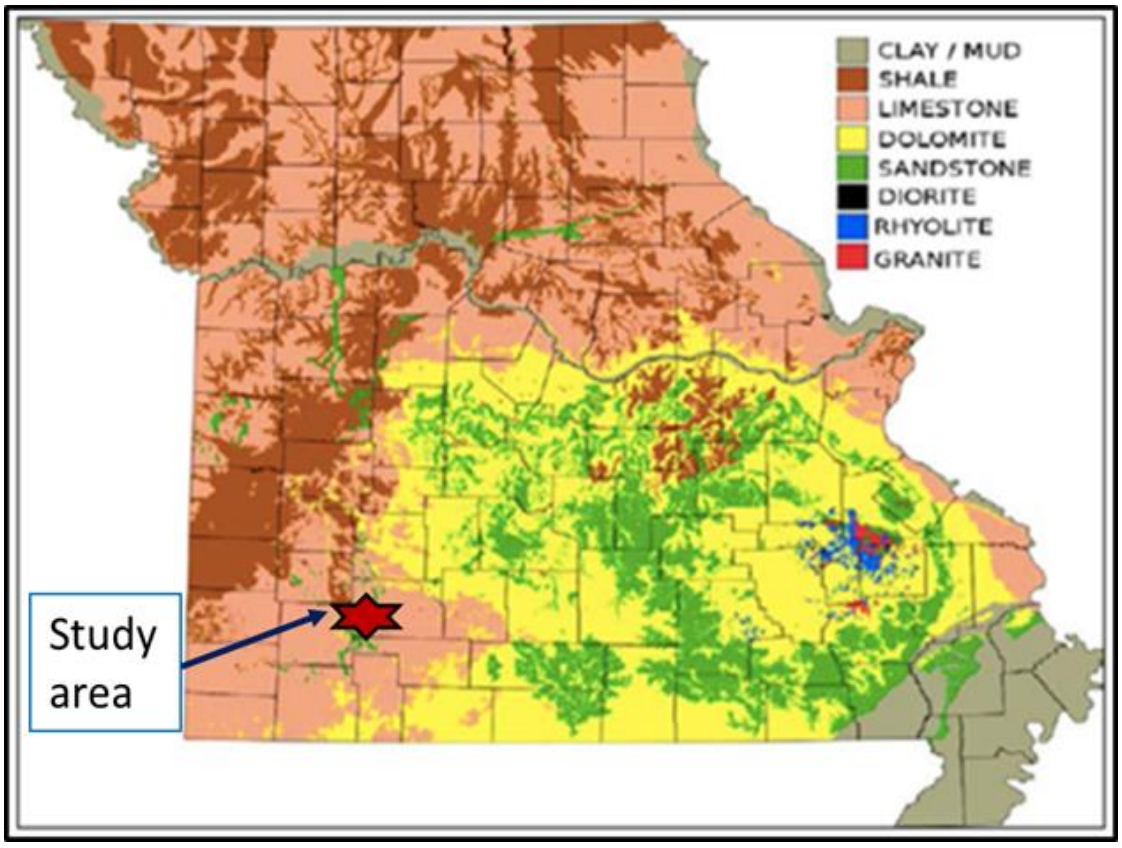

Figure 2.5. Geologic map shows the distribution of different rock units in Missouri. About 59% of the state is underlain by thick carbonate rock units that host a wide variety of karst features. (http://upload.wikimedia.org/wikipedia/commons/a/a1/Missouri_Geology Primary_Rock_Types_v1.png).

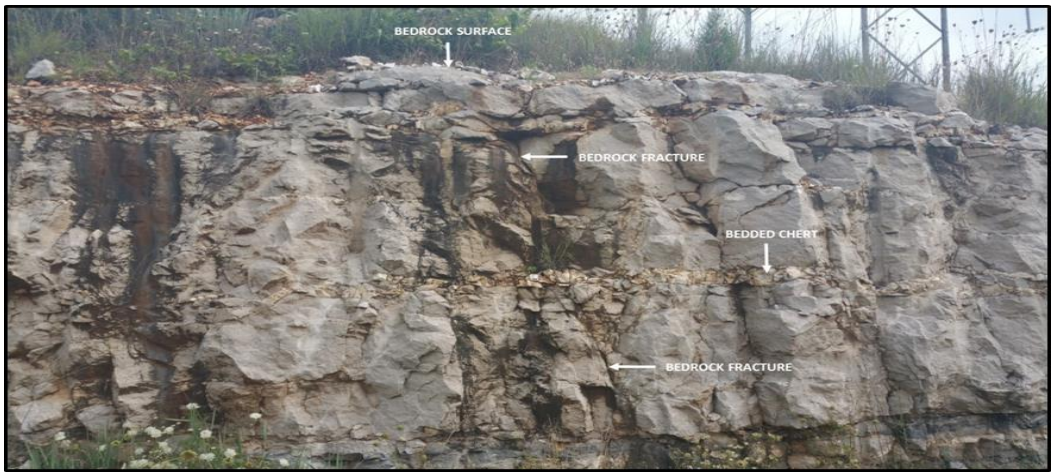

Figure 2.6. The figure shows the cherty clay, near surface thickness and the weathering processes (Anderson, 2016).

2.3. HYDROLOGY OF THE STUDY AREA

The source of groundwater for all aquifers is precipitation. When rain falls, some of it is absorbed by plants and soil, some drains into streams, some evaporates, and the remainder seeps downward into aquifers, recharging them (Figure 2.7). Groundwater moves through the hydrologic cycle as part of a dynamic flow system from recharge areas to discharge areas. Groundwater discharge areas include oceans, streams, lakes, and wetlands. Streams that flow during periods of little rainfall are fed by groundwater. Sinkholes are then formed as the result of the solution or erosion of rocks below groundwater and the collapse or subsidence of subsurface caves, where limestone, marble, dolomite, gypsum, salt and other rocks have been carved and shaped by water.

2.4. FORMATION OF KARST TERRAIN

Karst is described by the Houston Advanced Research Center (Veni, G. et al. 2015) as a unique land formation characterized by springs, caves, and sinkholes formed when carbon dioxide enriched water dissolves limestone and dolomite rock.

Table 2.1. Geologic and stratigraphic units in Greene County (Vandike, 1993).

System	Series	Group	Formation		Thickness (ft)
Mississipian	Osagean		Burlington-Keokuk Formation		150-270
			Elsey Formation		25-75
			Reeds-Spring Formation		125
			Pierson Formation		90
	Kinkerhookian	Chouteau	Northview Formation		5-80
			Compton Formation		30
Ordovician	Canadian		Cotter Formation		600
			Jefferson-City Formation		
			Ruobidoux Formation		150
			Gasconade Formation	Upper Gasconade Dolomite	350
				Lower Gasconade Dolomite	
				Gunter Sandstone Member	25
Cambrian	Upper		Eminence Formation		500
			Potasi Formation		
		Elvins	Derby-Doerun Formation		
			Davis Formation		150
			Bonneterre Formation		200
			Lamotte Formation		150
Precambrian	Crystalline rock				

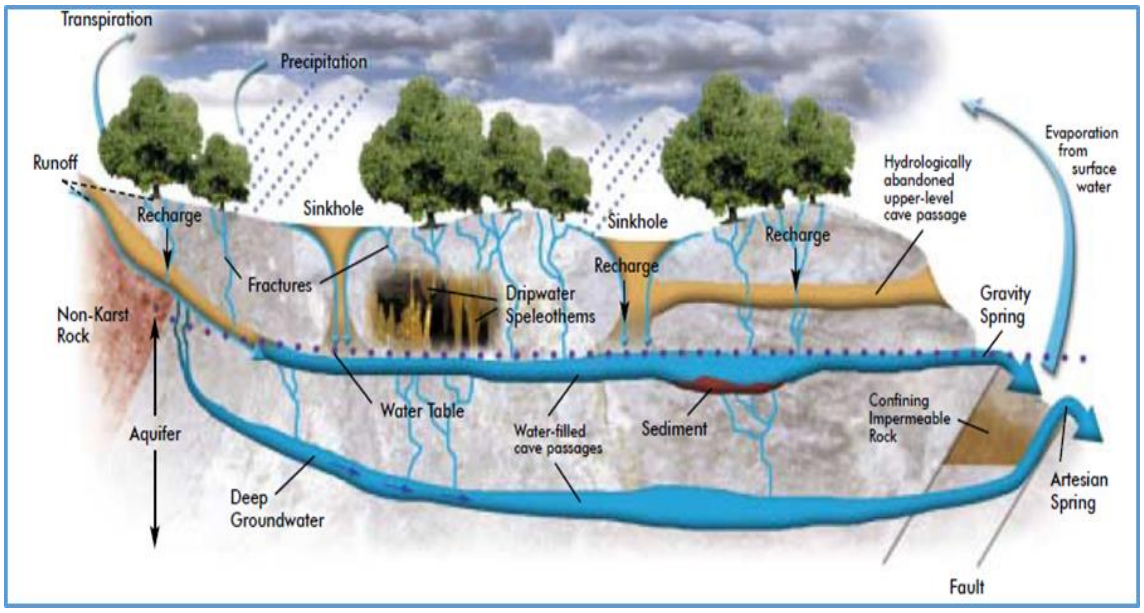

Figure 2.7. Conceptual model, showing hydrologic cycle in karst areas (http://augustacountyalliance.org/wp-content/uploads/2014/09/Augusta-County-Karst-101.pdf).

The development of caves involves acid waters that form when rainwater dissolves carbon dioxide particles in the atmosphere to form weak carbonic acid (partially dissociated acid), which is described by the following equation:

$$\underset{\text{carbon dioxide + water}}{CO_2 + H_2O} \rightleftharpoons \underset{\text{carbonic acid}}{H_2CO_3} \rightleftharpoons \underset{\text{bicarbonate + hydrogen ion}}{HCO_3^- + H^+} \quad (1)$$

The mild acidic water readily dissolves the calcium of the limestone, marble and dolomite and percolates through the surface joints and fractures to reach the groundwater, forming the various features that are recognized as karst features, such as depressions, recessions, basins, pits, and natural wells.

Sinkholes can be created by collapse, the gradual subsidence of a subterranean cavity, or a combination of the two. At some point during the process of cave development,

these caves come very close to the ground's surface and the rock cannot support its own weight, which results in the formation of collapse sinkholes (Figure 2.8).

Another sinkhole formation mode occurs when water from rain or floods percolates into the subsurface and creates small depressions as a result of the removal of surface material (piping). The depressions collect concentrated water and accelerate the dissolution of the carbonate rocks. The dissolved material functions as in-fill material for the subsurface fractures and joints when the clay particle sizes are filtered out of the seeping rainwater (Obi, 2016).

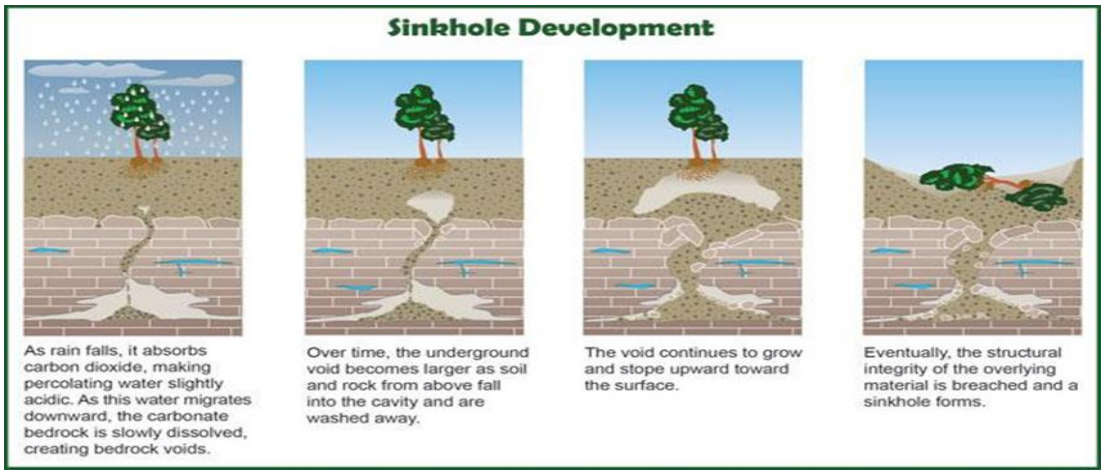

Figure 2.8. Stages of the sinkhole formation process
(Missouri Department of Natural Resources web site).

Through this process of piping, which occurs during the irregular seepage of water due to the existence of natural constraints such as fallen trees or anthropogenic factors such as roads and parking lots, depressions are created, which are considered to be the main factor in creating sinkholes that turn into ponds and wetland (Figure 2.9).

Sinkhole depressions in the Ozark can range from few inches in diameters and a few feet deep to over 1,000 ft wide and over 100 ft deep.

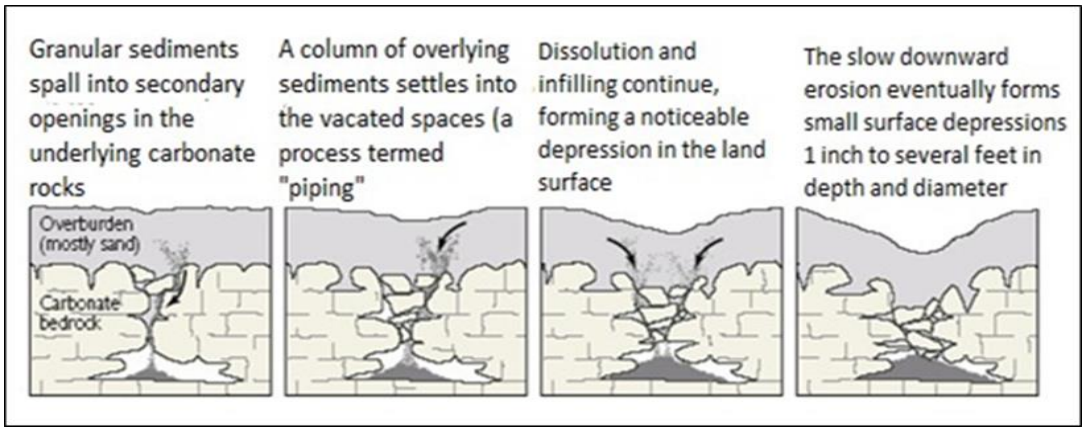

Figure 2.9. Formation of cover-subsidence sinkhole (https://water.usgs.gov/edu/sinkholes.html Cover-subsidence sinkhole).

A study in the Ozarks found that about 95% of all the mapped sinkholes were solutional and less than 5% were collapse sinks (Porter and Thomson, 1975). Due to the commonality and importance of sinkholes in Missouri, the Department of Natural Resources maps and regularly updates these features (Figure 2.10).

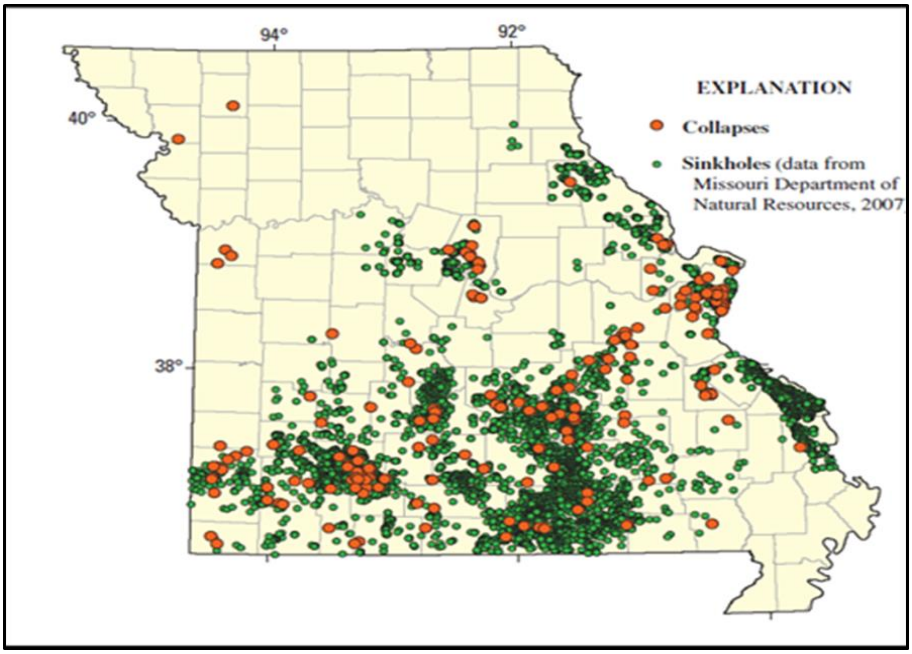

Figure 2.10. The figure shows sinkholes distribution in Missouri (Missouri Department of Natural Resources, 2007).

3. STUDY METHODS

3.1. ELECTRICAL RESISTIVITY TOMOGRAPHY (ERT)

Electrical resistivity tomography emerged from early studies on electrical resistivity properties of rock, soils and fluids.

3.1.1. Theory. The theory and principles are well defined using two to four electrodes to measure subsurface properties. These studies go back to the 1920's but were of very limited use because of the limitation of handling large data. By the advent of powerful computers, near surface geophysical survey's using electrical resistivity methods became possible and these surveys focused on characterizing soils, types of rocks, formation thickness, fracturing, jointing, faulting, contamination, delineating fills, finding voids, and mapping large scale geologic features (http://geophysicalservices.com/electrical-resistivity-tomography-imaging-supersting-ohmmapper-032517/).

The empirical relationship between the resistance (R) of a cylindrical-shaped body of uniform resistance, which receives a current (I) in a simple electric circuit, was derived by George Simon Ohm and is known as Ohm's Law, and is written as:

$$V=IR \tag{1}$$

Ohm's Law is the key principle to the electrical resistivity tomography (ERT), which is described by the environmental protection agency (EPA) as the distribution of electrical potential in the ground surface around a current carrying electrode, which depends on the resistivity and distribution of the surrounding soil and rock (Environmental Protection Agency, 2018) (Figure 3.1).

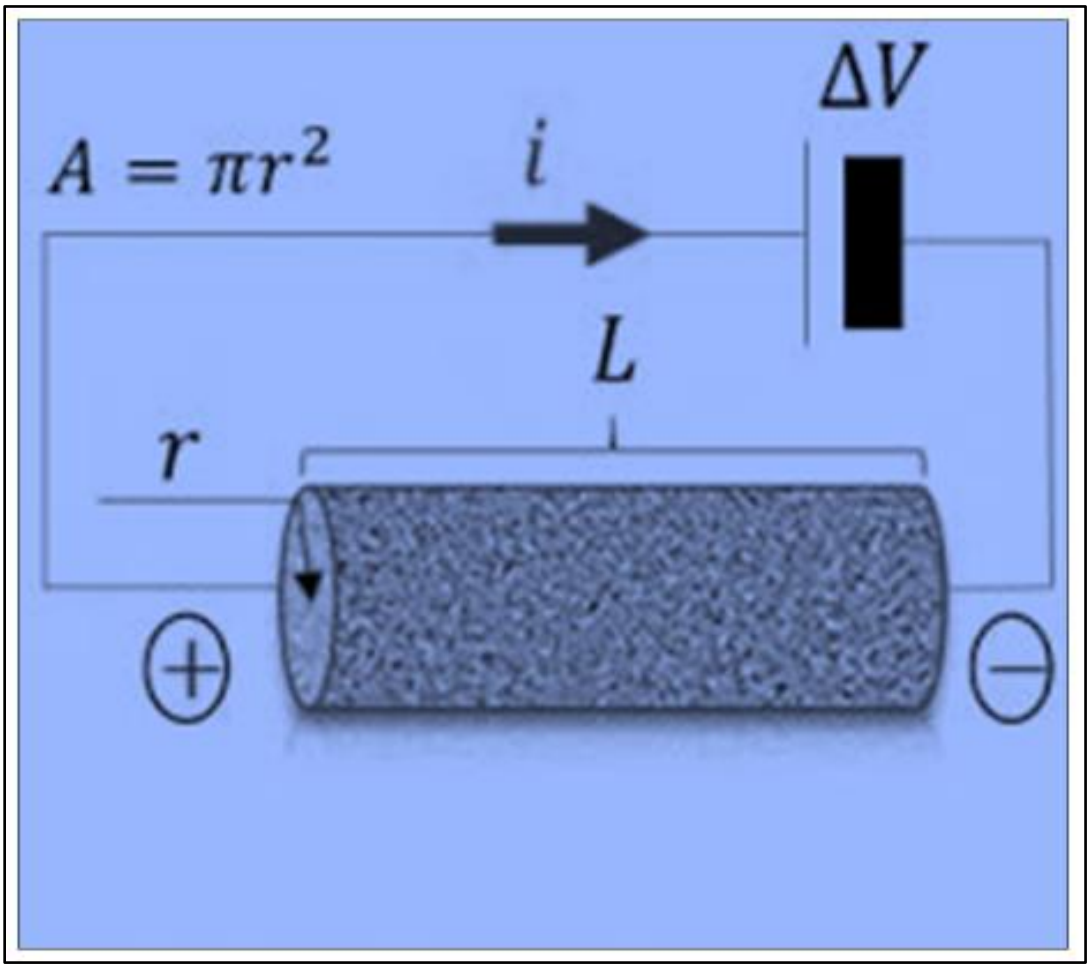

Figure 3.1. Simple electrical circuit illustrating Ohm's Law and the ERT principle (SEG wiki - SEG.org).

This relationship is derived from Ohm's Law, where (*R*) is the resistance of a cylindrical resistor body of uniform resistivity; (*I*) is simple current passing through the cylinder, and (*V*) corresponds to the change in potential, such that:

$$\Delta V = RI \tag{2}$$

By replacing values for ΔV and the current (*I*), the value of resistance *R* could be obtained (Gibson & George, 2003). Another approach is used to obtain the potential difference, using the dissipation of electrical current within infinite homogeneous space. The approach considers that the current travels radially from an origin. Using a radius of

(r) and a surface area of $2\pi^2$ for the current travel distance and equipotential area, respectively, we obtain the resistance at any point from the source as:

$$R = \rho\left(\frac{r}{2\pi r2}\right) = \frac{\rho}{2\pi r}. \quad (3)$$

This resistance is related to Ohm's Law in the form:

$$V = IR = I\left(\frac{\rho}{2\pi r}\right). \quad (4)$$

This above relationship applies to obtaining the potential difference between any two points, provided that the medium is homogeneous. The following equation expresses this relationship:

$$V = I\left[\left(\frac{\rho}{2\pi r1}\right) - \left(\frac{\rho}{2\pi r2}\right)\right] = \left(\frac{I\rho}{2\pi}\right)\left[\left(\frac{1}{r1}\right) - \left(\frac{1}{r2}\right)\right]. \quad (5)$$

The equation could be rewritten in terms of ρ as:

$$\rho = \left(\frac{2\pi V}{I}\right)\left[\frac{1}{\left(\frac{1}{r1}\right) - \left(\frac{1}{r2}\right)}\right]. \quad (6)$$

The resistivity (ρ) we obtain is an apparent resistivity, because it represents the resistivity of homogeneous medium (i.e. theoretical), unlike the heterogeneity of natural earth material.

Practically a direct current is applied between the electrodes that are implanted in the ground to measure the difference of potential between other additional electrodes that do not carry current. The relationship between the distributed potentials and the ground resistivity and their distributions is the basic factor in interpreting the resistivity distributions. The resistivity of soil and rock is governed primarily by the amount of pore water, its resistivity, and the arrangement of the pores. For this reason, there are wide ranges in resistivity for any soil or rock type (Figure 3.2).

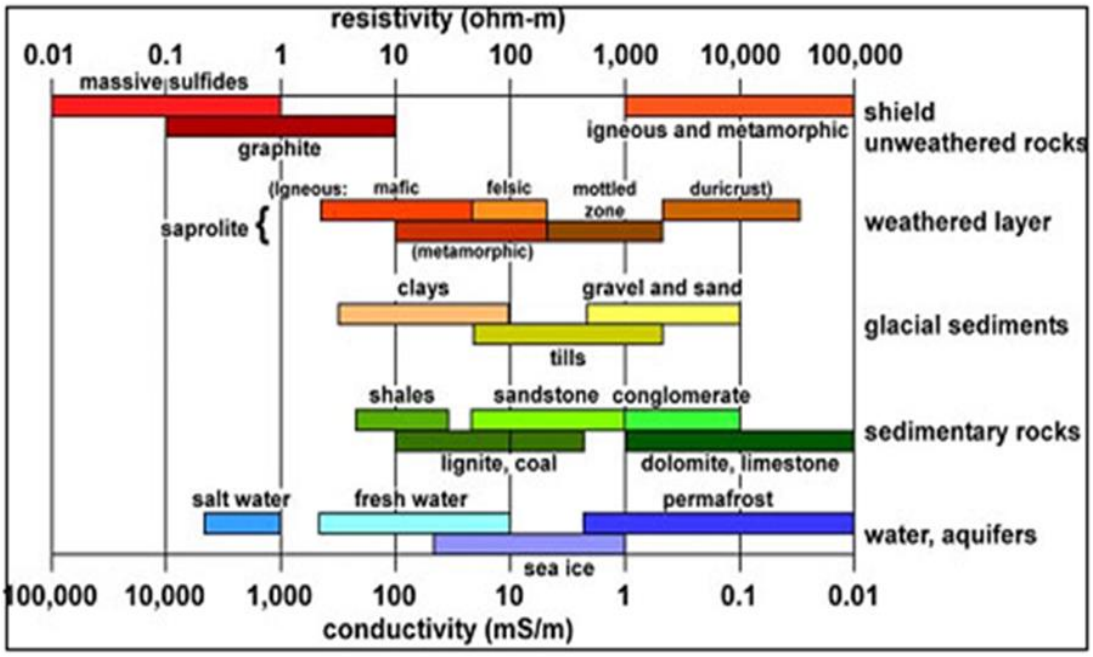

Figure 3.2. Typical range of resistivity of rocks and soils (Palacky, 1988).

Soil type or lithology cannot be directly interpreted form resistivity values, but zones of distinctive resistivity can be associated with specific soil or rock units, based on local field or drill-hole information.

The principle problem of resistivity surveying is the use of apparent resistivity values from field observations at various locations and electrode configurations to estimate the true resistivities of the various earth materials and to spatially locate the boundaries below the surface.

A dipole-dipole array was used for this study owing to its high sensitivity to lateral changes in resistivity. The array uses closely spaced electrode pairs to measure the curvature of the potential field, which is good for mapping vertical structures, such as dykes and cavities.

Schlumberger is another array that operates with four aligned electrodes; the outer two electrodes are current source providers while the inner two electrodes are potential

receivers. The potential electrodes are slightly separated (< 1/5 of current electrode spacing) and kept in a fixed position at the center of the array, while the current electrodes have a larger separation during the survey to obtain the minimum observed voltage. The potential electrode spacing could be adjusted along with the constant current electrode spacing to detect the proximal heterogeneities or lateral resistivity changes around the potential electrodes.

The Wenner array (Figure 3.3) is the third common array that utilizes four equally spaced and aligned electrodes. This is considered an advantage for the Schlumberger array and a disadvantage for the Wenner, since it is faster in the field to move the two current electrodes of Schlumberger than to move the four electrodes of the Wenner array between the successive observations. In addition, the Schlumberger array is more robust in distinguishing lateral from vertical variations in resistivity. A major advantage of the Wenner array is that it allows for data minimization and requires less attention to equipment sensitivity.

Dipole-dipole was preferred over Schlumberger and Wenner for its high sensitivity to lateral changes in resistivity and ability to map the vertical structures.

To investigate the change in resistivity at greater depths, the spacing between electrodes is increased to allow more current to flow deeper, which causes the apparent resistivity to become increasingly like the average resistivity of the earth over a greater range of depths. This relationship is plotted as apparent resistivity versus electrode spacing to indicate vertical variations in resistivity. The smaller the spacing between electrodes, the closer the apparent resistivity is to that of the surface material; the larger the spacing between electrodes, the more the apparent resistivity is to that of the bedrock.

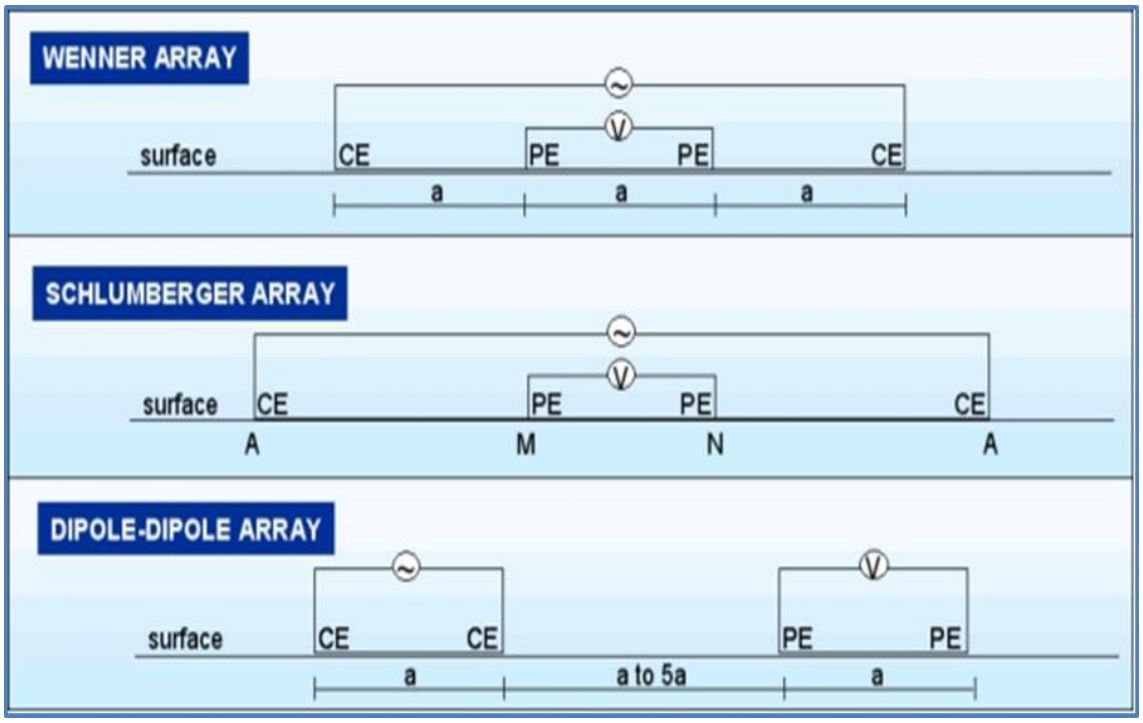

Figure 3.3. The most common array types generally employed in electrical resistivity surveys (http://old.acogok.org/geophysical-tutorial).

The relationship between the electrode spacing and the apparent resistivity of layer 1, 2, and 3 is illustrated in (Figure 3.4). As shown in this illustration, more than 50% of the current induced by array 1 flows through layer 1; hence the value of apparent resistivity determined using array 1 is close to that of layer 1. About 50% of the current induced by array 2 flows through layer 2; hence the value of apparent resistivity determined using array 2 is close to that of layer 2.

More than 50% of the current induced by array 3 flows through layer 3; hence the value of apparent resistivity determined using array 3 is close to that of layer 3.

As the electrode spacing increases, more current flows at greater depths, and the value of apparent resistivity ($\rho a = (2\pi a)\frac{\Delta V}{I}$) becomes increasingly like the resistivity of the earth at greater depths.

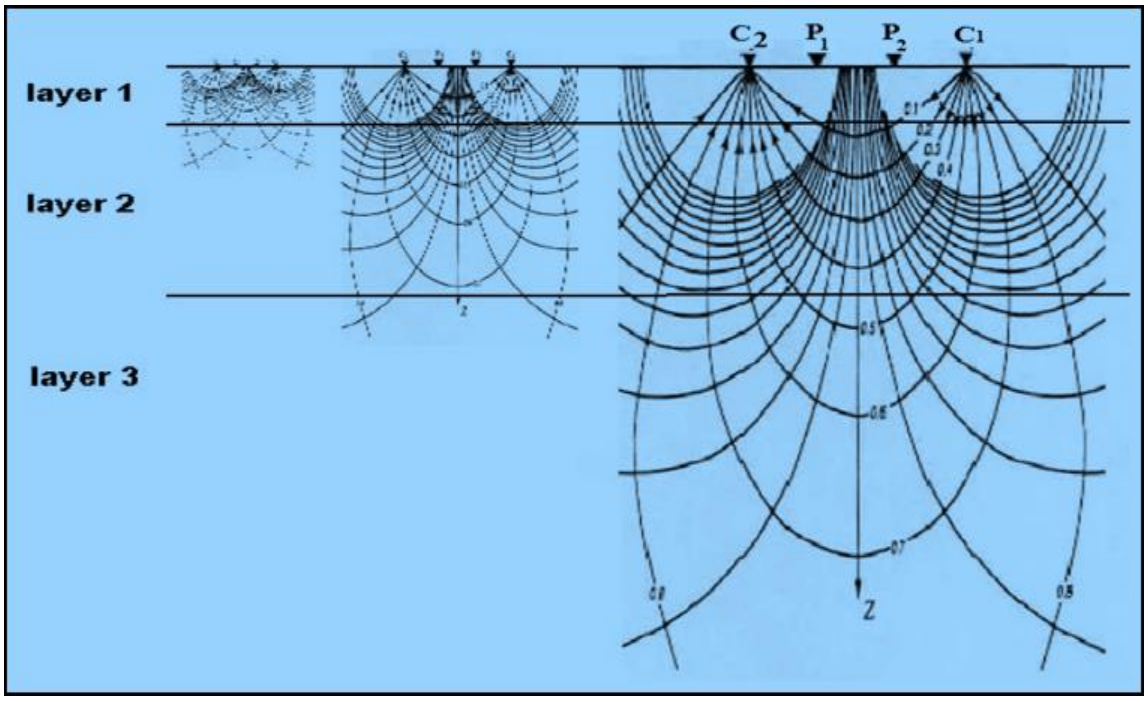

Figure 3.4. The relationship between depth and electrode spacing (Wightman, 2004).

3.1.2. Data Acquisition. SuperSting R8 system was used to acquire the data needed to generate 2D and 3D electrical resistivity images of the subsurface (Figure 3.5).

The system consists of a control unit, passive cables, 12-volt battery, metal stakes, and a switch box. The system can be interconnected to many electrodes, but only four electrodes can be active at a time.

For a dipole-dipole data collection, the system is set to use two electrodes as current electrodes that inject current into the ground and two electrodes as voltmeter electrodes that measure the resulting voltage. The electrode pairs are separated by a pre-determined distance. A known current is transmitted by the SuperSting control unit into the subsurface, while the unit records the corresponding potential difference (Figure 3.6). The apparent resistivity will then be calculated for the pre-determined distance (a) using the equation [$\rho a = (\pi n (n+1) (n+2) a) (\Delta V/I)$].

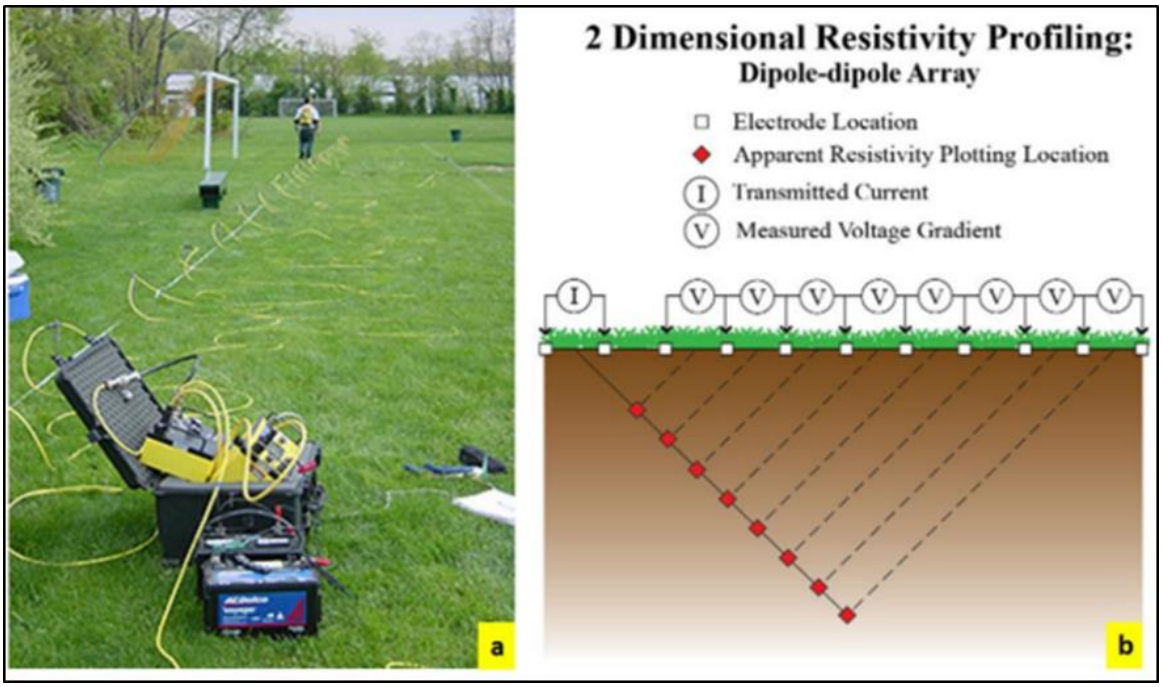

Figure 3.5. The setup of an ERT system. (a) The ERT SuperSting unit for data acquisition. (b) The dipole-dipole array configuration (https://archive.epa.gov/esd/archivegeophysics/web/html/resistivity_methods.ht).

The apparent resistivity (ρa) for all separations between electrodes is then calculated, and a profile for the apparent resistivities is plotted as a function of the midpoint and the number of electrodes (n) (Figure 3.7).

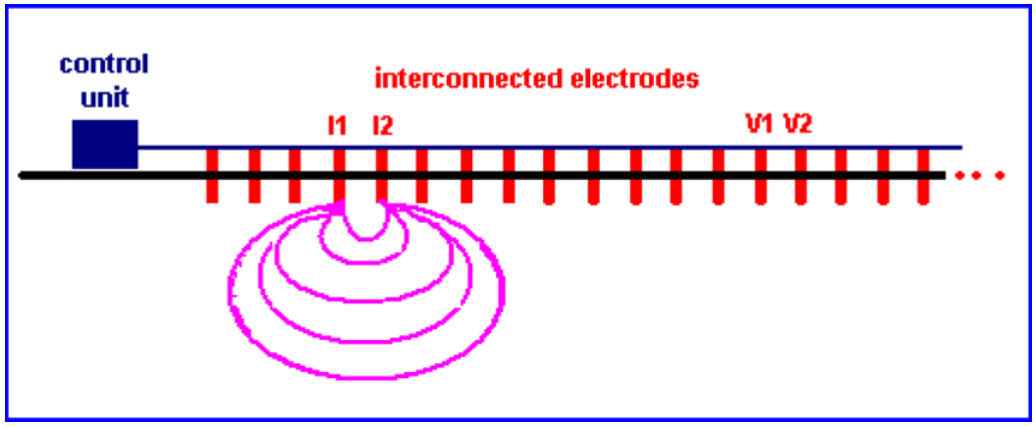

Figure 3.6. Dipole-dipole interconnected electrodes (Neil Anderson, 2017, lecture notes).

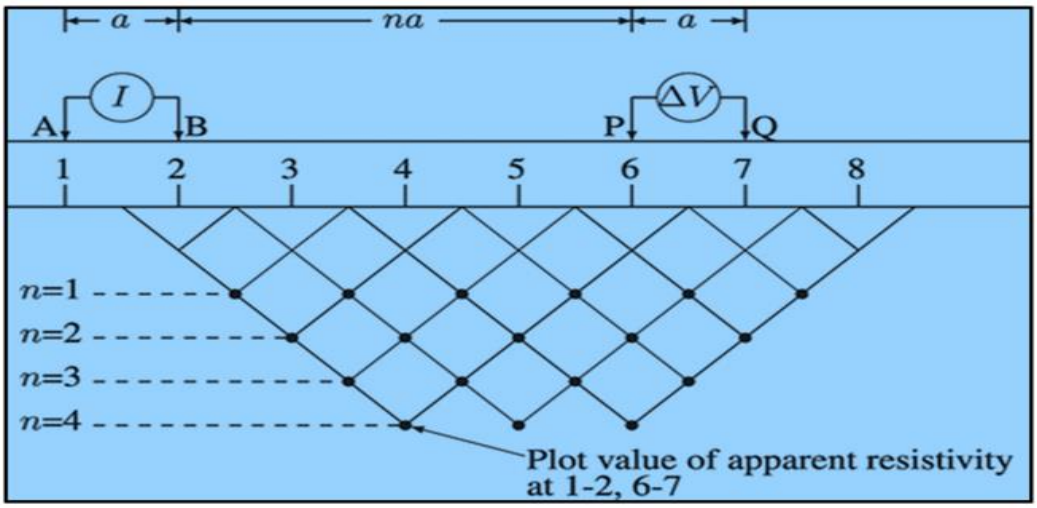

Figure 3.7. Profile plotted from data acquired using (n) number of electrodes at pre-determined distance of (ρa) (Sharma, P. 1997).

3.1.3. Data Processing. Electrical resistivity tomography (ERT) data were acquired using RES2DINV software that transforms the ERT data acquired along the traverses into two and three dimensional (2D and 3D) electrical resistivity images of the subsurface. The RES2DINV software inverts the actual pseudosection data using a tomographic approach, transforming it into a 2D or 3D resistivity image of the subsurface. The processing sequence is explained in Figure 3.8.

3.1.4. Data Interpretation. Data interpretation is a complicated process. It combines the skillfulness of the interpreter, the data, and the environmental factors related to location, time, geology and weather conditions. Contrast in resistivity and detection of anomalies are major guides in data interpretation. For example, an air-filled cavity in a host rock will have a higher resistivity than the host rock; however, if the cavity is water-filled, its resistivity could be comparable to that of the host rock. On the other hand, if the host rock is resistive and the water in the cavity is saline, then the cavity will have a lower resistivity than the host rock.

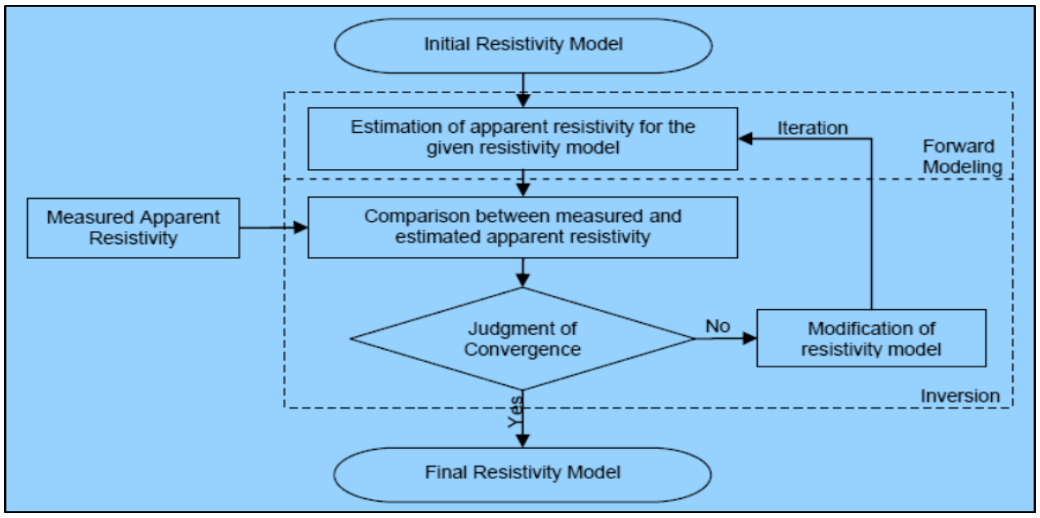

Figure 3.8. Flow chart describing the resistivity inversion process (Society of Exploration Geophysicists of Japan, 2004).

According to Anderson (2015), moist clays in the Springfield area are typically characterized by resistivity values < 125 Ω·m, and dry soil is typically characterized by resistivity values > 125 Ω·m. Resistivity values of fractured rock with moist piped clay-fill are typically < 125 Ω·m, while the resistivity of moist weathered and/or fractured rock is typically >125 Ω·m but < 600 Ω·m. The resistivity for intact rock is typically > 600 Ω·m (Table 3.1).

Table 3.1. Typical resistivity values for different subsurface materials (Anderson, 2015).

Earth Material	Resistivity, Average or Range (Ω.m)
Moist Soil	< 125
Dry Soil	> 125
Moist weathered and/or fractured rock	> 125 < 600
Fractured rock with moist piped clay-fill	< 125
Intact rock or very dry rock	> 600

3.2. MULTI-CHANNEL ANALYSIS OF SURFACE WAVES (MASW)

Surface waves disperse in a way that allows geophysics to analyze the transformation using post-processing software.

3.2.1. Theory. Multi-channel analysis of the surface waves is the process of studying how surface waves change (disperse) as they propagate across a site, i.e. how the seismic energy changes as it progresses along an array of geophones (http://geophysicalservices.com/masw-surveys-acquisition-data-processing interpretation-091717/).

MASW geophysical method assist in measuring the stiffness of the subsurface material. The method responds to the contact between bedrock and unconsolidated soil and could map weathered zones at the top bedrock. It responds also to variations in density, porosity and cementation, and is used in locating the problematic karst features and voids.

Park et al. (2005) stated that the multi-channel analysis of the surface waves method deals with surface waves in the lower 1 Hz to 30 Hz frequencies, particularly for Relight waves. The method also explores a much shallower depth range of investigation (e.g., a few to a few tens of meters).

The principle of (MASW) is built on the seismic wave theory, which itself is dependent on the idea of elastic waves that travel at speeds determined by the physical properties of the media within which these waves travel (Parasnis, 1997). The elastic behavior of materials and the velocity of waves are derived from Hooke's law, which states that the strain (ϭ) of an object is directly related to the stress (s) applied to the object. Stressed material could reach a point where it permanently loses its elasticity, but if it did not reach that point, then a relationship exists between stress and strain named elastic

modulus (E) (Callister Jr., 2001), given by the equation:

$$\sigma = \epsilon E. \tag{7}$$

The wave propagation in a media depends on the ability of the particles of this media to elastically deform under different type of stress, such as compressional or shear stress. The wave velocity (v) is directly related to the frequency of the wave (f) and the length of the wave (λ), as shown in equation:

$$\nu = f\lambda. \tag{8}$$

The wavelength (λ) is the distance between two consecutive peaks or wave troughs. The frequency of a wave is the reciprocal of the wave period (τ), which is the duration required to complete one wave oscillation:

$$f = \frac{1}{\tau}. \tag{9}$$

$$\text{i. e. the wave velocity } \nu = \frac{\lambda}{\tau}. \tag{10}$$

Seismic waves consist of two types: body waves and surface waves (Figure 3.9). Body waves are non-dispersive and travel through a given media at a speed that is proportional to the material density and modulus.

Body waves travel in a longitudinal or transverse manner relative to the travel direction. The longitudinal waves are called P-waves or compression waves, and the transverse waves are the S or shear-waves. P-waves transfer energy through media by compressing and dilating particles.

In an S-wave, particles move perpendicular to the direction of wave movement. Generally, in a homogeneous environment, the velocity is expressed by the equation:

$$\nu = \sqrt{\frac{material\ elastic\ modulud}{material\ density\ (\rho)}}. \quad (11)$$

Seismic waves are naturally produced during earthquakes, thunder, or tidal waves. Artificially, these waves are generated using active sources, or can passively be acquired.

The propagation velocity of the seismic Raleigh and love waves is dependent on the shear-wave velocity (Vs) of the earth material (the stiffness of earth material), a property known by the term, dispersive.

The MASW method utilizes this dispersive property to map the stiffness of earth material in terms of shear velocity (Vs) to obtain a desired depth (1D) or depth and location (2D).

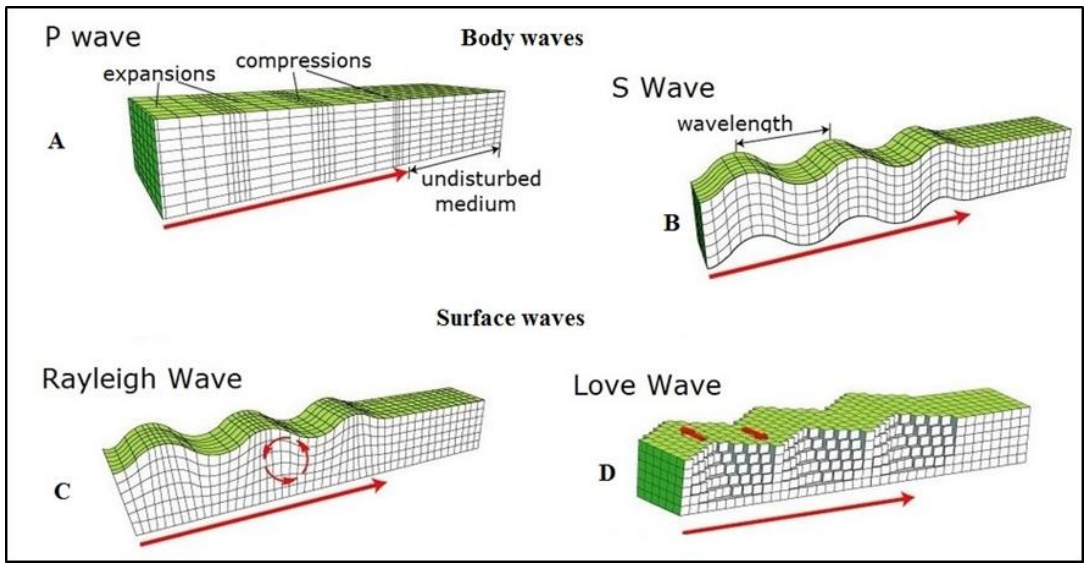

Figure 3.9. The seismic body waves A and B and surface waves C and D (Park et al., 2005).

The MASW system generally determines the shear-wave velocity (Vs) of earth material at a frequency range of 3Hz -30 Hz. MASW is a high energy method and

possesses an excellent ability to removing noise from body waves and surface waves, including Relight waves.

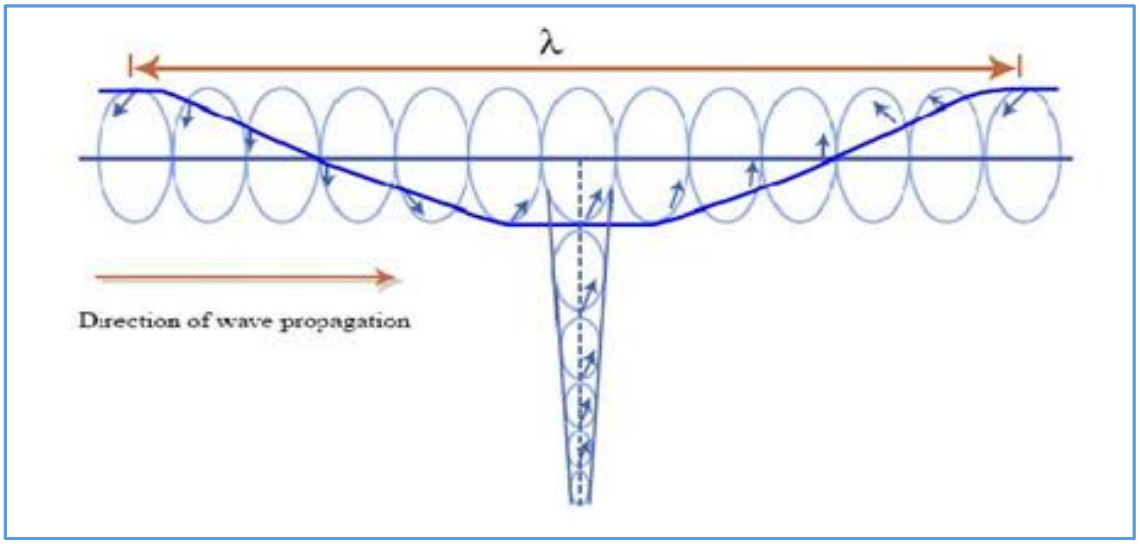

Figure 3.10. Retrograde, elliptical particle motion of Rayleigh Wave (Van Der Hilst, 2004).

The MASW method images waves using the wave-field transformation method into a well-defined energy dispersion pattern. The MASW method is widely used as an efficient geophysical method to delineate and map the topographic boundary between soils and bedrock, based on the shear velocity (Table 3.2).

Table 3.2. Shear wave velocity (Vs) of some earth materials (NEHRP, 1997, National earthquake hazards reduction program).

Earth Material	Average Shear-wave Velocity
Hard rock	>5000 ft/sec (> 1500 m/sec)
Rock	2500-5000 ft/sec (750-1500 m/sec)
Very dense soil and soft rock	1200-2500 ft/sec (360-750 m/sec)
Stiff soil	600-1200 ft/sec (180-360 m/sec)
Soft soil	<600 ft/sec (<180 m/sec)

A general illustration for the theoretical MASW active system setting, data collection, and data processing is illustrated in Figure 3.11.

3.2.2. Data Acquisition. In general, a typical field setting for acquiring MASW data consists of twenty-four low-frequency geophones (4.5 Hz), which are usually used and positioned at predetermined distances. The distances are related to the shortest wavelength (λmin) of the light at the desired depth of investigation. The length of the receiver spread (D) directly relates to the longest wavelength (λmax) that can be analyzed.

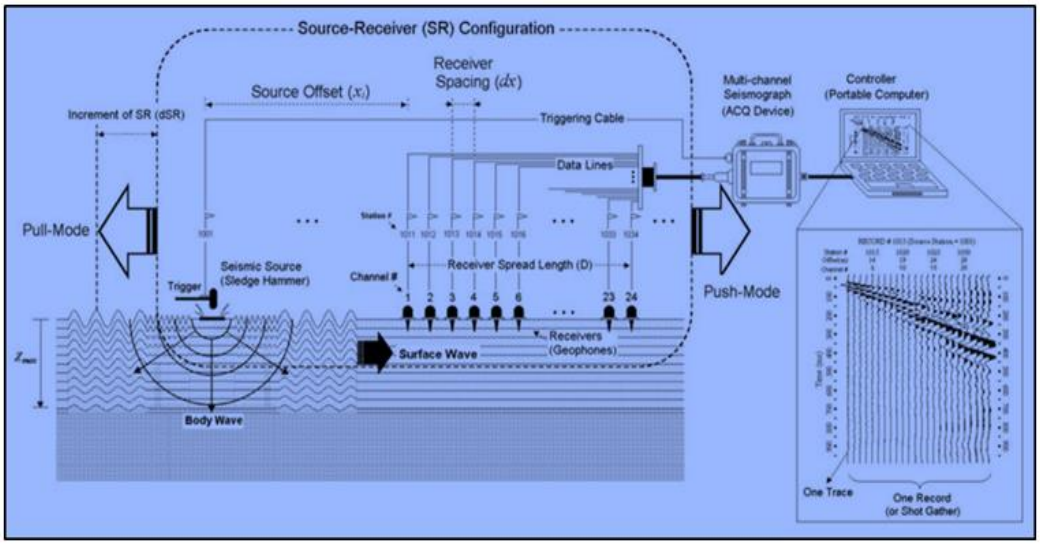

Figure 3.11. Active MASW field survey (http://www.masw.com/DataAcqisitiom.html).

The longest wavelength (λmax) determines the maximum depth of investigation. These relationships hold as: (zmax): D ≈ λmax ≈ zmax. The site and type of active source can cause some variations in these relationships (Figure 3.12). This figure shows the source-receiver configuration. The most important parameters in the MASW are the source offset (x1) and receiver spacing (dx). The source offset is set at a predetermined distance from the nearest geophone.

Figure 3.13 display the equipment and an actual field setup. The equipment consists of sledgehammer, metal plate to concentrate signal, measuring tape, geophones, battery, connection unit, cables, and a field laptop.

3.2.3. Data Processing. The acquired MASW data is processed using the Kansas Geological Survey (KGS) software package SurfSeis. The software transforms the data into a 1D shear velocity profile by extracting the fundamental-mode dispersion curves (velocity vs frequency) to obtain a 1D shear-wave depth profile. The second processing stage involves the generation of a frequency vs phase velocity dispersion curve from the acquired Rayleigh wave field data, using the wave-field transformation and modified wave-field transform. The resulting curve is transformed into a 1D depth vs shear-wave velocity profile from which the elastic properties, density, and thickness of layers in the subsurface are obtained (Figure 3.14).

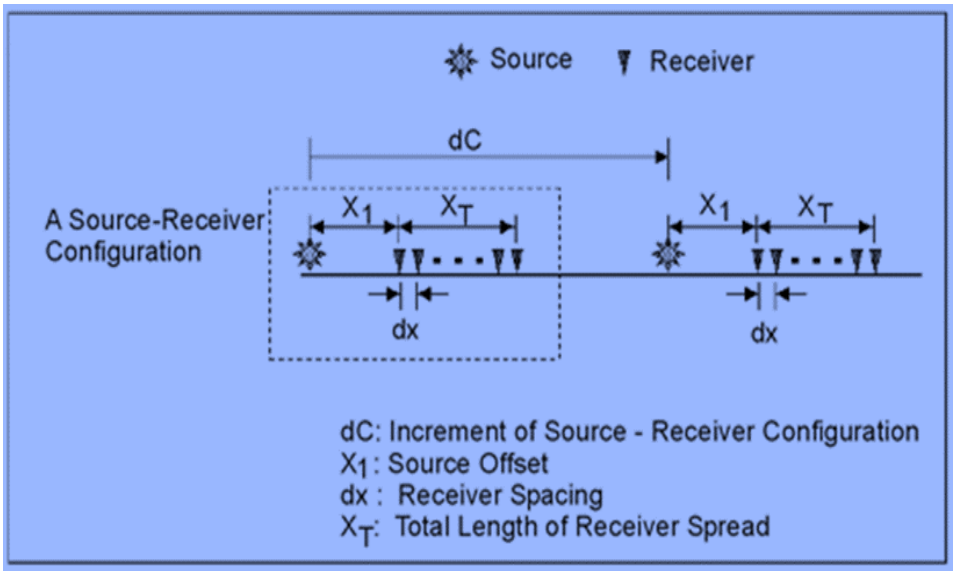

Figure 3.12. Definition of a source-receiver configuration and increment of the configuration (Park et al., 2005).

Park, C. B. et al., (2005) and the Kansas Geological Survey concisely summarized the MASW method as (1) obtaining the shot gathers, (2) extracting the dispersion curves, and (3) inverting the dispersion curves to get the (1D) depth and/or the surface and depth (Figure 3.15 and Figure 3.16).

Figure 3.13. MASW equipment's and tools.

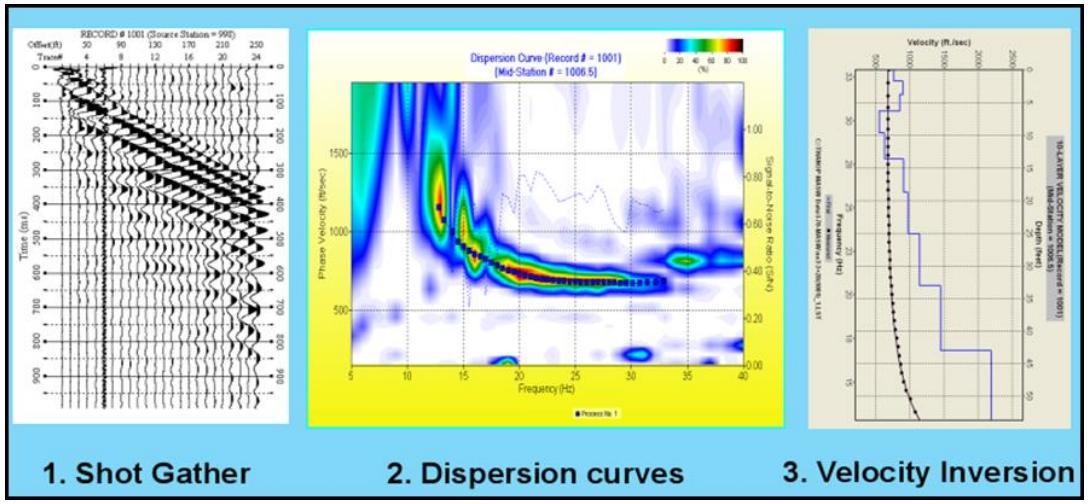

Figure 3.14. MASW surface wave data set transformed into a 1-D shear-wave velocity profile of the subsurface (Park, 2006).

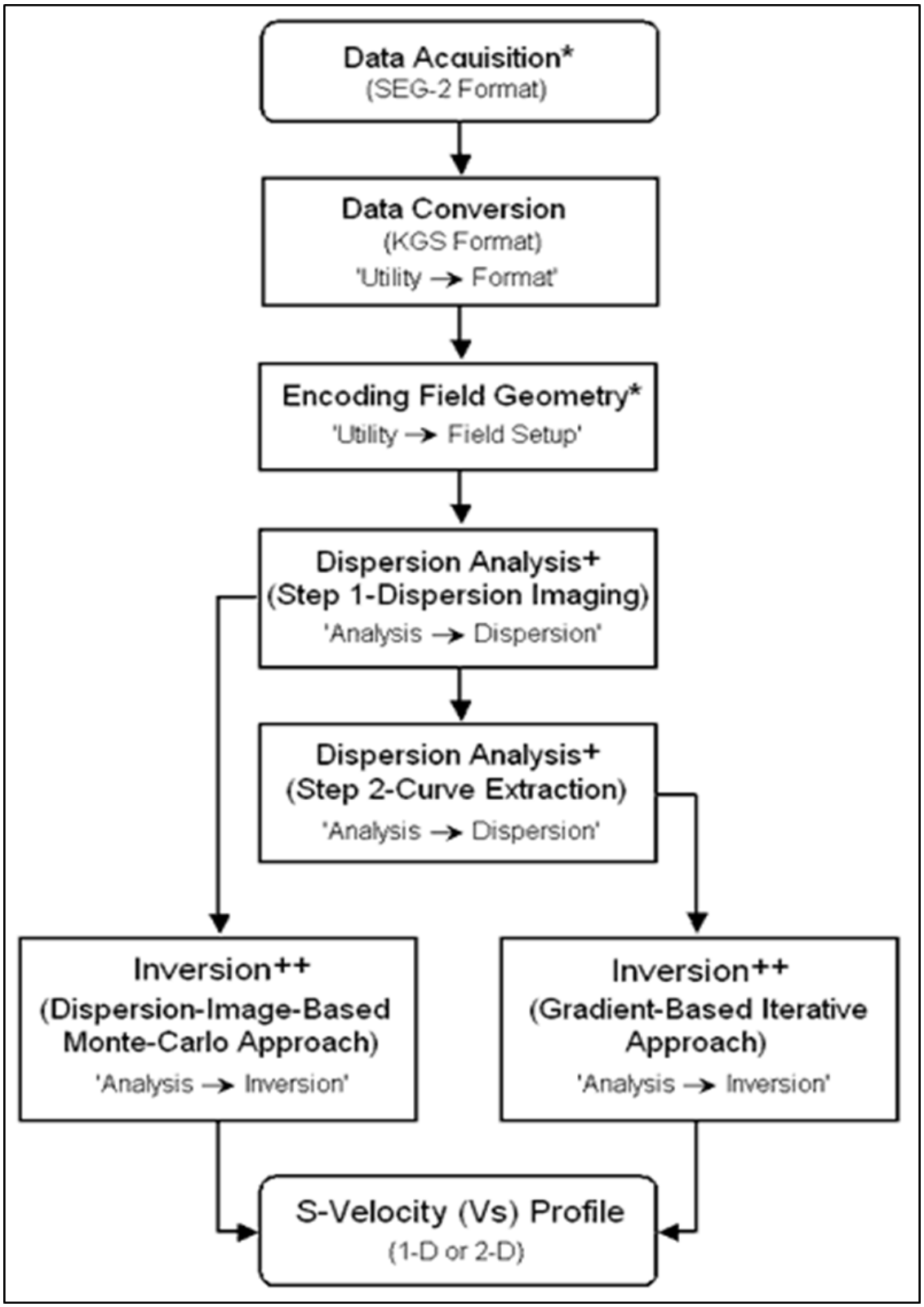

Figure 3.15. A step-by-step approach for data processing and analyzing MASW profiles (Kansas Geological Survey).

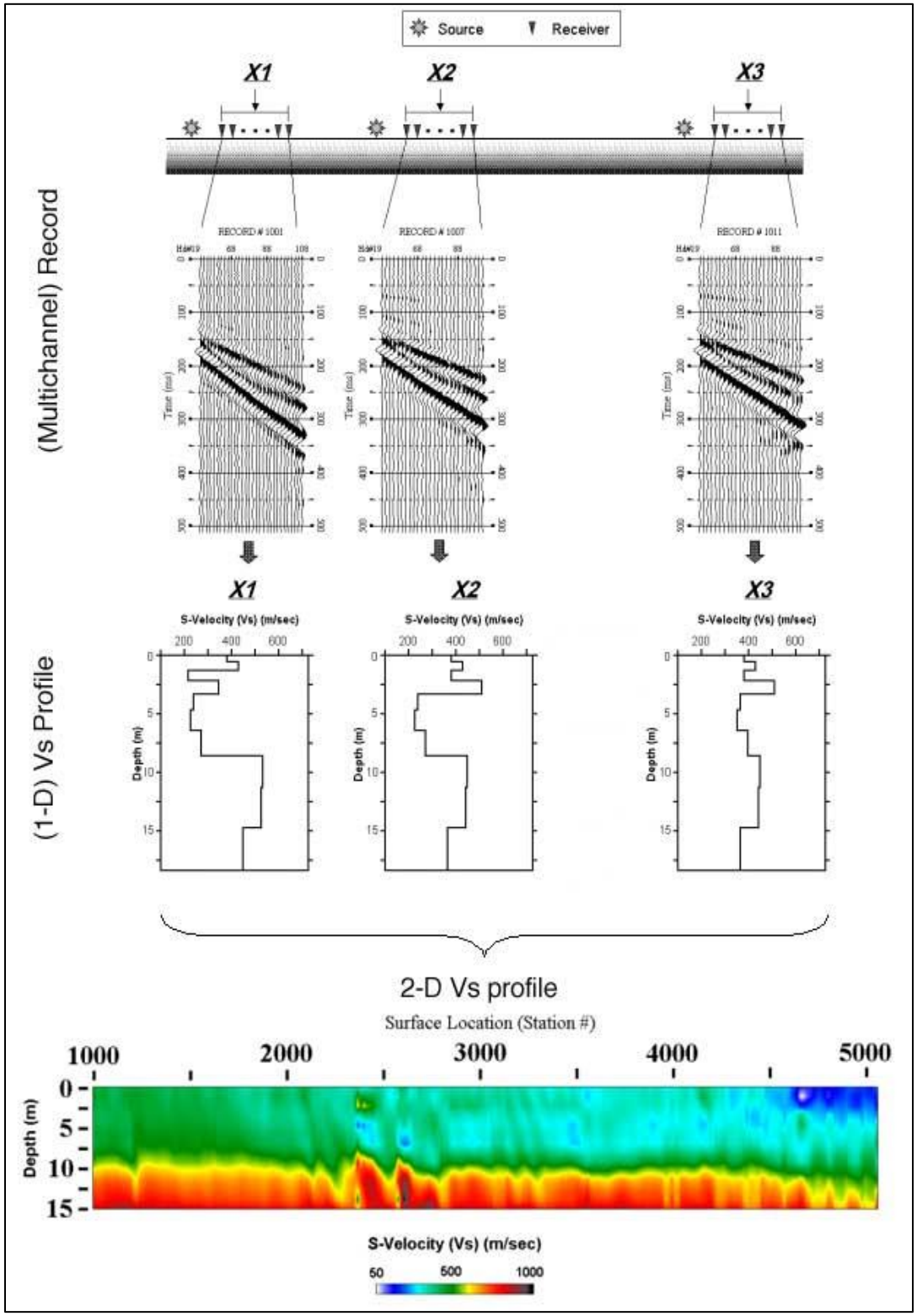

Figure 3.16. Overall procedure for the 2-D shear-wave velocity map with the MASW survey (https://www.researchgate.net/publication/228977208_MASW_horizontal_resolution_in_2D_shear-velocity_Vs_mapping/figures?lo=1).

3.2.4. Data Interpretation. Interpretation of geophysical data (including MASW data) generally involves many factors. The interpreter's knowledge of the study area and its geology, stratigraphy, climate, topography, and development history will have a positive impact on the interpretation of the data, and on the study goals and objectives.

The MASW interpretation involves the careful consideration of the relationship between shear-wave velocities and depth to realistically model the subsurface.

Interpretation should consider the use of more than one geophysical method to complement each other, due to some inherent limitations in methods, equipment, and the variation of environmental factors.

Although variations in shear-wave velocities could occur within short distances in natural conditions, it is still advantageous to have a general idea about shear-wave velocities from previous studies as a reference. In situations where anomalously low or high values are obtained during data acquisition, these values could raise concern and suggestions in investigating the acquired data, calibrating the equipment, or conducting confirmatory studies.

4. DATA ACQUISITION AND PROCESSING

4.1. ELECTRICAL RESISTIVITY TOMOGRAPHY (ERT)

The electrical resistivity system used for this survey was the SuperSting R8, manufactured by Advanced Geosciences, Inc.

4.1.1. ERT Data Acquisition. The complete field system consists of the transmitter/receiver SuperSting R8 instrument console, switch boxes, two 12V power supply batteries, passive cables and metal stakes. 168 electrodes were fixed on the pinned metal stakes in a straight line from both sides from the centered SuperSting R8 (Figure 4.1). The electrodes were spaced at 5 ft. intervals along each traverse. The desired maximum depth of investigation was 100 ft.

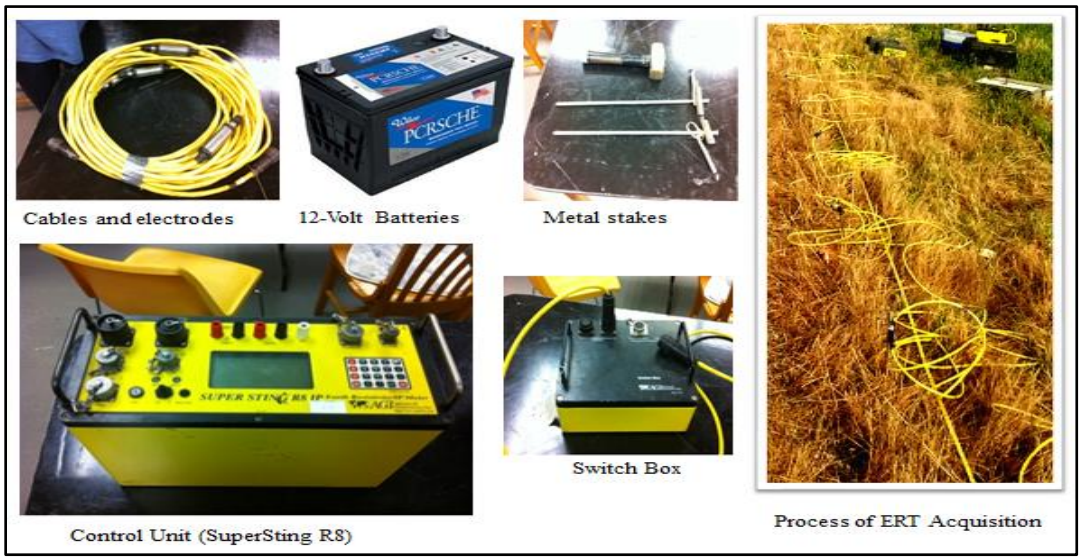

Figure 4.1. The equipment used for ERT data collection.

ERT profiles were acquired along more than hundred separate traverses in the study area. The traverses were oriented either west to east or north to south. The spacing between

adjacent parallel traverses was nominally 100 ft. Thirteen (13) representative examples of ERT profiles are presented herein, some of which were selected to illustrate the major factors that contributed to the observed resistivity anomalies in the subsurface. (Figure 4.2).

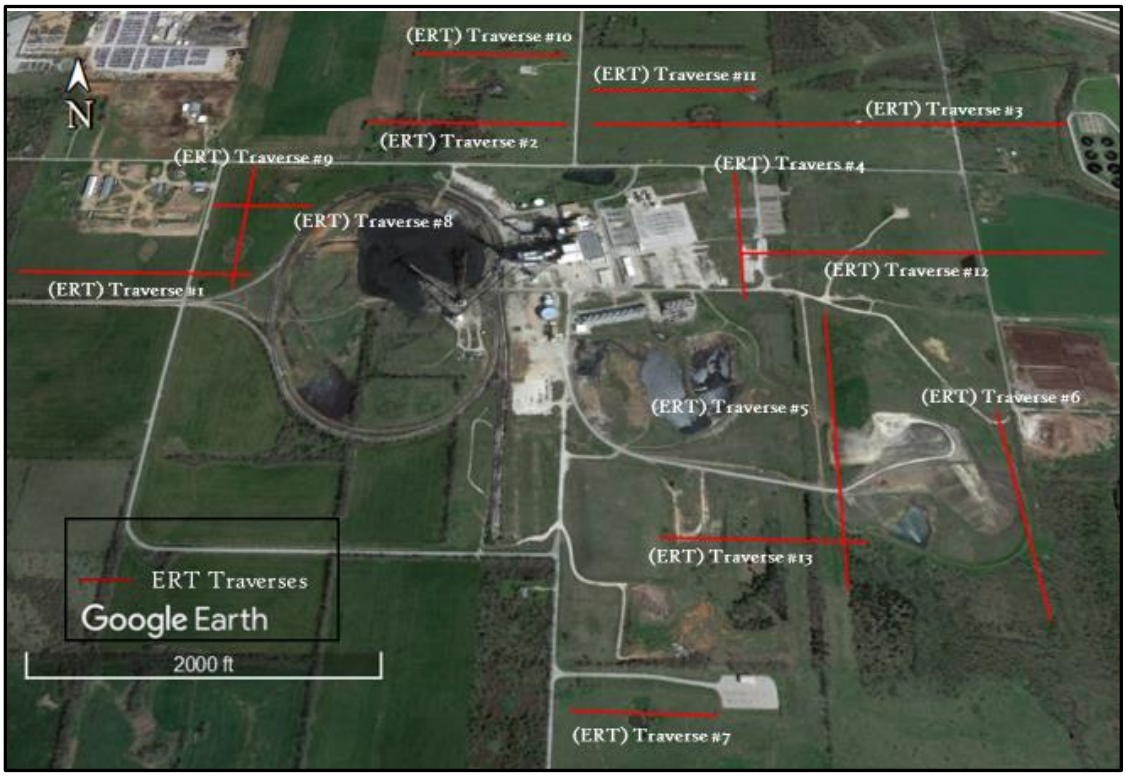

Figure 4.2. The location of ERT traverses presented in this study.

4.1.2. ERT Data Processing. RES2DINV software was used to process the ERT data acquired in this study. The software was used to identify and remove the bad data (Marescot & Loke, 2004), and for the compilation of a resistivity model. The steps of the ERT data processing are illustrated in Figure 4.3 to Figure 4.7 and accompanying text. The steps include:

Reading the (.stg) SuperSting data file into computer, and converting the file into a format, readable using res2dinv processing software (dat).

Loading the (dat) file in res2dinv software and exterminating bad data points (Figure 4.3). Bad points are caused generally by electrodes that are not properly coupled (electrically) to the ground surface. Uncoupling could result from moisture deficiency, damaged cables, or by shorting across the cables due very wet ground conditions. The processing software provides guidance with respect to the removal of bad data points.

Reading the saved file and performing the default inversion to get the pseudosection. Inversion is the process of reconstructing a model computed from the collected data values by using a set of measurements. The pseudosection is created using the default parameters, which includes 7 iterations.

SuperSting displays the data in meters. The display was changed to "feet" by selecting "feet" in the data/display change setting submenu; then editing the data to reset the inversion/damping factor values of the pseudosection.

The damping factor (λ) is used as a smoothness-constrained factor in least-squares inversion equations. The factor has a value between 0.25 and 0.05 and is set to a higher value if the data set is noisier. Inversion, coupled simultaneously with damping, removes the apparent variability artifacts that may arise due to overfitting noisy data to obtain a true model of the data.

Other parameters that changed include the absolute error to RMS error and the model cell width (changed to be half the unit of electrode spacing and setting contour intervals) to delineate the boundaries between the different earth material. These changes are applied to set a reasonable scale for the extended model discretization (Figure 4.4).

Following the setting of new parameters, inversion is carried on until it completes four (4) selected iterations, (Figure 4.5).

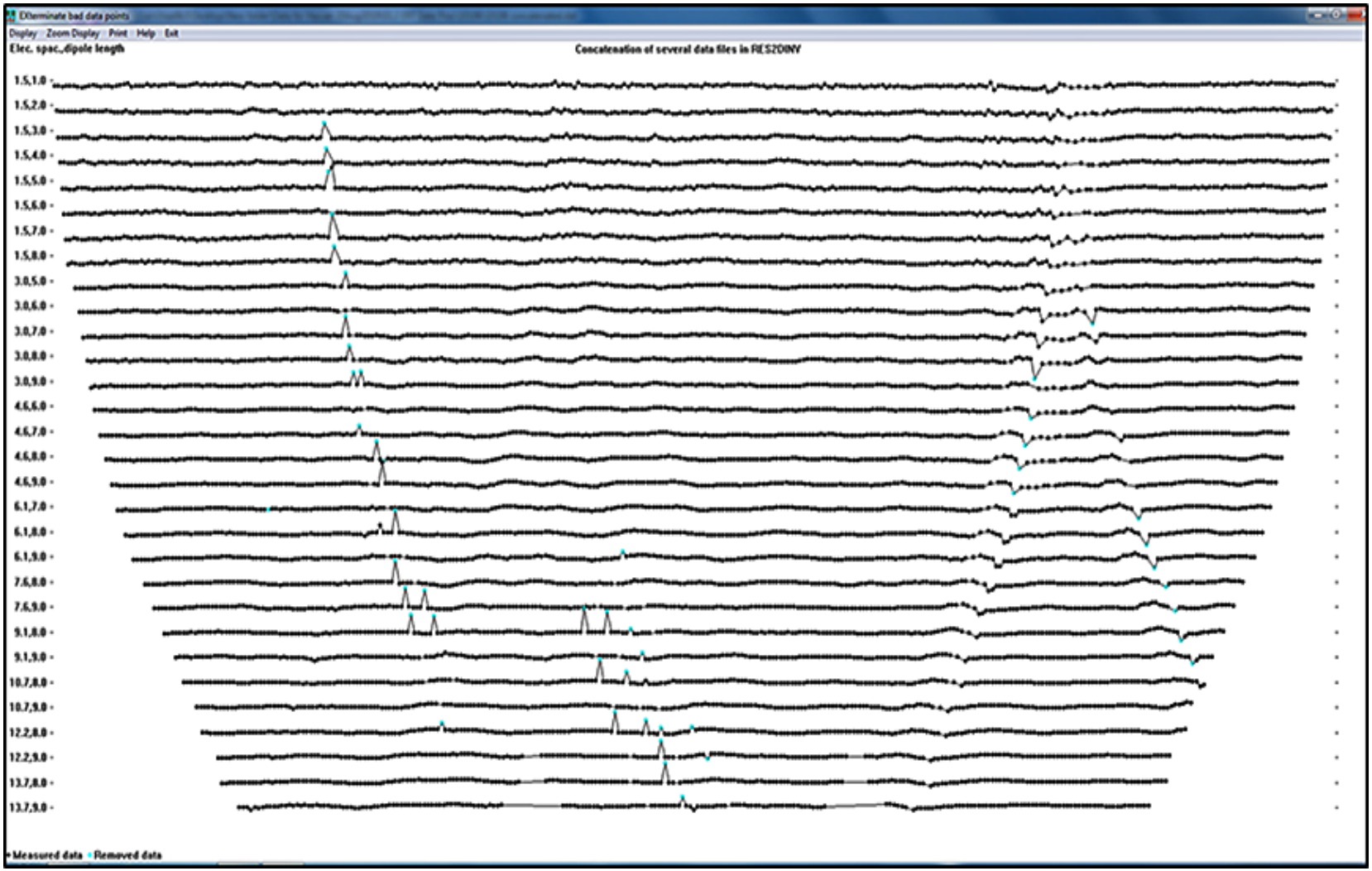

Figure 4.3. Identifying and removing the bad data (blue dots).

The iterations minimize the variation in the data RMS misfit and the model RMS misfit during the 2D inversion of apparent resistivity data. The misfits are normalized with respect to the value at the iteration numbers. Data are edited after the completion of iterations and the RMS error statistics are evaluated. When the RMS is high, an effort is made to reduce noise, and then data are reprocessed until the RMS is less than 10% (Figure 4.6). When the RMS error is < 10 %, the model is accepted (Figure 4.7).

Resistivity measurement acquired is apparent resistivity, which processed in an inversion program to give the distribution of electrical properties of the subsurface and is representable in a 2D (pseudosection) profile.

The Pseudosections associate the log of the values of apparent resistivity with the (x, y) location. Location (x) is the mid-point of the measuring, electrodes, and location (y) relates to the electrodes spacing. The data are then contoured to yield a pseudosection.

The pseudosection is the first step in assessing the quality of data; bad electrodes are identified, and heterogeneity is visually detected. The middle section is the calculated apparent resistivity result, and the bottom section, is the final inverse model resistivity section (the truest representation of the true subsurface) (Figure 4.7).

The acquired ERT data are fair-to-excellent quality, particularly considering that the data were acquired in complex karst terrain. The practices resulted in excellent quality data, and they included the regular conduction of contact resistance tests prior to data acquisition surveys to ensure the electrical connectivity of electrodes. Cable issues and anomalously high resistance values were corrected in the field. The wetting of dry/or porous soils was regularly completed during surveys when high resistance values were initially recorded during the contact resistance tests.

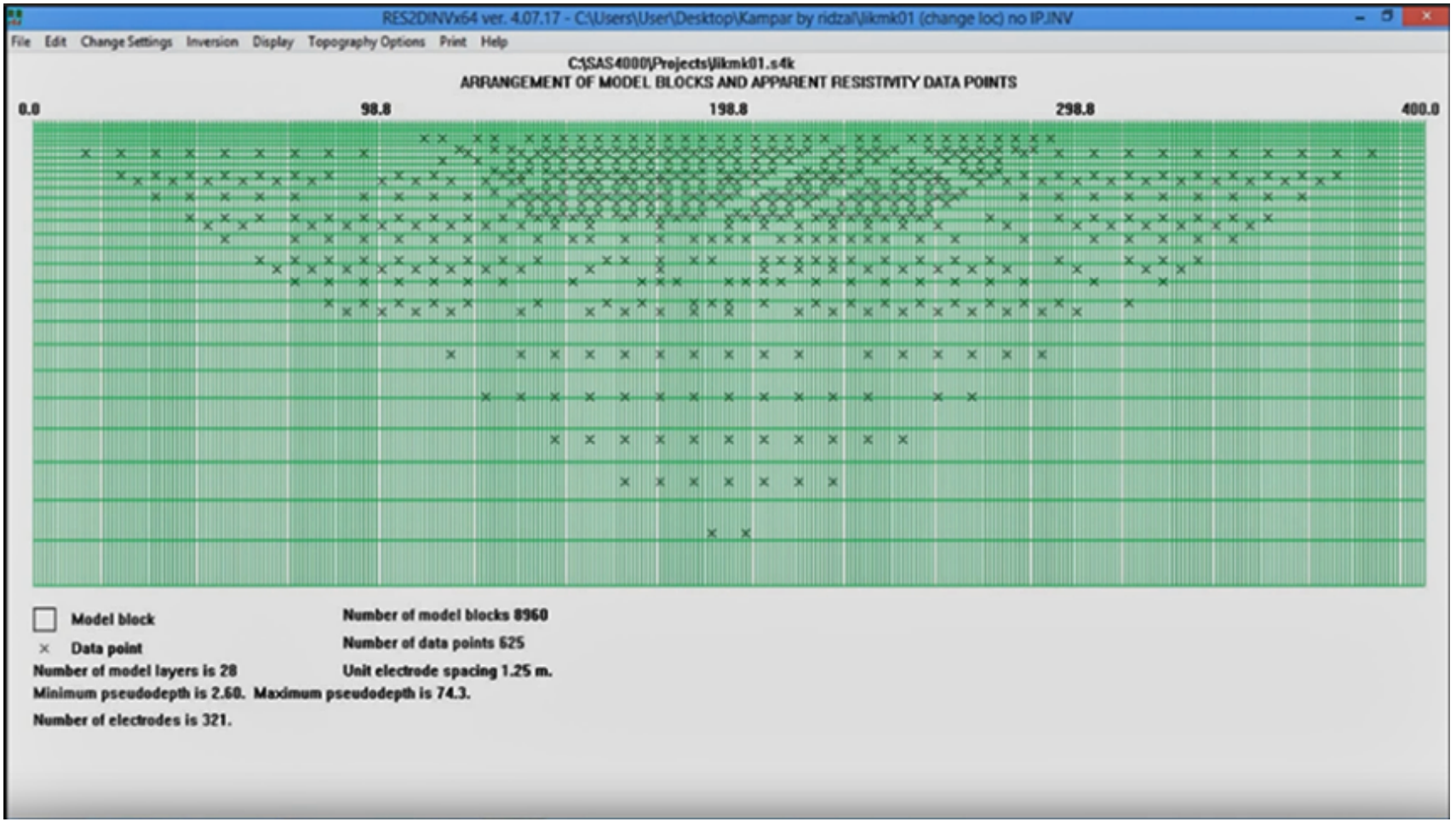

Figure 4.4. Model discretization

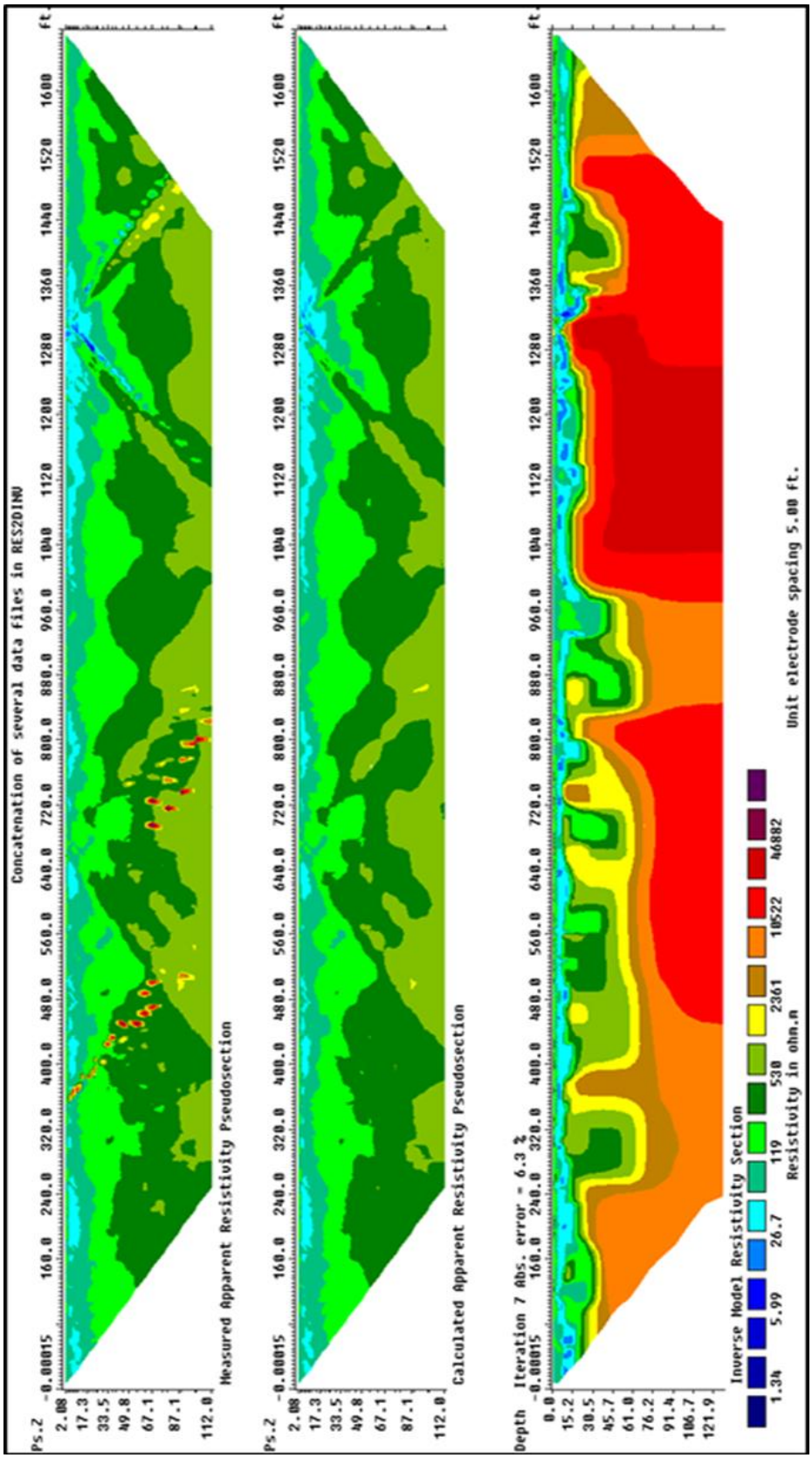

Figure 4.5. The measured apparent resistivity pseudosection (upper), calculated apparent resistivity pseudosection (middle), and inverse model resistivity section (lower) after the complete inversion.

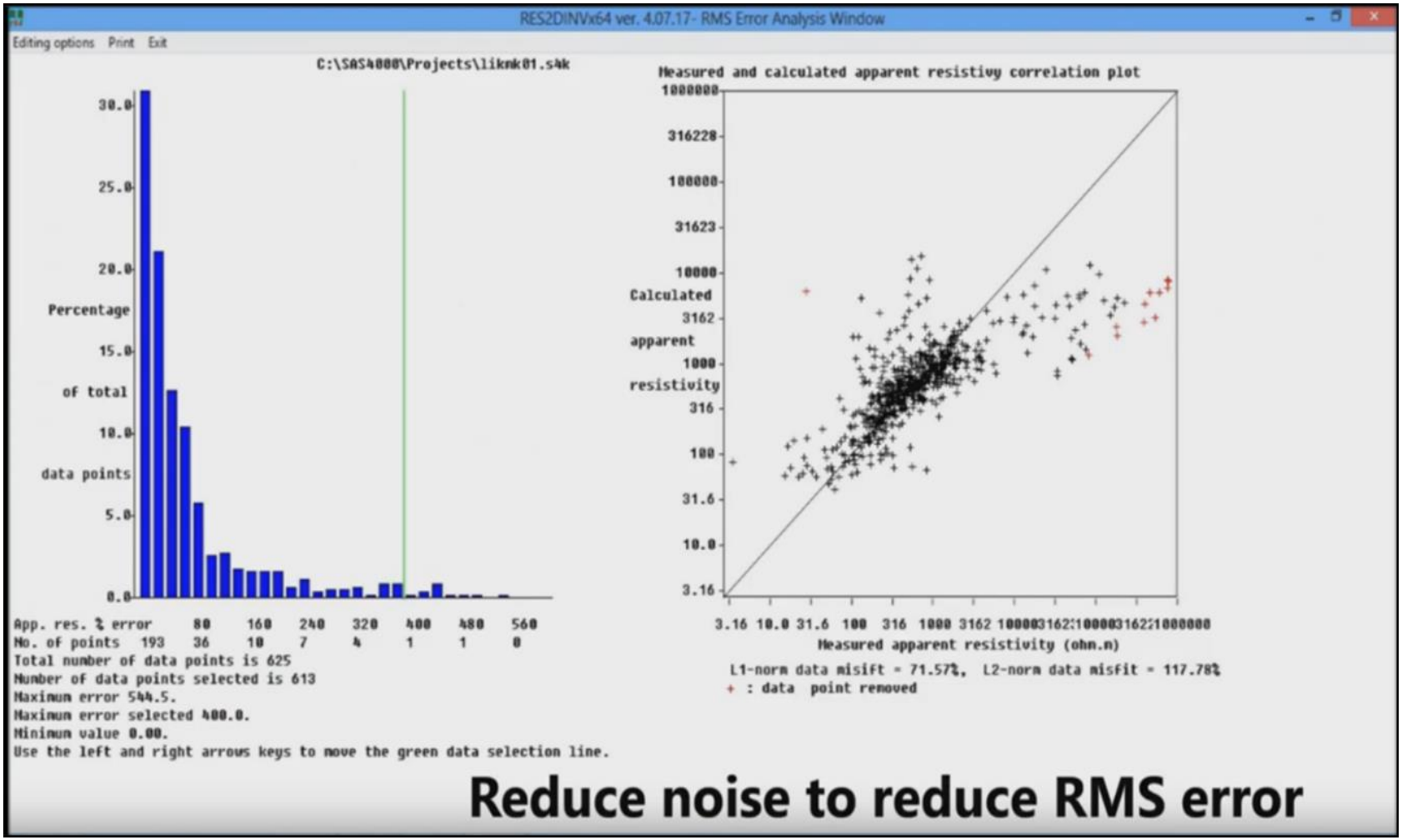

Figure 4.6. The figure explains the noise and RMS error reduction process.

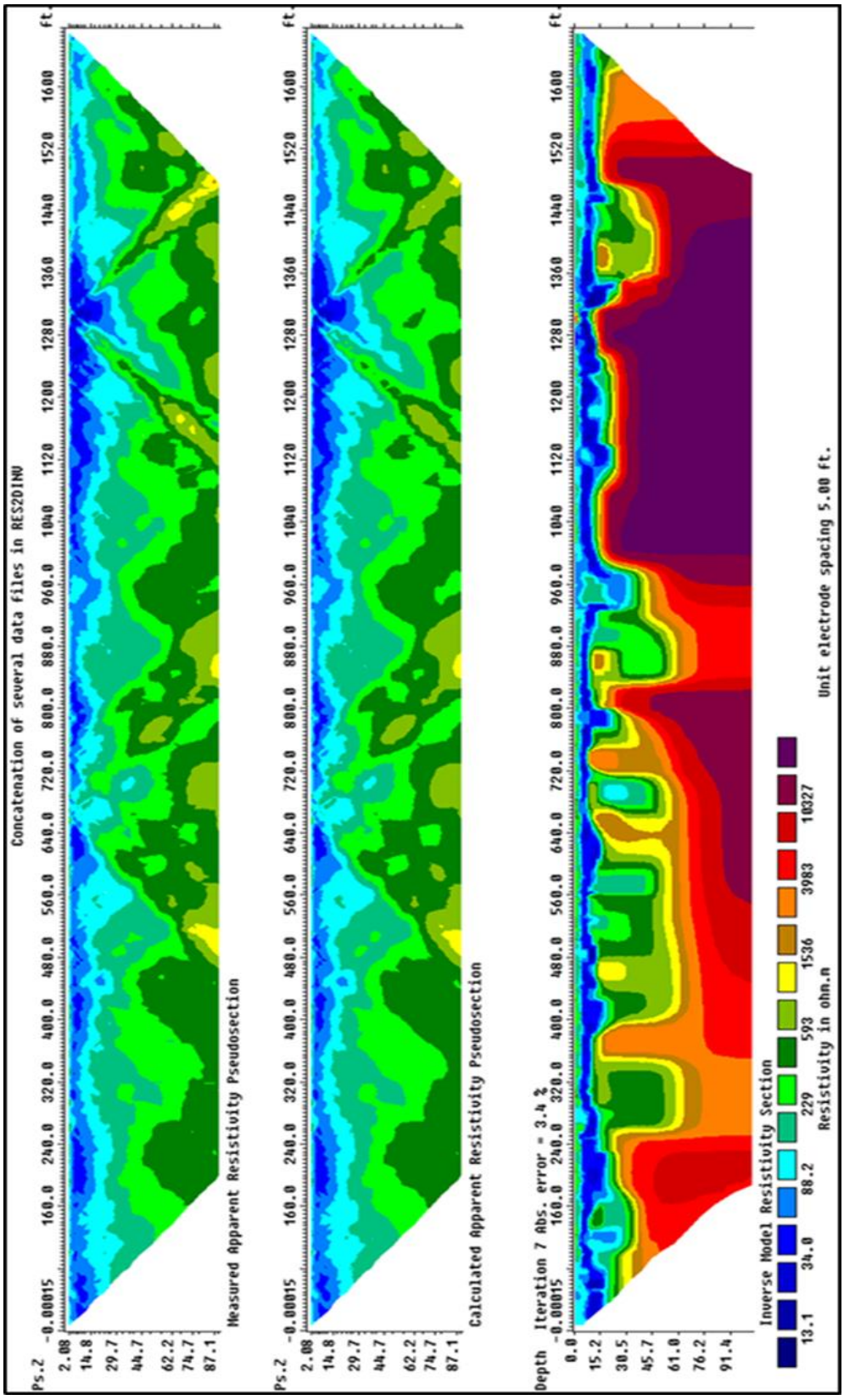

Figure 4.7. The final ERT model generated by concatenation of several data files using 168 electrodes, spaced at 5ft apart, with a total profile length of approximately 1680 ft.

Shallow and loose electrodes and stakes were checked and properly fixed. During the actual data acquisition, output errors were viewed and continuously monitored on the instrumentation screen. In some situations, data acquisition was terminated when continuous high values or negative resistivity values were viewed on the instrument. In such situations, the cables and electrodes were checked for problems and were fixed or replaced.

Data quality is automatically assessed during processing by the software, the RMS error is calculated, and the software determines the quality of the data and may reject it. Generally, the quality of data is accepted and considered reliable in this study when the RMS is less than 10%. Some of the data used in this study has RMS values < 4 %, which is high quality data.

For the purpose of this research, several electrical resistivity tomography models were generated from the acquired data using 168 electrodes, spaced at 5 ft. apart. Six of these profiles were presented here below as examples (Figure 4.8 to Figure 4.13).

4.2. MULTI-CHANNEL ANALYSIS OF SURFACE WAVES (MASW)

The MASW data were acquired on the ERT traverses and mostly on a grid of 400 ft. The MASW traverses were oriented approximately parallel to the direction of the ERT traverses. The acquisition parameters and the acquisition software setup for conducting active MASW surveys were summarized by Park et al. (2002) in (Table 4.1) and the (Figure 4.14).

4.2.1. MASW Data Acquisition. A 24-channel seismograph equipment and 24 vertically polarized 4.5 Hz geophones were used to acquire the MASW data.

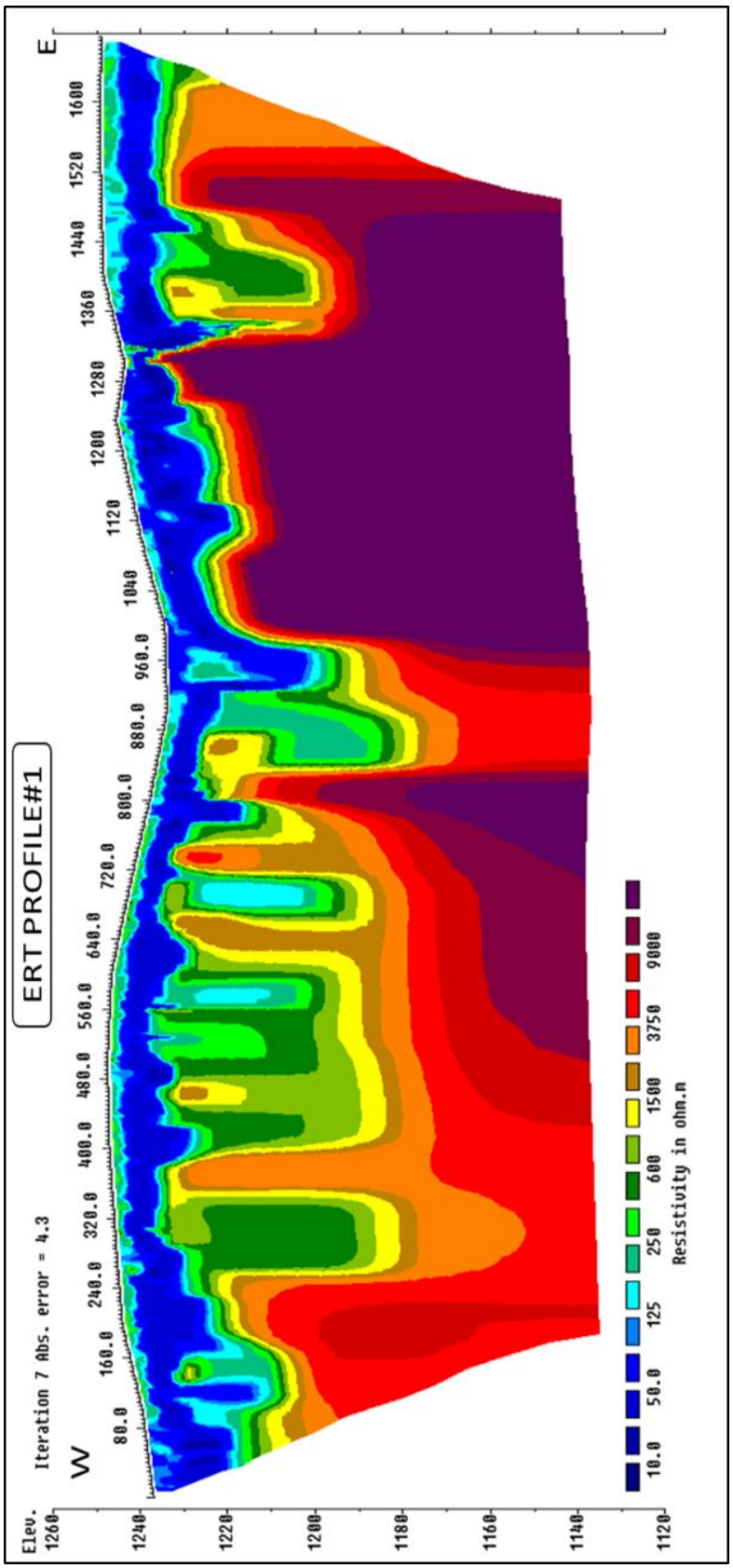

Figure 4.8. ERT profile #1. ERT model generated using 168 electrodes spaced at 5 ft apart with a total profile length of approximately1680 ft.

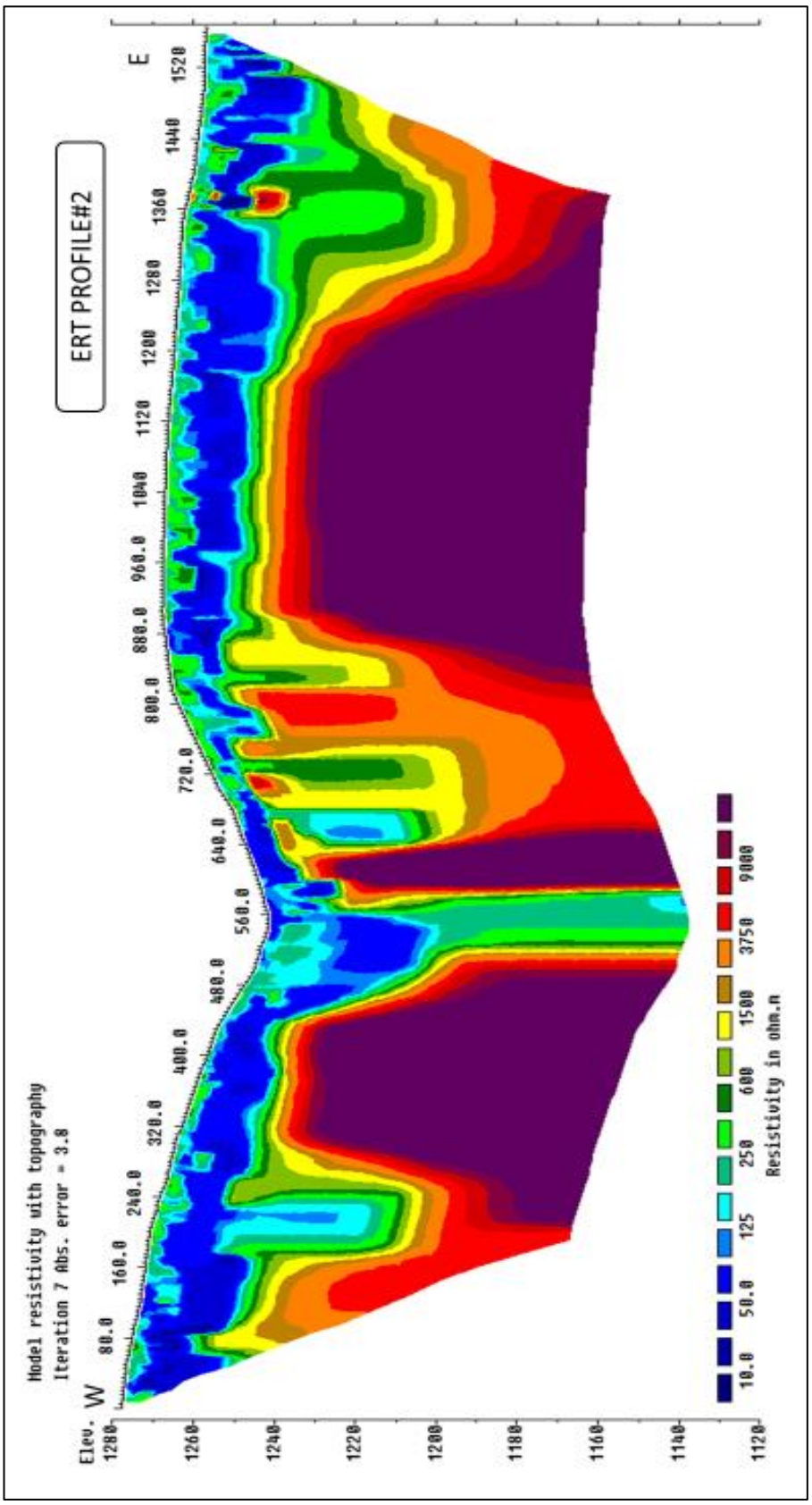

Figure 4.9. ERT profile #2. ERT model generated using 168 electrodes spaced at 5 ft apart with a total profile length of approximately 800 ft.

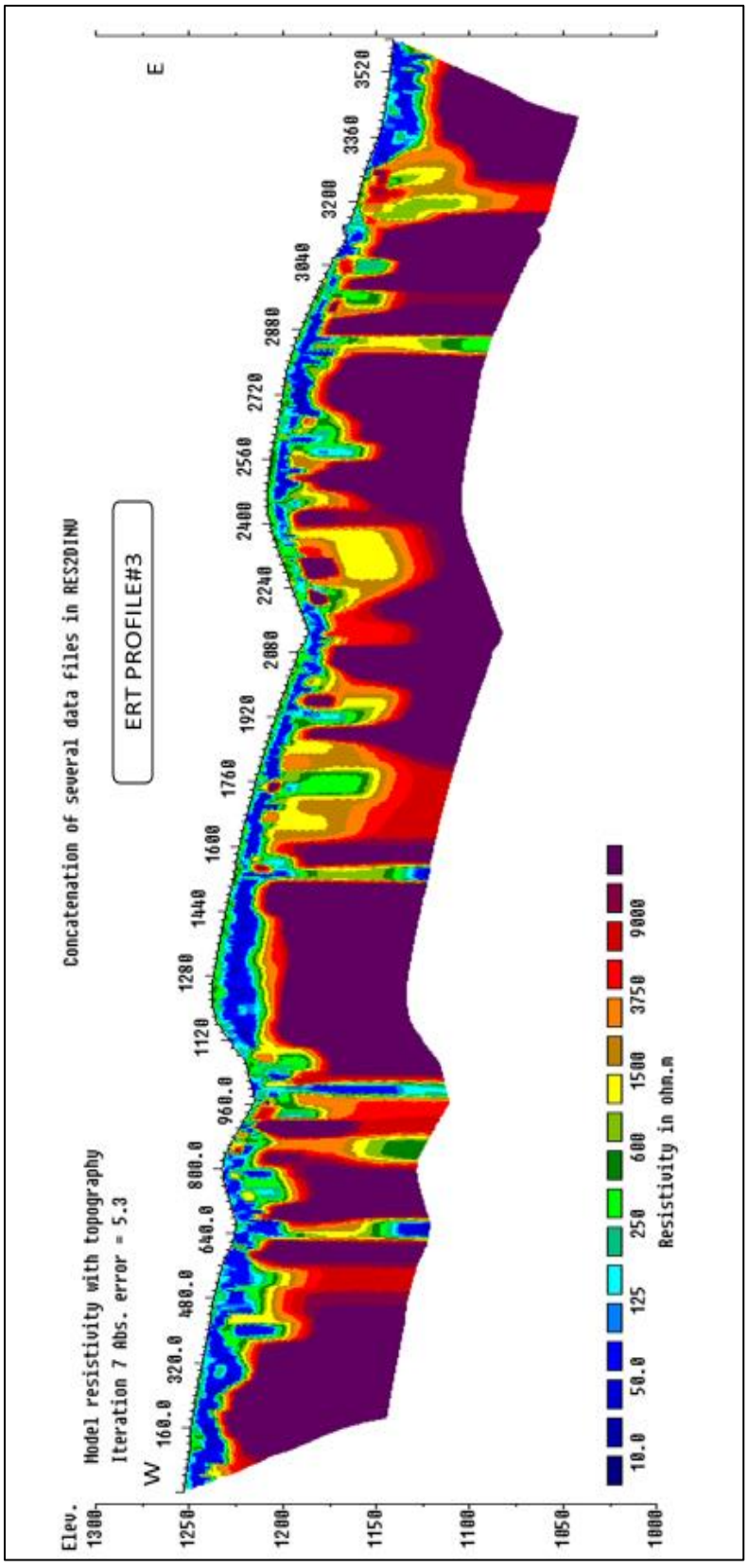

Figure 4.10. ERT profile #3. ERT model generated using 168 electrodes spaced at 5 ft apart with a total profile length of approximately 2500 ft.

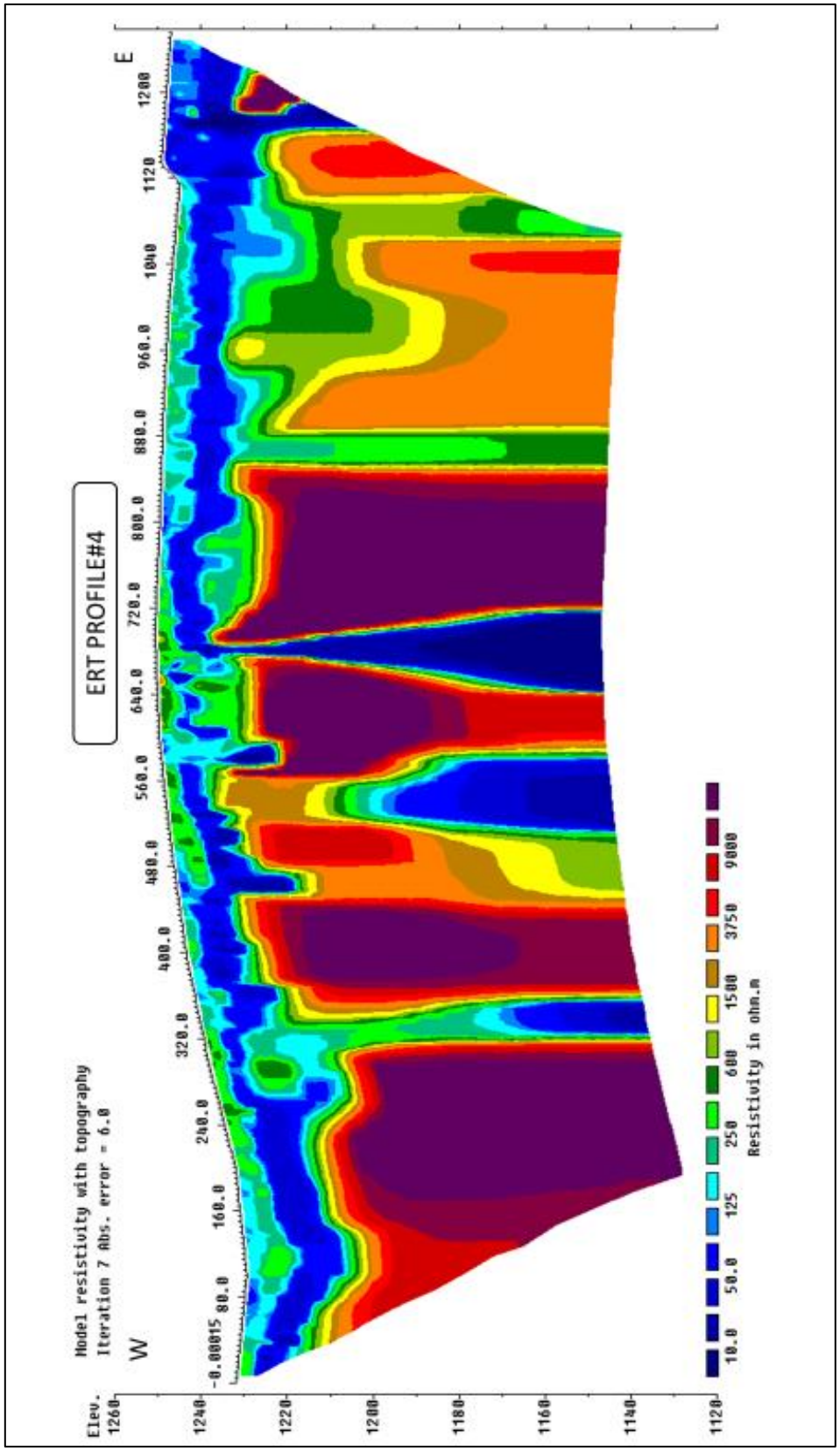

Figure 4.11. ERT profile #4. ERT model generated using 168 electrodes spaced at 5 ft apart with a total profile length of approximately1300 ft.

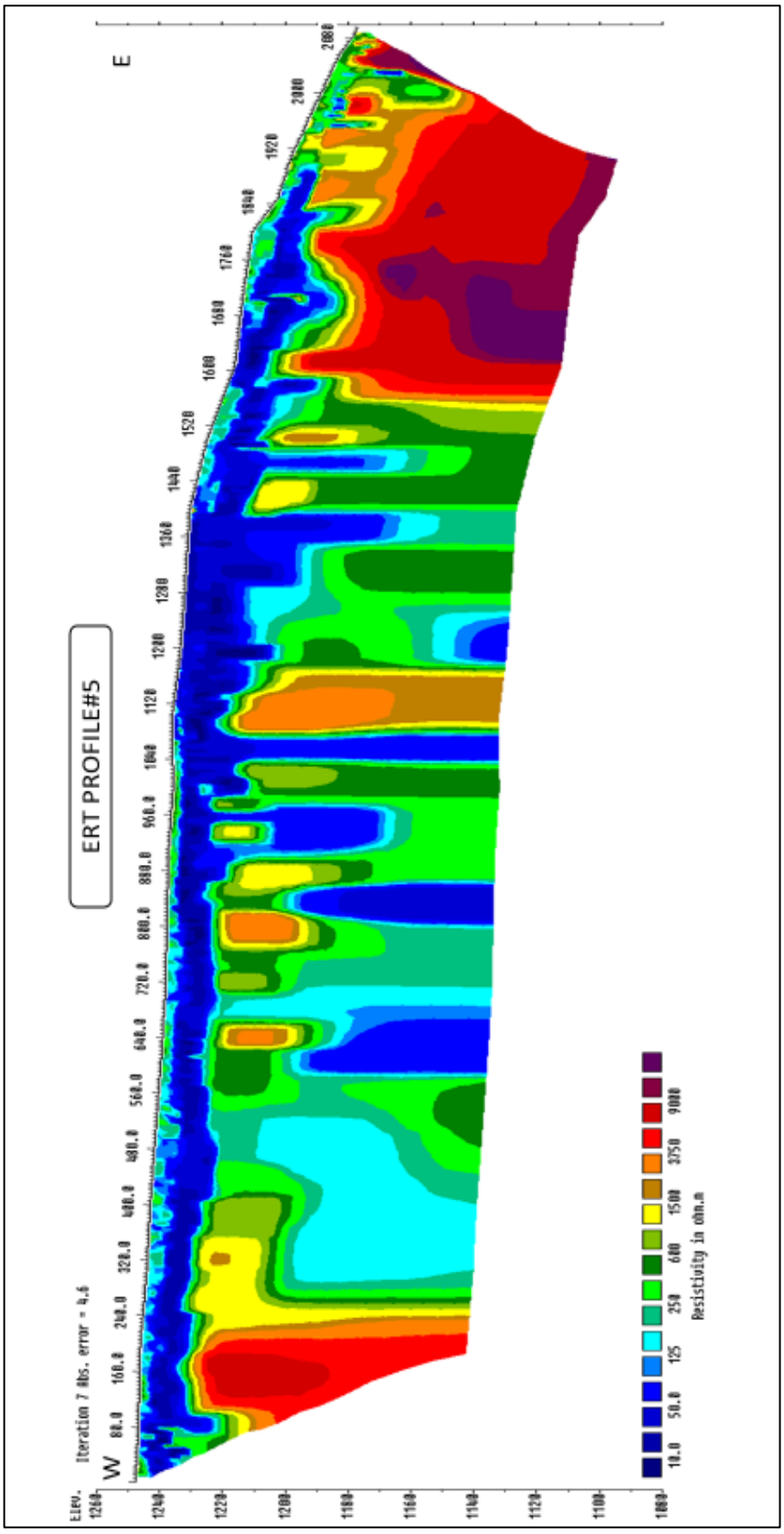

Figure 4.12. ERT profile #5. ERT model generated using 168 electrodes spaced at 5 ft apart with a total profile length of approximately 1260 ft.

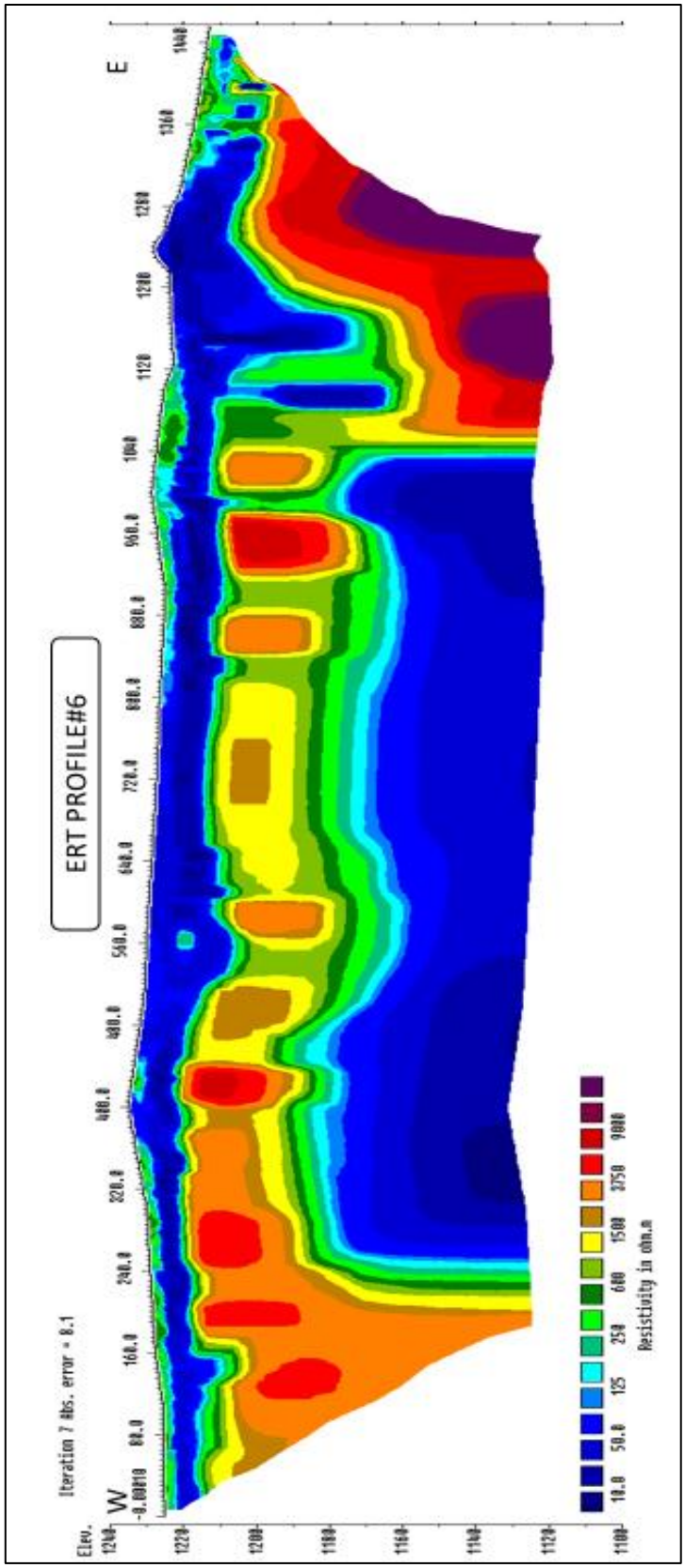

Figure 4.13. ERT model generated using 168 electrodes spaced at 5 ft apart with a total profile length of approximately1280 ft.

The geophones were placed in a straight line, at spacings of both 2.5 ft and 5 ft. Data acquired using a 5 ft interval should enable (theoretically) the user to image the subsurface to a depth in excess of 100 ft. Unfortunately, data quality, in karst terrain, often deteriorates with longer spacings due to smearing (caused mostly by variable depth to top-of-rock). In many instances, data acquired using a 2.5 ft spacing was superior to data acquired using a 5 ft spacing. Two offsets were used:10 ft and 30 ft. A sledgehammer (20 lbs.) and metal plate were used as the source for generating the surface waves.

MASW data acquired to determine the engineering properties of the subsurface to a depth of approximately 50ft. Thirteen (13) ERT traverses were selected to be presented in this study with MASW traverses acquired to constrain the ERT interpretation results (Figure 4.15).

4.2.2. MASW Data Processing. Processing of acquired MASW data was conducted using SurfSeis software from the Kansas Geological Survey (KGS). The purpose of the processing is to generate 1D (depth) shear-wave velocity profile.

To achieve this, three processing steps are required, including the upload of the basic field multichannel data records “shot gathers” (Figure 4.16) to the computer and converting the data from seismograph format to KGS format, the estimation of the fundamental-mode dispersion curves, and the inversion of these curves to obtain 1D (depth) and velocity Vs frequency plots.

Accurate estimation of fundamental-mode dispersion curve is a critical step in many shallow surface-wave methods (Gathers, J. I. et al., 2005). A simple multichannel processing technique used to mute the interfering seismic waves in the shot records is used to changes the amplitude of all or part of a trace before additional processing.

Table 4.1. Table shows the recommended (rule-of-thumb) data acquisition parameters for active MASW survey (Park et al., 2002).

Data Acquisition Parameters++ for Active MASW Survey (in ft)

****Most Recommended Values**

Depth (Z_{max})[1] (ft)	Source (S)[2] (lb)	Receiver (R)[3] (Hz)	Receiver Spread (RS) (ft)				SR Move[6] (dx)			Recording[8]				
			Length[4] (D)	Source Offset[5] (X_1)	Receiver Spacing (dx)		Lateral Resolution[7]			dt[9] (ms)	T[10] (sec)	Vertical Stack[11]		
					24-ch*	48-ch	High	Medium	Low			C	N	VN
≤ 5.0	≤ 1	4.5–100	5–15	1–15	0.2–0.6	0.1–0.3	1–2	2–4	4–12	0.5–1.0	0.5–1.0	1–3	3–5	5–10
	(1)**	**(40)**	**(10)**	**(2)**	**(0.3)**	**(0.2)**	**(1)**	**(2)**	**(4)**	**(0.5)**	**(0.5)**	**(3)**	**(5)**	**(10)**
5–15	1–5	4.5–40	5–45	1–9	0.2–2.0	0.1–1.0	1–2	2–4	4–12	0.5–1.0	0.5–1.0	1–3	3–5	5–10
	(5)	**(10)**	**(30)**	**(5)**	**(1.0)**	**(0.5)**	**(1)**	**(2)**	**(4)**	**(0.5)**	**(0.5)**	**(3)**	**(5)**	**(10)**
15–30	5–10	≤ 10	15–90	3–18	0.5–4.0	0.2–2.0	1–2	2–4	4–12	0.5–1.0	0.5–1.0	1–3	3–5	5–10
	(10)	**(4.5)**	**(50)**	**(10)**	**(2.0)**	**(1.0)**	**(1)**	**(2)**	**(4)**	**(0.5)**	**(1.0)**	**(3)**	**(5)**	**(10)**
30–60	≥ 10	≤ 10	30–180	6–36	1.0–8.0	0.5–4.0	1–2	2–4	4–12	0.5–1.0	1.0–2.0	1–3	3–5	5–10
	(20)	**(4.5)**	**(120)**	**(30)**	**(4.0)**	**(2.0)**	**(1)**	**(2)**	**(4)**	**(0.5)**	**(1.0)**	**(3)**	**(5)**	**(10)**
60–100	≥ 10	≤ 4.5	60–300	12–60	2–12	1–6	1–2	2–4	4–12	0.5–1.0	1.0–2.0	1–3	3–5	5–10
	(20)	**(4.5)**	**(200)**	**(40)**	**(8)**	**(4)**	**(1)**	**(2)**	**(4)**	**(1.0)**	**(1.0)**	**(3)**	**(5)**	**(10)**
100–150	≥ 10 **(20)**	≤ 4.5	100–450	20–90	4–18	2–9	1–2	2–4	4–12	0.5–1.0	1.0–3.0	1–3	3–5	5–10
	or passive	**(4.5)**	**(300)**	**(60)**	**(12)**	**(6)**	**(1)**	**(2)**	**(4)**	**(1.0)**	**(1.0))**	**(3)**	**(5)**	**(10)**
> 150	≥ 10 **(20)**	≤ 4.5	> 150	> 30	> 6.0	> 3.0	1–2	2–4	4–12	0.5–1.0	≥ 1.0	1–3	3–5	5–10
	or passive	**(4.5)**	**(450)**	**(100)**	**(20)**	**(10)**	**(1)**	**(2)**	**(4)**	**(1.0)**	**(2.0)**	**(3)**	**(5)**	**(10)**

++Values listed here are by no means definitive and required. There can always be a tolerance of, at least, ±20% to the most recommended values.

[1]maximum depth to be investigated, [2]weight of hammer in pounds, [3]natural frequency of geophone, [4]approximate total length of receiver spread ($D \approx mZ_{max}$ with $1 \le m \le 3$), [5]distance between source and the closest receiver($X_1 \approx \kappa D$ with $0.2 \le \kappa \le 1.0$), [6]distance in receiver spacing (dx) that the source (S) and receiver (R) setup moves after acquiring data at one location, [7]degree of lateral resolution being sought, [8]recording parameters for seismograph, [9]sampling interval in milliseconds (ms), [10]total recording time in seconds (sec), [11]number of stacking data in seismograph's memory before being saved under different conditions of calm (C), noisy (**N**), and very noisy (**VN**) environment, respectively, [12]acquisition filter (e.g., low-cut, high-cut, etc.), *24-channel acquisition system.

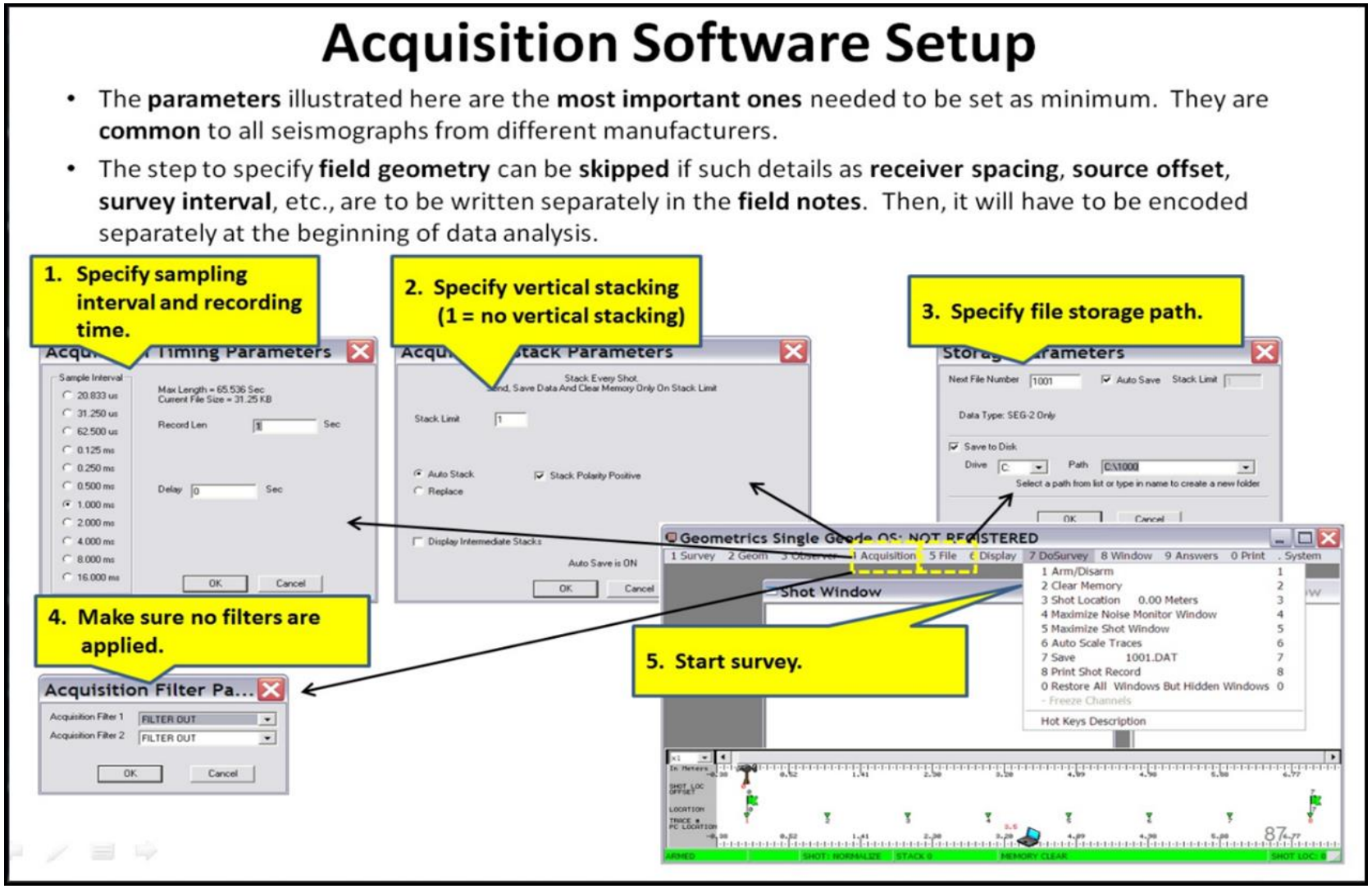

Figure 4.14. The figure illustrates how to setup the important parameters for the data acquisition software (Park et al., 2002).

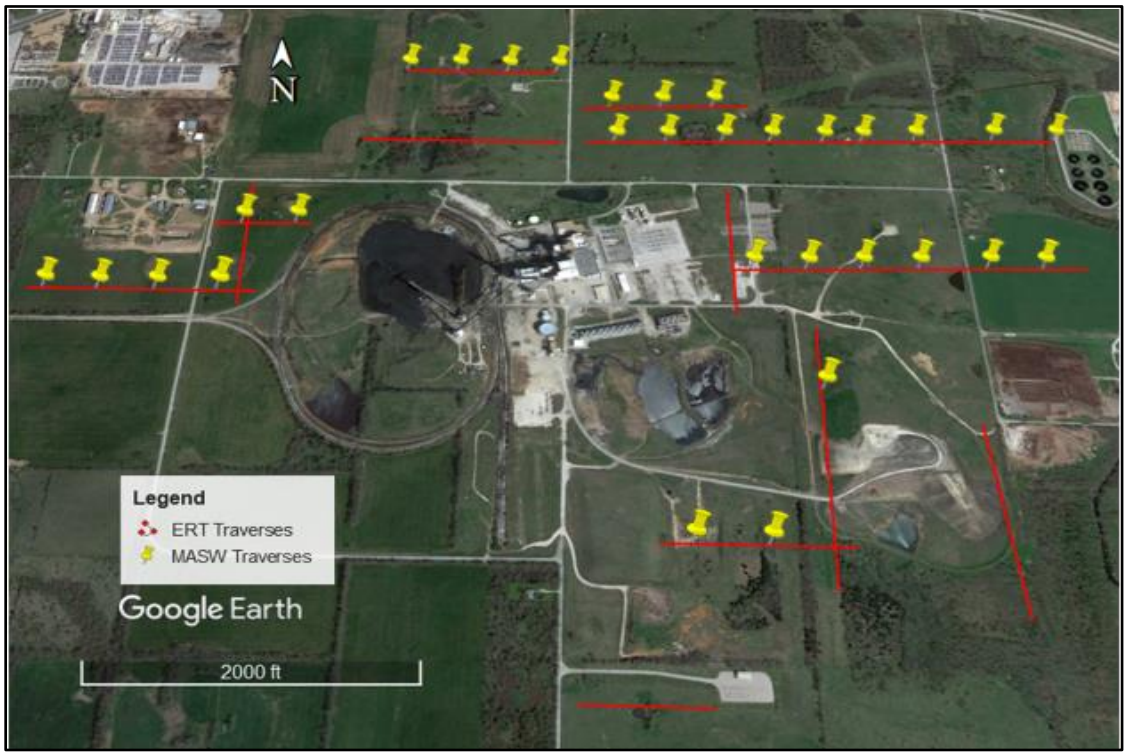

Figure 4.15. Location of acquired ERT traverses and MASW arrays in the study area.

Noisy and erroneous traces are given zero amplitude, and data (noise) before the first break, and the known refraction arrivals are also often reduced to zero amplitude.

The next step in MASW data processing is generating the dispersion image from the data after the muting process. This is done directly by the software, where it calculates phase velocities from the frequency records of the MASW data and extracts an aggregate dispersion curve from the overtone image (Figure 4.17).

After the generation of the dispersion curve, the high mode surface wave data is deleted to the extent possible to minimize noise, because steepness of the low frequency section (< 1.5 Hz) of the dispersion curves creates many computational instabilities during the inversion.

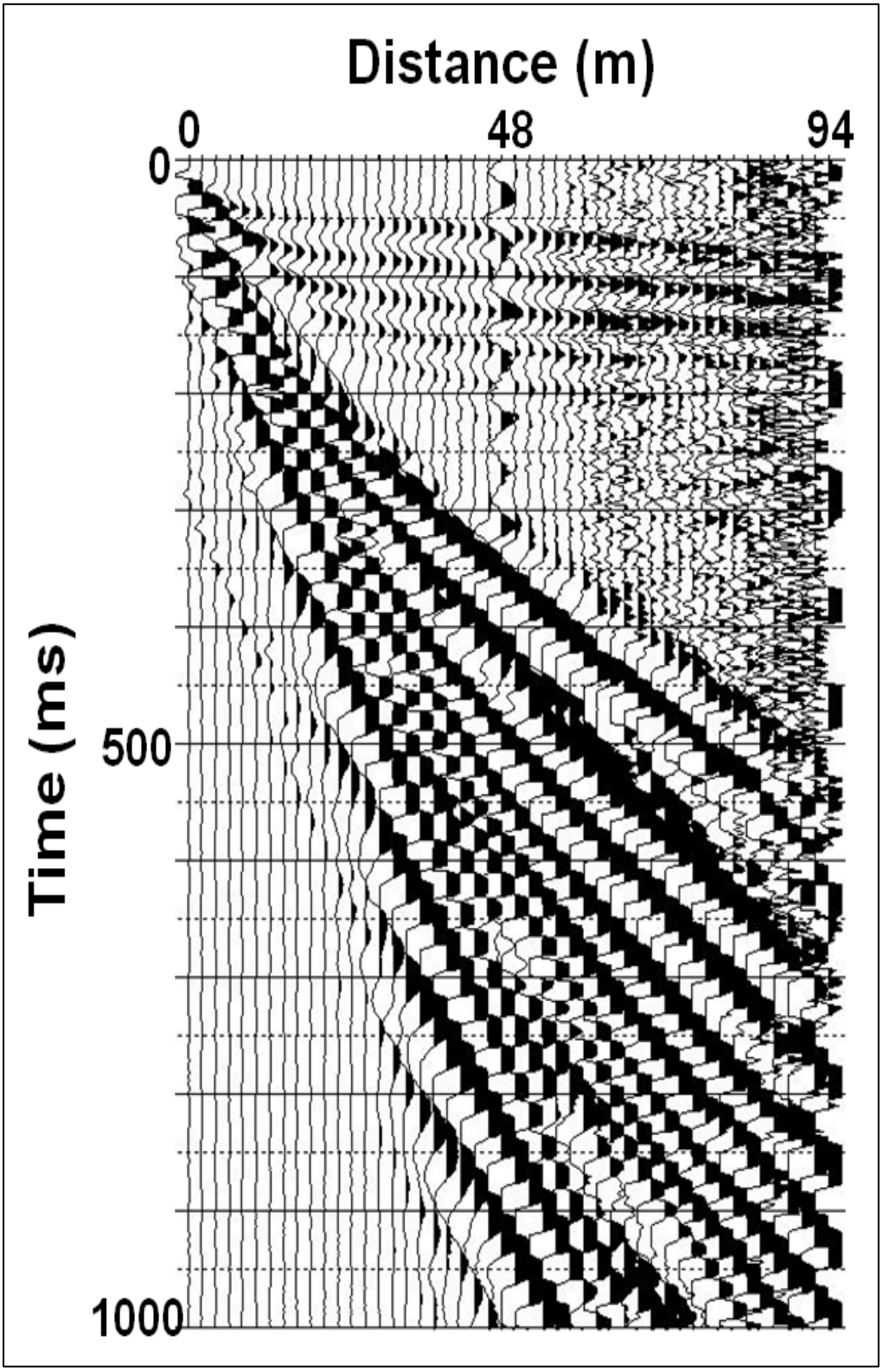

Figure 4.16. Illustration of the shot gathers, which shows that most of the depicted energy is fundamental mode surface wave energy.

Inversion of the curve is done by using least squares approach in the inversion submenu of the software to generate 1D (depth) vertical shear-wave velocity profile (Figure 4.18).

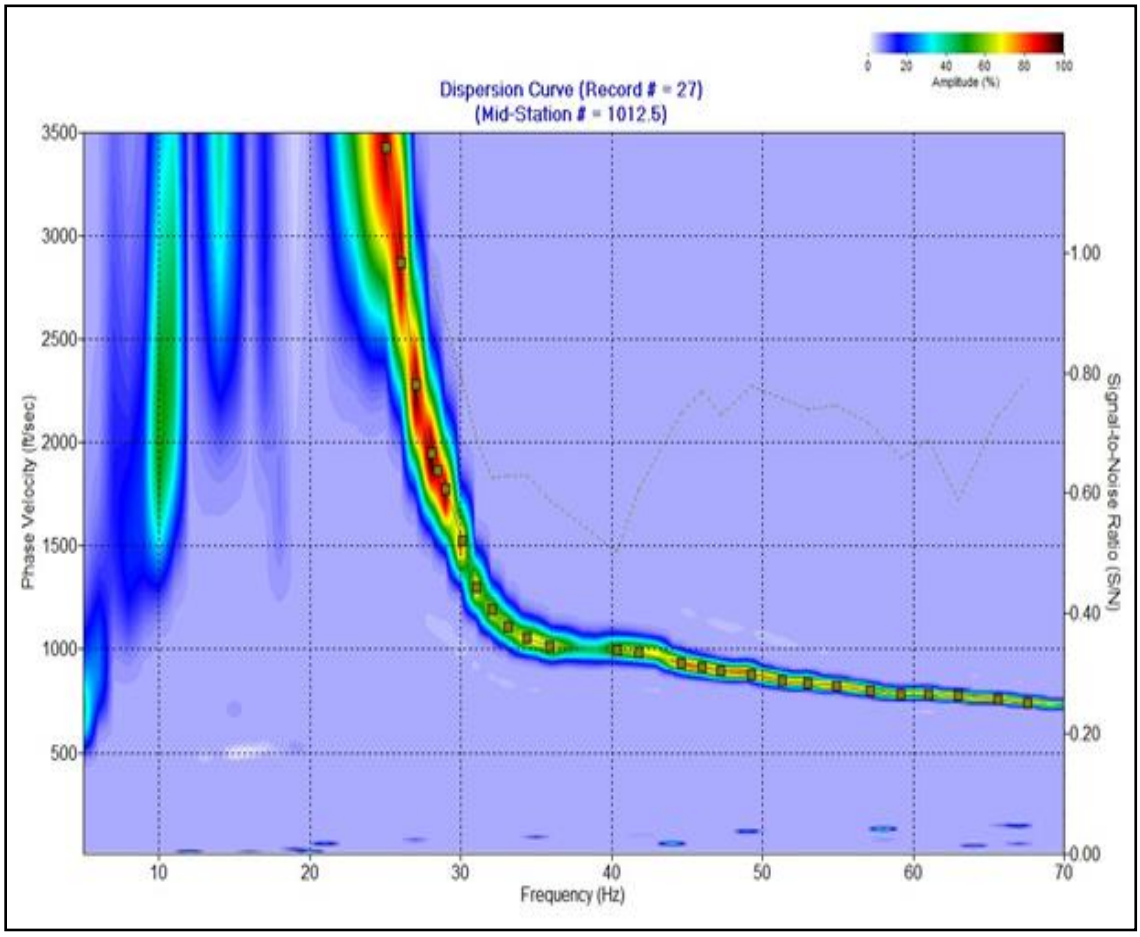

Figure 4.17. Dispersion curve from each record generated for phase velocity Vs frequency.

The inversion produces a final shear-wave velocity profile (step-ladder-shape), model dispersion curves (solid curve) and observed dispersion curves (dotted). If the final model dispersion curve matches the observed dispersion curve, the output shear-wave velocity profile is assumed to be reliable.

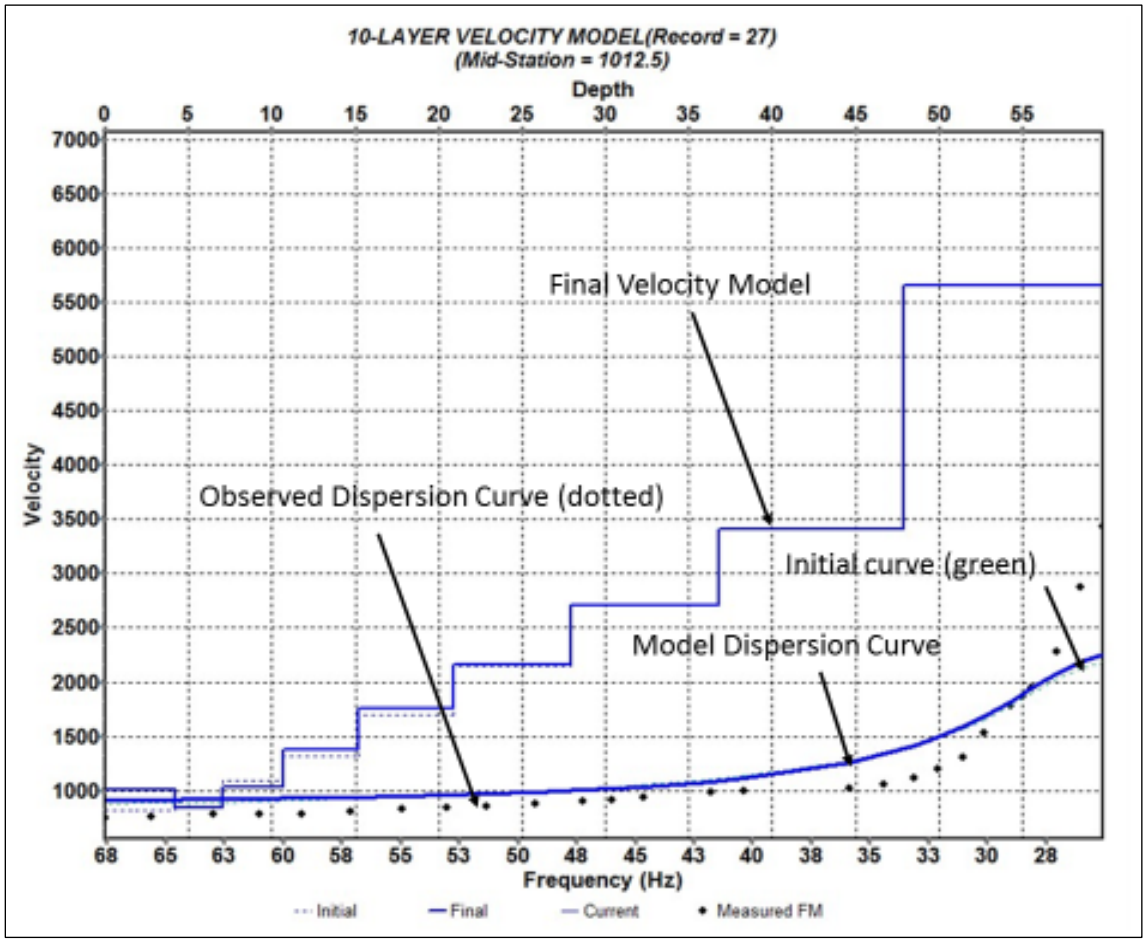

Figure 4.18. The dotted black line represents the observed dispersion curve as picked on the overtone image; the blue solid line represents the model dispersion curve; the green dotted line represents the initial curve, and the step-ladder-shape represents the final velocity model.

Data quality is monitored during all the steps of the MASW survey. During data acquisition, cables, electrodes and stakes were monitored for electrical connectivity and problems associated with them. Special attention was directed to the dispersion curve selection, and to the removal of the higher mode signal.

Comparing the deviation between the model dispersion curve and observed dispersion curve in the six examples (Figure 4.19 to Figure 4.24) presented in this research, indicates that the quality of data is good to excellent.

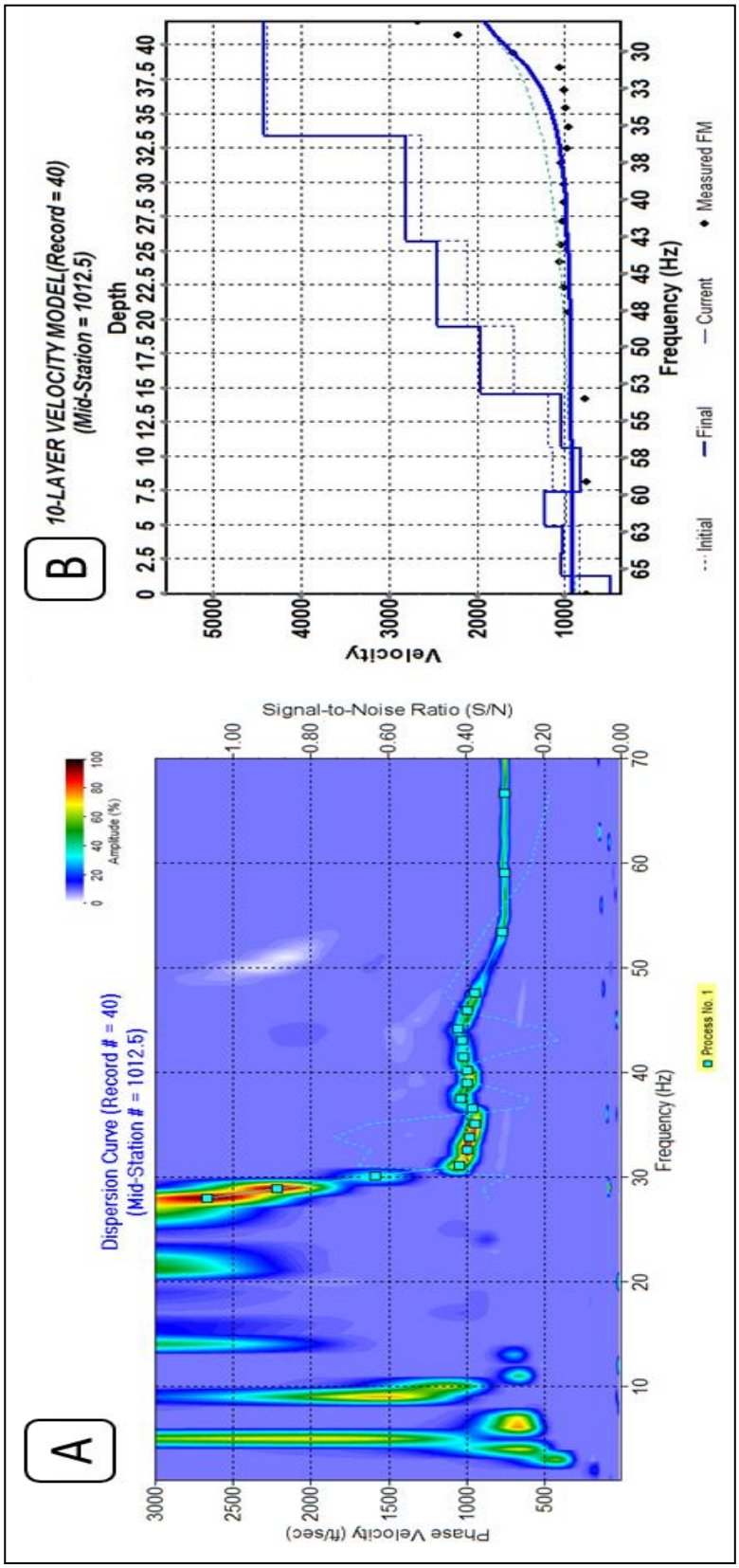

Figure 4.19. Profile (1) show the dispersion curve of the frequency versus phase velocity (A) and the shear-wave velocity profiles Vs frequency 1D depth curve (B).

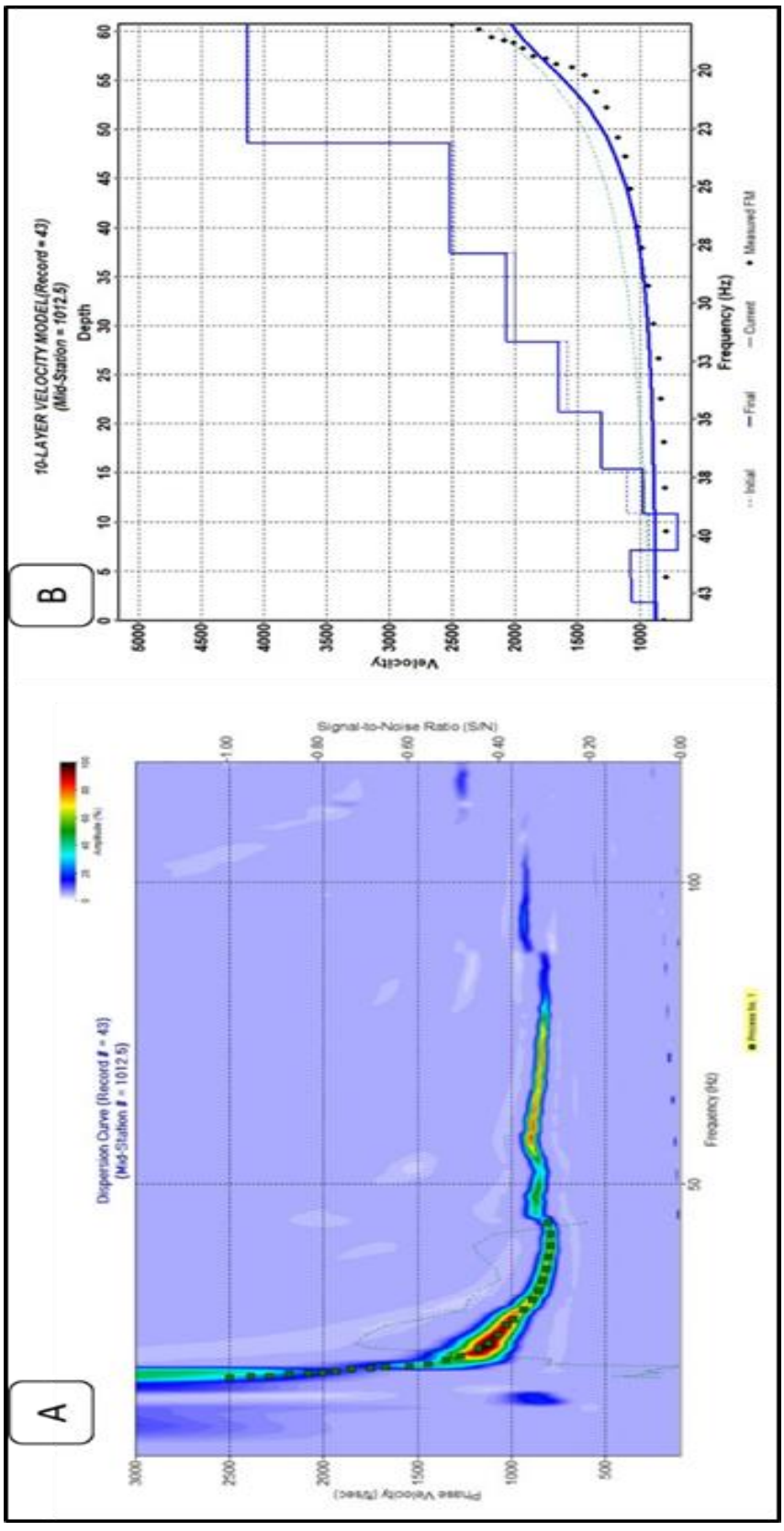

Figure 4.20. Profile (2) show the dispersion curve of the frequency versus phase velocity (A) and the shear-wave velocity profiles Vs frequency 1D depth curve (B).

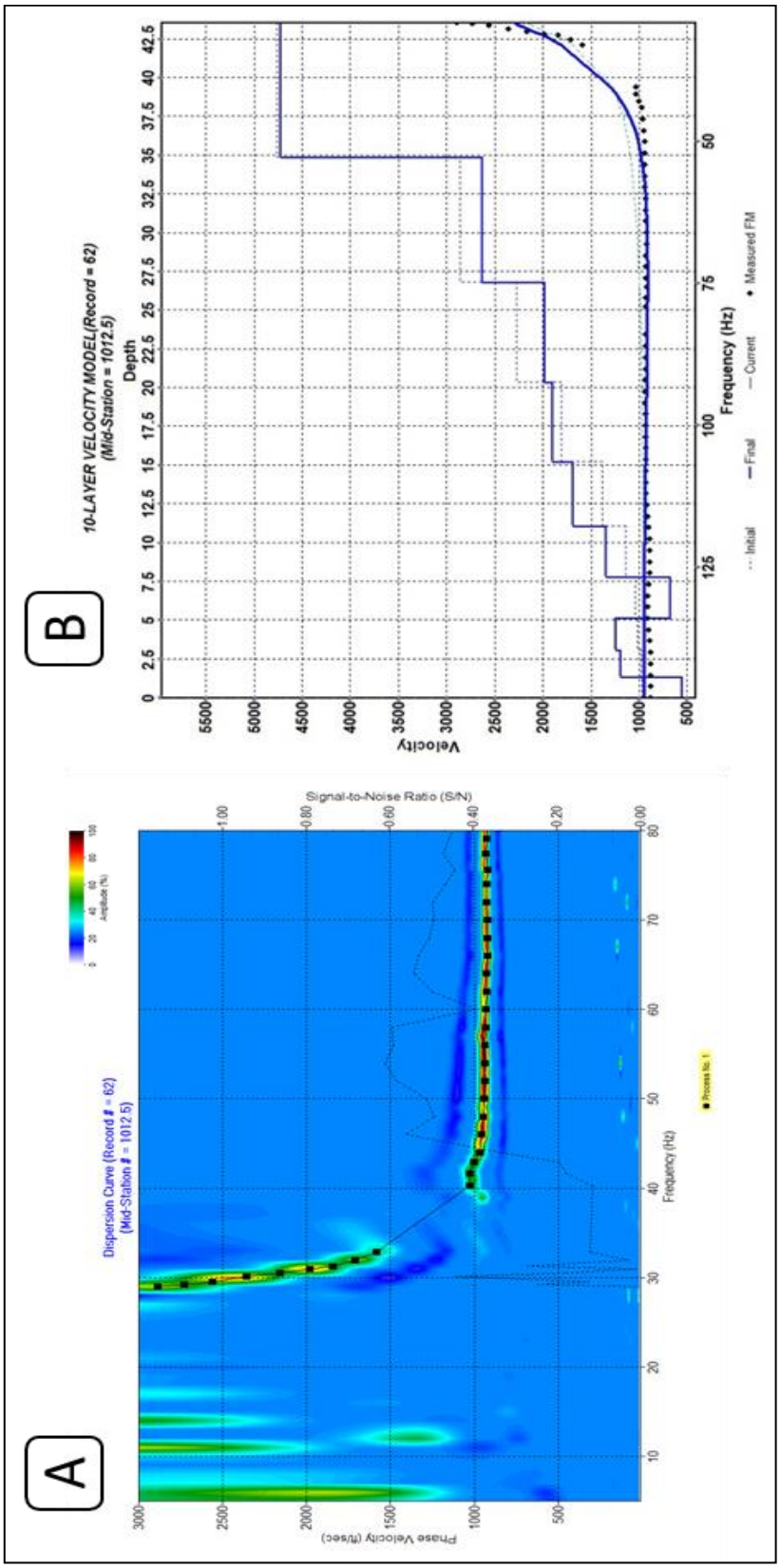

Figure 4.21. Profile (3) show the dispersion curve of the frequency versus phase velocity (A) and the shear-wave velocity profiles Vs frequency 1D depth curve (B).

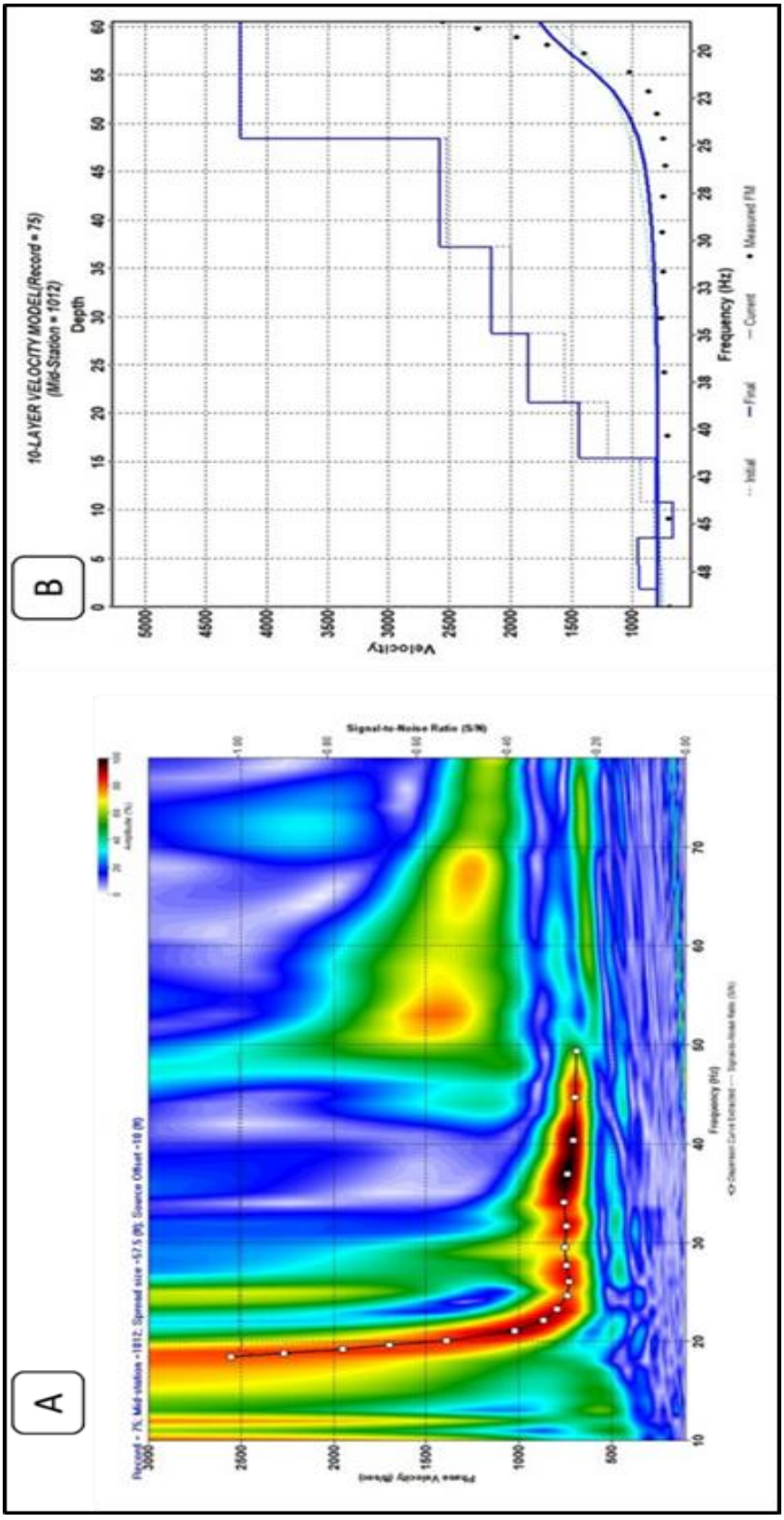

Figure 4.22. Profile (4) show the dispersion curve of the frequency versus phase velocity (A) and the shear-wave velocity profiles Vs frequency 1D depth curve (B).

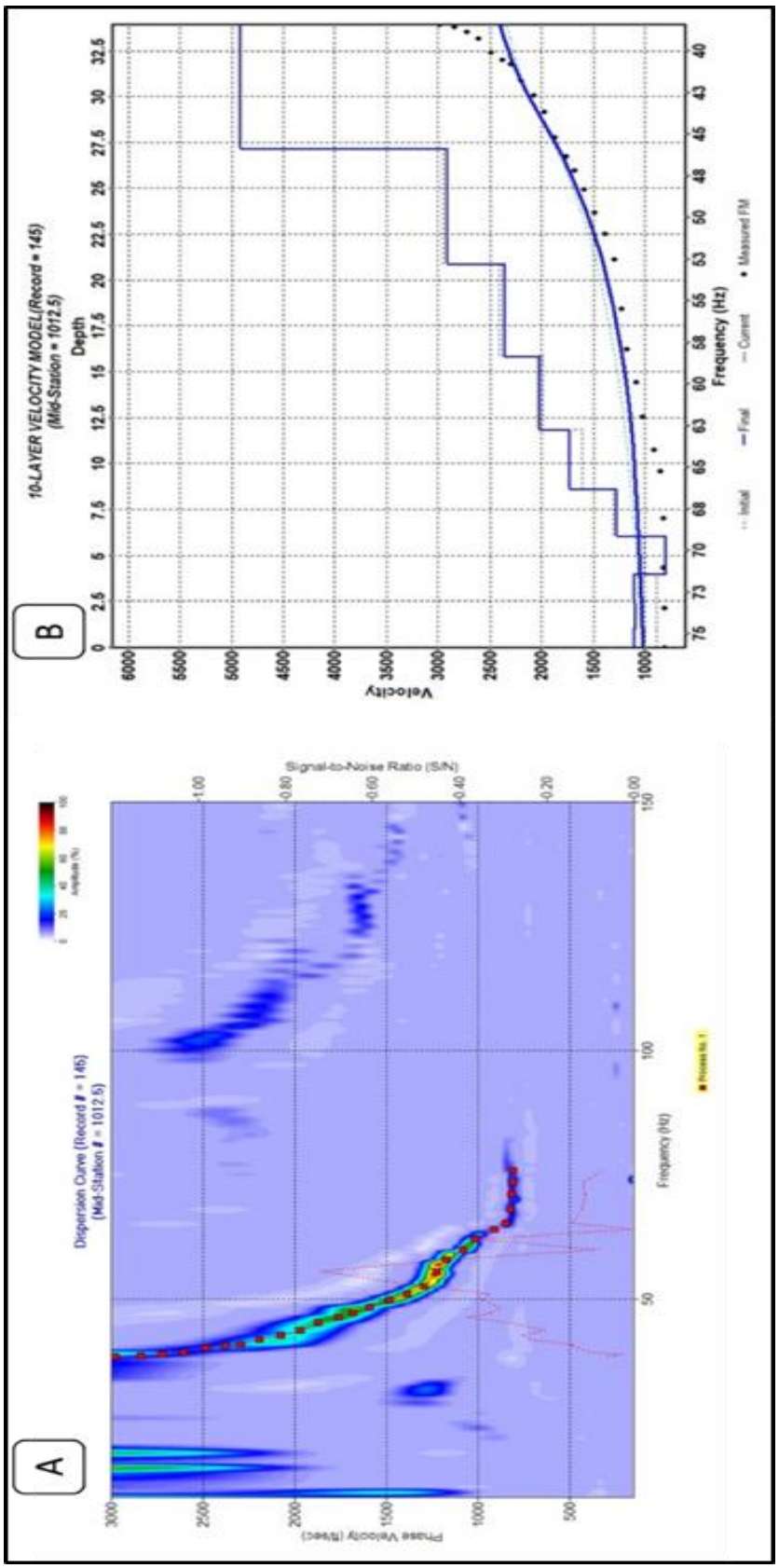

Figure 4.23. Profile (5) show the dispersion curve of the frequency versus phase velocity (A) and the shear-wave velocity profiles Vs frequency 1D depth curve (B).

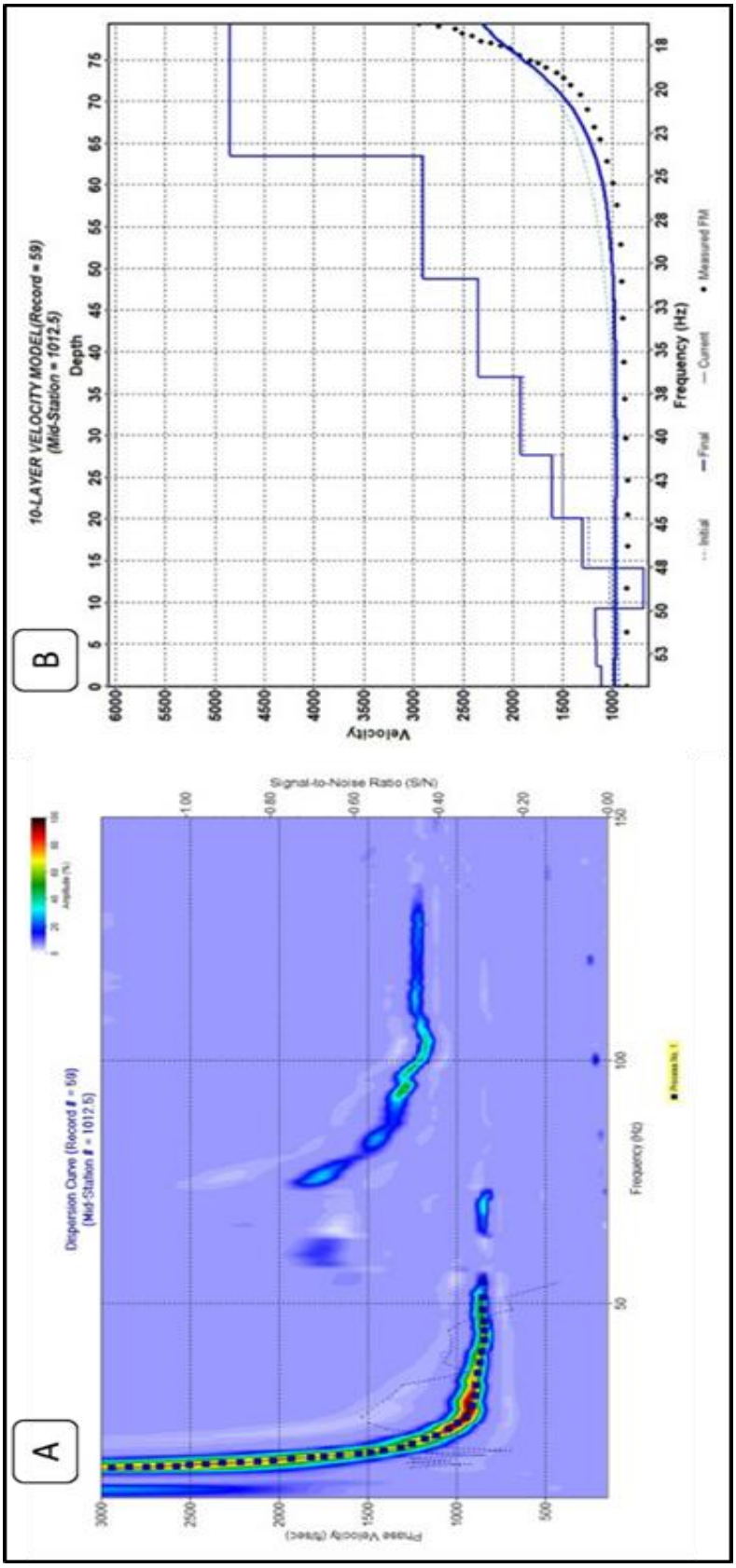

Figure 4.24. Profile (6) show the dispersion curve of the frequency versus phase velocity (A) and the shear-wave velocity profiles Vs frequency 1D depth curve (B).

5. INTERPRETATION AND DISCUSSION

The locations of the traverses of the ERT and MASW profiles selected for interpretation and discussion in this study of "imaging in karst terrain using the electrical resistivity tomography and multi-channel analysis of surface waves methods" are shown on a Google Earth image of the study area (Figure 5.1).

Figure 5.1. Google Earth image showing locations of the MASW and ERT traverses.

The interpretations and discussions in this study focus on seven (7) ERT profiles and two (2) MASW data sets which collectively illustrate the signatures of both man-made and the natural zones of anomalously low resistivity within bedrock. Anomalously low resistivity is defined herein as rock characterized by resistivity values less than 125 Ω·m.

The average resistivity values of earth material (as per Table 5.1) was used as a guide for the ERT interpretation.

The MASW data were acquired in proximity to the ERT traverses and used to constrain and verify the ERT interpretations. The NEHRP shear-wave velocity classification table for soils and rocks (Table 5.2) was used as a guide for interpreting the MASW shear-wave velocity profiles.

Table 5.1. Typical resistivity values for different subsurface materials (Anderson, 2015).

Earth Material	Resistivity, Average or Range (Ω.m)
Moist Soil	< 125
Dry Soil	> 125
Moist weathered and/or fractured rock	> 125 < 600
Fractured rock with moist piped clay-fill	< 125
Intact rock or very dry rock	> 600

Table 5.2. Shear-wave velocity (Vs) of some earth materials (NEHRP, 1997).

Earth Material	Average Shear-wave Velocity
Hard rock	>5000 ft/sec (> 1500 m/sec)
Rock	2500-5000 ft/sec (750-1500 m/sec)
Very dense soil and soft rock	1200-2500 ft/sec (360-750 m/sec)
Stiff soil	600-1200 ft/sec (180-360 m/sec)
Soft soil	<600 ft/sec (<180 m/sec)

ERT Example 1:

ERT profile 1 is oriented west–east (Figure 5.1 & Figure 5.2). The superposed black solid line represents the interpreted top-of-rock and corresponds approximately to the 125 Ω·m contour interval. The contact (as interpreted) between the moist soil and the

underlying moist soft rock (resistivity < 125 Ω·m) in proximity to anomaly 1 cannot be confidently identified on the ERT profile 1 because the moist soil and moist soft rock at the contact depth have similar resistivity values, presumably because the shallow rock is moist and intensely weathered with piped clay infill.

ERT anomaly 1 on the ERT profile 1 is approximately 85 ft wide at the interpreted top-of rock (elevation 1218 ft) and narrows down to ~50 ft (elevation 1200 ft) to a depth 18 ft from the top-of-rock, with a total length of 18 ft of the anomaly. Anomaly 1 underlies a natural stream bed running north-south (the blue lines in Figure 5.2).

ERT anomaly 1 on the ERT profile 1 is attributed to the seepage water from the overlying stream bed into the subsurface. The anomaly as interpreted, is "natural" in origin. Inasmuch as the stream bed has existed for thousands of years (since glacial times), shallow rock is believed to have been intensely weathered over time. The minimum resistivity of ERT anomaly 1 on the ERT profile 1, as interpreted, is less than ~75 Ω·m, and the overall resistivity is between 75 and 125 Ω·m. Note that the resistivity of rock in proximity to the highlighted anomaly increases away from the anomaly and with depth of burial and is much broader than the stream bed. This indicates that moisture flow from the stream bed is both vertical and lateral. ERT anomaly 2 on the ERT profile 1 is approximately 50 ft wide at the interpreted top-of-rock (elevation 1234 ft) and pinches out at a depth of ~12 ft (elevation 1223 ft) from the top-of-rock, with a total length of 12 ft of the anomaly (Figure 5.2).

Anomaly 2 underlies a roadway with drainage ditches. The contact (as interpreted) between the moist soil and the underlying moist soft rock in proximity to anomaly 2 cannot be confidently identified on the ERT profile 1 because the moist soil and moist soft rock at

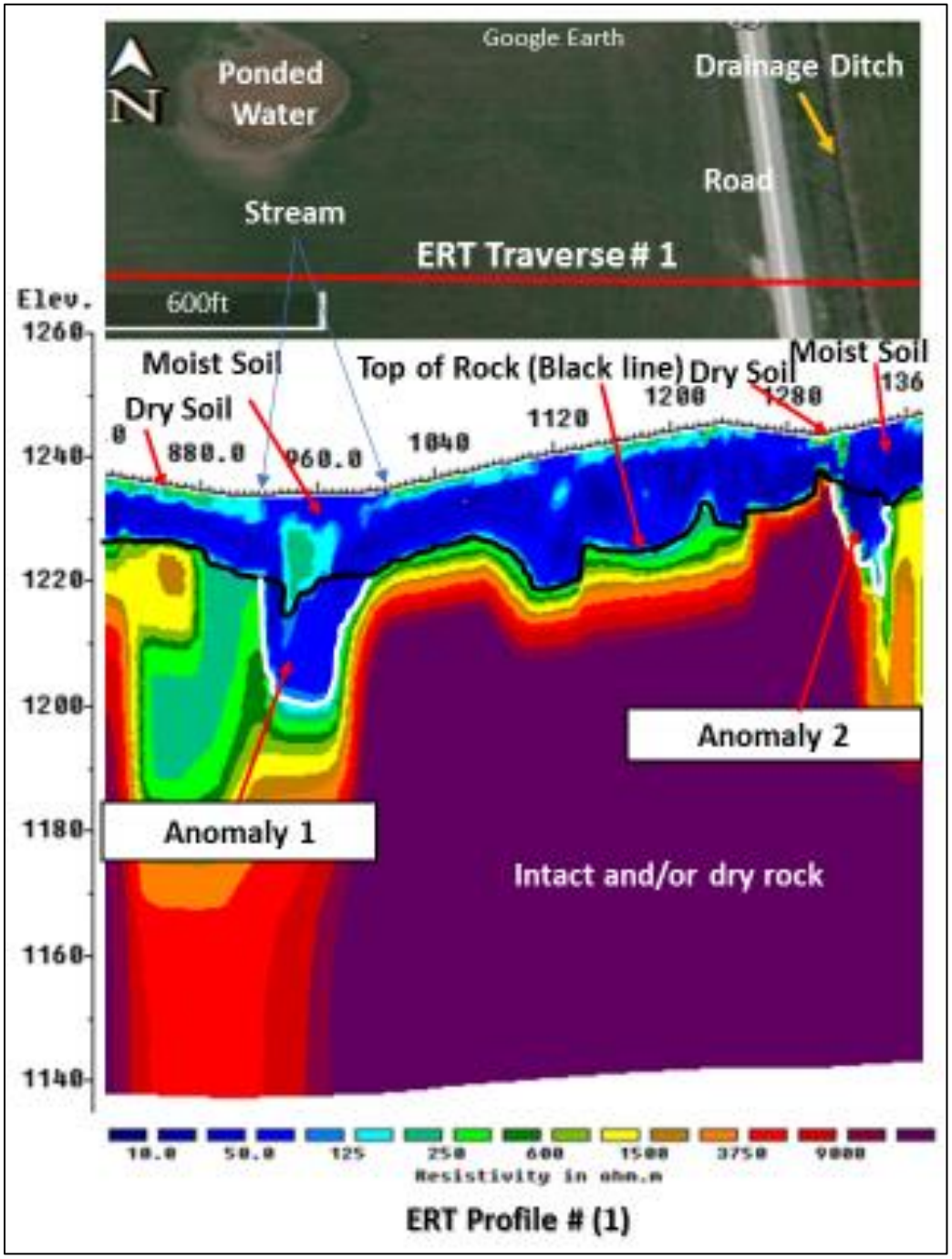

Figure 5.2. Google Earth image showing the ERT traverse location, water pond, the stream, roadway and drainage ditch. Interpretations are superposed upon the ERT profile 1.

the contact depth has similar resistivity values, presumably because the shallow rock is moist and intensely weathered with piped clay infill. The minimum resistivity of ERT

anomaly 2 on the ERT profile 1, as interpreted, is less than ~25 Ω·m, and the overall resistivity is between 25 and 50 Ω·m. Note that the resistivity of rock in proximity to the highlighted anomaly increases away from the anomaly and with depth of burial and is much broader than the roadway and ditches. This indicates that moisture flow is both vertical and lateral.

ERT anomaly 2 on the ERT profile 1 is attributed to the seepage water from the roadway and drainage ditch into subsurface. The anomaly as interpreted, is "man-made" in origin. Since the roadway has existed for less than 50 years, it is highly unlikely that shallow rock beneath the roadway has been intensely weathered by the seeping water (although it probably contains piped clay). It worth noting that the “natural in origin” anomaly 1 is larger in size and extends to a greater depth compared to the “man-made” anomaly 2. This could be attributed, in part, to the fact that shallow bedrock beneath the stream has probably been weathered by seeping water for thousands of years and is more porous and permeable than shallow bedrock beneath the drainage ditches of anomaly 2. On the other hand, as noted, anomaly 2 has lower minimum resistivity values than anomaly 1 (less than 25 Ω·m). This could be attributed, in part, to the thesis that moisture and piped clay flow more rapidly into the subsurface beneath the stream bed in anomaly 1 than their flow into subsurface in anomaly 2. Hence, anomaly 1 is more volumetrically larger and its minimum resistivity values are slightly higher than anomaly 2.

MASW data set 1 was acquired along the ERT traverse 1 at the 1400 ft tie point. The shear-wave velocity for soil in the study area, as interpreted, is < 1250 ft/s, the shear-wave velocity for soft (weathered) rock, as interpreted, is between 1250 ft/s and 2500 ft/s; the shear-wave velocity for rock, as interpreted, is > 2500 ft/s (Figure 5.3).

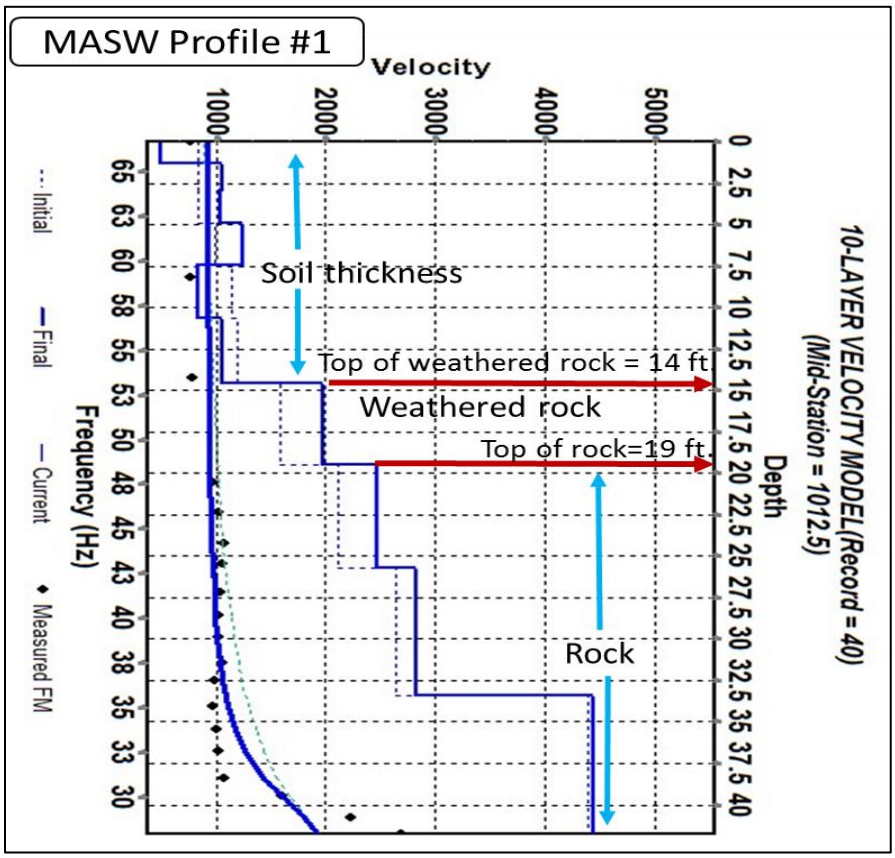

Figure 5.3. MASW shear wave velocity profile 1 illustrating soil thickness, depth to top of weathered rock and weathered rock and top-of-rock. Velocity is in ft/s.

At the tie point, the soil thickness as interpreted on the ERT profile 1 is ~12 ft. The soil thickness (depth to soft or weathered rock) as interpreted on the MASW shear-wave velocity profile is ~14 ft. The interpreted top-of-rock (shear-wave velocity greater than 2500 ft/s) on the shear-wave velocity profile is at a depth of 19 ft. The difference between the ERT and MASW estimates of soil thickness can be attributed to the fact that the ERT estimate is based on moisture content (resistivity) whereas the MASW estimate is based on shear strength (shear-wave velocity). Also, the MASW data were acquired using a 115 ft long array of geophones. As a result, the MASW shear wave velocity profile represents the average shear wave velocity of the subsurface beneath the array of geophones as opposed to representing the shear wave velocity of the subsurface precisely at the tie point.

ERT Example 2:

ERT profile 2 is west–east oriented (Figure 5.1 & Figure 5.4). The superposed black solid line is the interpreted top-of-rock and corresponds approximately to the 125 Ω·m contour interval. The contact (as interpreted) between the moist soil and the underlying moist soft rock (resistivity < 125 Ω·m) in proximity to anomaly 1 cannot be confidently identified on the ERT profile 2 because the moist soil and moist soft rock at the contact depth have similar resistivity values, presumably because the shallow rock is moist and intensely weathered with piped clay infill.

ERT anomaly 1 on the ERT profile 2 is approximately 70 ft wide at the interpreted top-of-rock (elevation ~1220 ft) and thins at the bottom to 40 ft (elevation ~1200 ft) from the top-of-rock, with a total length of the anomaly ~20 ft. The minimum resistivity of anomaly 1, as interpreted, is less than 100 Ω·m, but generally, the resistivity values are between 100 – 125 Ω·m. Anomaly 1 as interpreted, underlies a natural stream bed that has probably existed for thousands of years (since glacial times), thus, shallow rock is believed to have been intensely weathered over time (Figure 5.4). Anomaly 1 on the ERT profile 2 as interpreted, indicates that the stream bed is active, but the vertical moisture and clay material supply is intermittent, and that the anomaly receives its major supply from the seepage water and piped clay from lateral sources Anomaly 1 on the ERT profile 2, as interpreted is “natural” in origin. The resistivity increases with depth of burial to more than 250 Ω·m to a depth of 25 ft (elevation 1196).

It is likely that the resistivity in this area is controlled by the seasonal variation of moisture content, which eventually slows weathering. Water that seems to contribute to the low resistivity is seeping from sources and pathways at the vicinity of the stream bed.

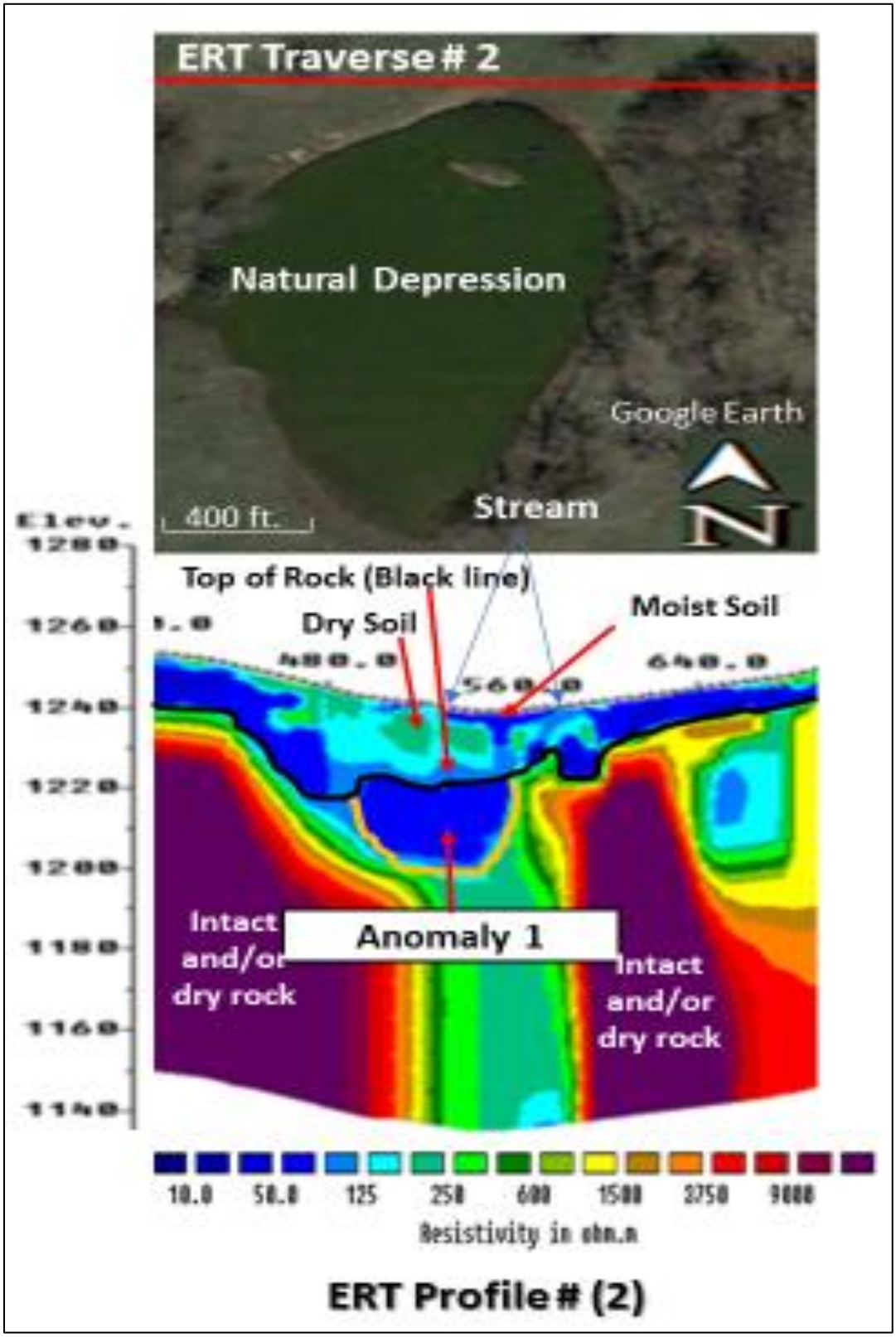

Figure 5.4. Google Earth image showing the ERT traverse location and the natural depression superposed upon the ERT profile 2.

ERT Example 3:

ERT profile 3 is oriented west–east (Figure 5.1 & Figure 5.5). The superposed black solid line is the interpreted top-of-rock and corresponds approximately to the 125 Ω·m contour interval. The contact (as interpreted) between the dry soil and the underlying weathered rock (resistivity > 125 Ω·m) in proximity to anomaly 1 cannot be confidently identified on the ERT profile 3 because the dry soil and weathered rock at the contact depth have similar resistivity values, presumably because the shallow rock is weathered and porous.

ERT anomaly 1 on the ERT profile 3 is approximately 20 ft wide at the interpreted top-of-rock (elevation 1200 ft) and broadens to 40 ft wide at a depth of 56 ft (elevation 1144 ft) from the top-of-rock. The total length of the anomaly is 62 ft from the top-of-rock (elevation 1200 ft and 1138 ft). The minimum resistivity values (~75 Ω·m) associated with the anomaly are observed at a depth of ~12 ft from the top-of-rock (elevation ~1188 ft). Resistivity range of the anomaly varies between ~75 and ~150 Ω·m. The resistivity of the anomaly increases with depth of burial to more than 125 Ω·m (below elevation 1138 ft). ERT anomaly 1 on the ERT profile 3, as interpreted, underlies a natural stream bed running north-south (the blue lines in Figure 5.5). The anomaly as interpreted, is moist weathered rock, filled with clay. Inasmuch as the stream bed has existed for thousands of years (since glacial times), shallow rock is believed to have been intensely weathered (Figure 5.5).

ERT anomaly 1 on the ERT profile 3 is attributed to the seepage of the stream bed water and overlying depression into subsurface. The anomaly is interpreted as "natural" in origin, and it is likely that water and clay supply is not enough to impact the underlying

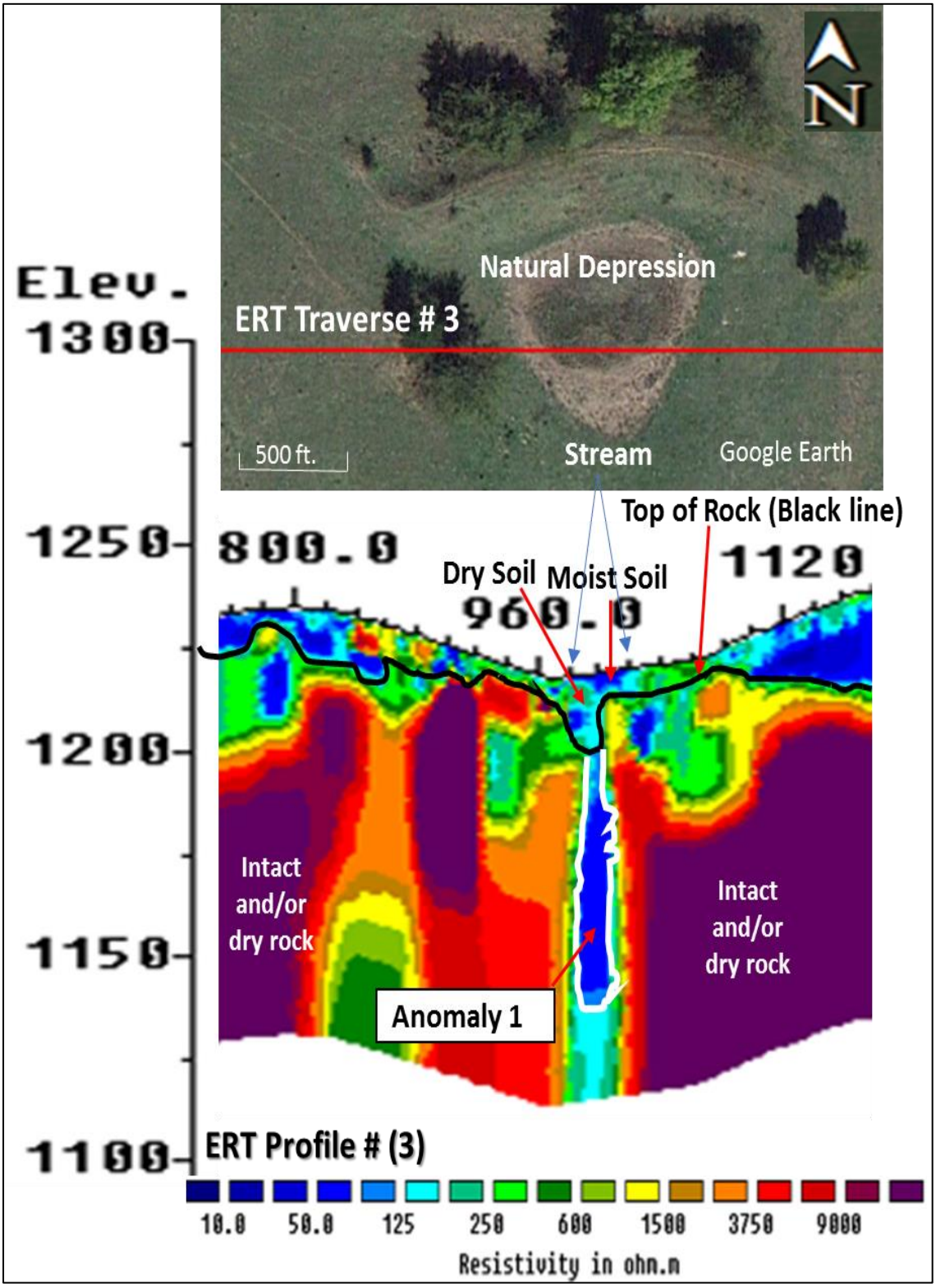

Figure 5.5. Google Earth image showing the ERT traverse location and the natural depression superposed upon the ERT profile 3.

rock, or it drains very fast before seeping into subsurface. Moreover, the shallow rock is likely less porous and less fractured than the underlying rock. The anomaly, as interpreted, indicates that flow pathways are vertical and lateral, even though they are intermittent.

ERT Example 4:

ERT profile 4 is north-south oriented (Figure 5.1 & Figure 5.6). The superposed black solid line is the approximated top-of-rock, which is extremely variable but is generally considered to correspond to the 125 Ω·m contour interval. The contact (as interpreted) between the moist soil and the underlying moist soft rock (resistivity < 125 Ω·m) in proximity to anomaly 1 cannot be confidently identified on the ERT profile 4 because the moist soil and moist soft rock at the contact depth have similar resistivity values, presumably because the shallow rock is moist and intensely weathered with piped clay infill.

Anomaly 1 on the north–south oriented ERT Profile 4, as interpreted, is ~15 ft wide at the top-of-rock (1238 ft elevation). The width of the anomaly increases progressively with depth to 80 ft at a depth of ~90 ft (elevation of 1148 ft) from top-of-rock, with a length more than 90 ft for the anomaly (Figure 5.6). The base of the anomaly (as defined by the 125 Ω·m contact) is not observed on Figure 5.6, so the maximum depth of the anomaly cannot be determined. The minimum resistivity values (~10 Ω·m) associated with the anomaly are observed at a depth of ~47 ft from the top-of-rock. Resistivity range of the anomaly varies between ~10 and ~50 Ω·m. This feature as interpreted, is one of the prominent west-east solution-widened joints that characterizes the study area. The joint is clay-filled, and resistivity of the anomaly decreases further with depth to less than 10 Ω·m.

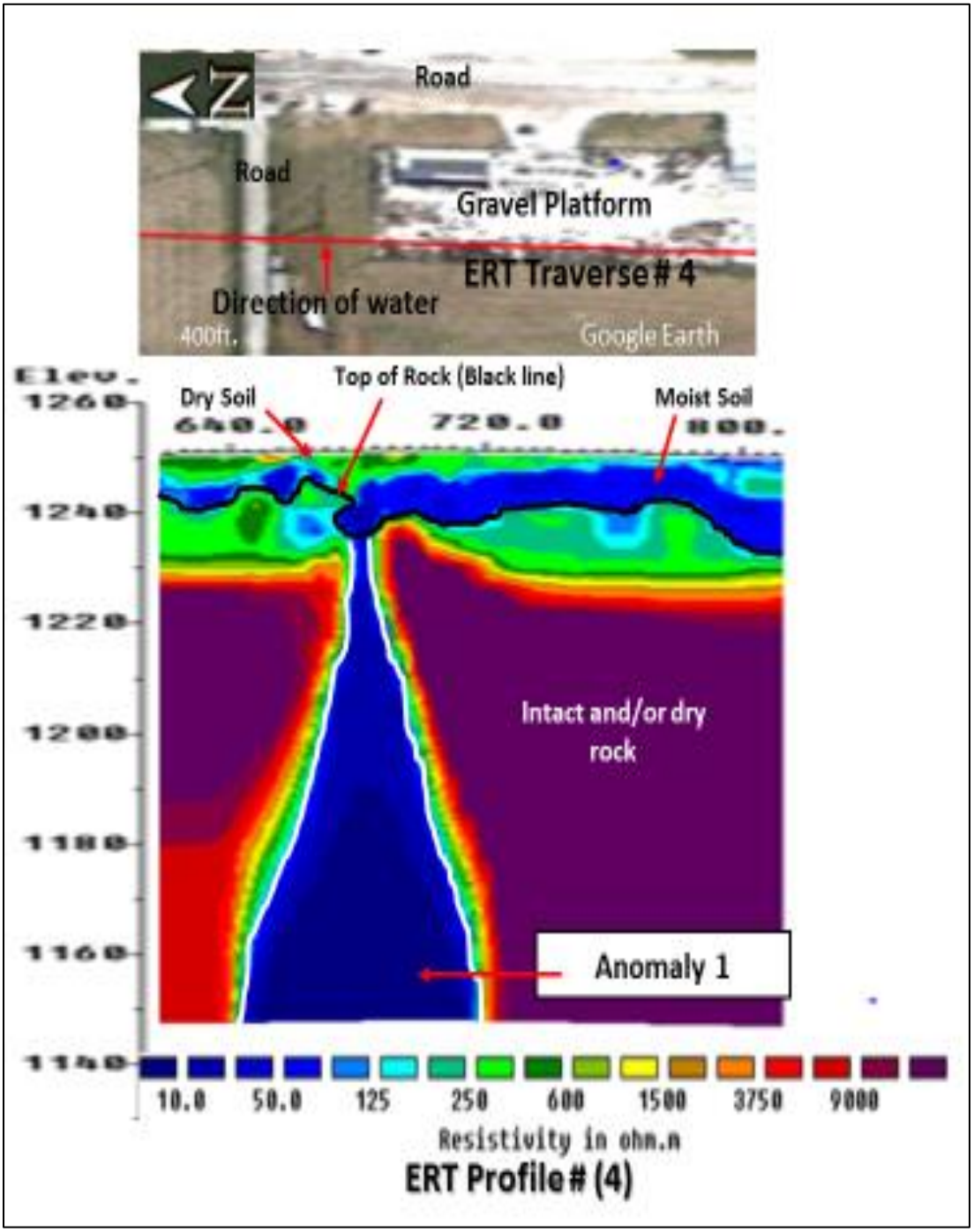

Figure 5.6. Google Earth image showing the ERT traverse location and the gravel platform. Interpretation superposed upon the ERT profile 4.

ERT anomaly 1 on the ERT profile 4 is interpreted as "man-made" in origin. Google earth images from 1997 to 2019 revealed that the location of the acquired ERT

traverse 4 was occupied by buildings and structures that were established on laid-out gravel platform. The consecutive Google earth images illustrated that the buildings were removed, and the gravel platform diminish gradually and completely disappeared, as shown in the most recent Google earth image (2019).

Water is flowing from west to east in the vicinity of the ERT traverse and across the gravel platform into a north-south drainage ditch (Figure 5.6). Water and fine earth material infiltrate the gravel platform into the jointed subsurface soft rock. Excess water flow further east into the drainage ditch, and eventually seeps laterally and vertically into the subsurface, causing the anomalously low resistivity values.

ERT Example 5:

ERT profile 5 is north-south oriented (Figure 5.1 & Figure 5.7). The superposed black solid line is the approximated top-of-rock and corresponds approximately to the 125 Ω·m contour interval. The contact (as interpreted) between the moist soil (resistivity < 125 Ω·m) and the underlying moist soft rock in proximity to anomaly 1 cannot be confidently identified on the ERT profile 5 because the moist soil and moist soft rock at the contact depth have similar resistivity values (between 25–75 Ω·m), presumably because the shallow rock is moist and intensely weathered with piped clay infill.

ERT anomaly 1 on the north-south oriented ERT Profile 5 is ~35 ft wide, as interpreted at the top-of-rock (elevation 1210 ft). The width of anomaly 1, as interpreted, slightly broadens with depth to 60 ft at a depth of 65 ft (1150 ft elevation) from the top-of-rock, with a length of more than 80 ft for the anomaly (Figure 5.7). The base of the anomaly (as defined by the 125 Ω·m contact) is not observed on Figure 5.7, so the maximum depth of the anomaly cannot be determined.

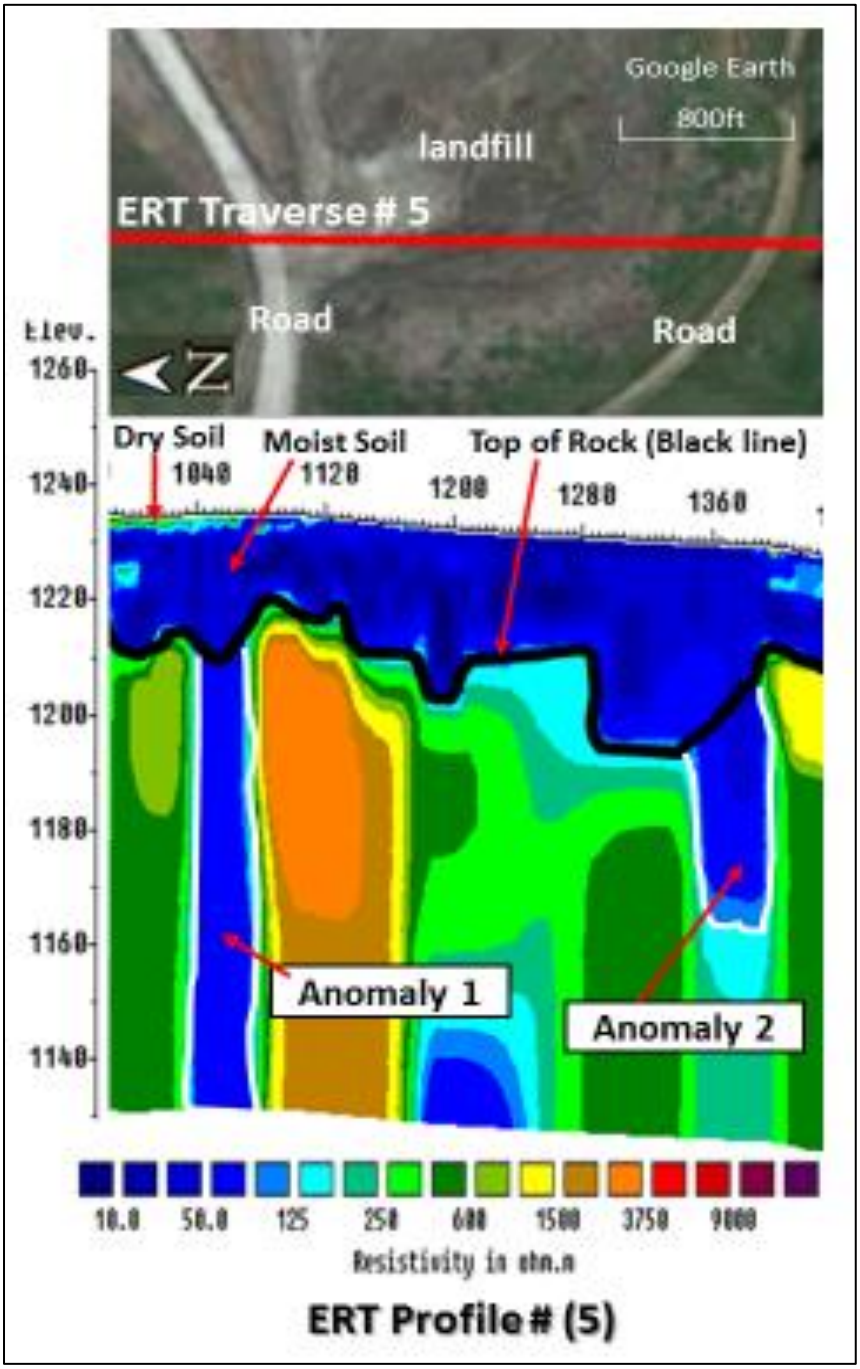

Figure 5.7. Google Earth image showing the ERT traverse location and the roads and drainage ditch. Interpretation superposed upon the ERT profile 5.

The minimum resistivity values (less than 75 Ω·m) associated with anomaly 1 are observed at a depth of ~35 ft from the surface, at the top-of-rock. Rocks of the study area are pervasively jointed, fractured and weathered limestones that often solution-widened

and clay infilled. The minimum resistivity values of anomaly 1 on the ERT profile 5 as interpreted, is less than 75 Ω·m, and underlies a 25 ft wide roadway surrounding landfill. Anomaly 1 on the ERT profile 5 as interpreted, is "man-made" in origin, is caused by seepage rainwater, run-off, water conveyed by roads and ditches and the water drainage system into subsurface, at the toe of the landfill via vertical and horizontal pathways.

ERT anomaly 2 on the ERT profile 5 as interpreted, is ~50 ft wide at the top-of-rock (elevation 1200 ft) and narrows down to ~40 ft at a depth of 38 ft (elevation 1162 ft) from the top-of-rock, with a total length of 38 ft (Figure 5.7). The contact (as interpreted) between the moist soil (resistivity < 75 Ω·m) and the underlying moist soft rock in proximity to anomaly 2 cannot be confidently identified on the ERT profile 5 because the moist soil and moist soft rock at the contact depth have similar resistivity values (between 50 – 75 Ω·m), presumably because the shallow rock is moist and intensely weathered with piped clay infill.

The minimum resistivity values associated with anomaly 2 on the ERT profile 5 (less than 50 Ω·m) are observed at the depth of the top-of-rock. Generally, resistivities of anomaly 2 ranges between 50 and 125 Ω·m. The feature as interpreted, is one of the prominent west-east solution-widened joints that characterizes the study area. The joint is clay-filled, and resistivity of the anomaly increases further with depth to more than 250 Ω·m.

ERT anomaly 2 on the ERT profile 5 as interpreted, is "man-made" in origin and is caused by seepage rainwater, run-off, water conveyed by roads and ditches and the water drainage system into subsurface, at the toe of the landfill via vertical and horizontal pathways.

MASW data set 5 was acquired along the ERT traverse 5 at the 500 ft tie point. Shear-wave velocity of the soil in the study area, as interpreted, is < 1250 ft/s, and the shear-wave velocity for the soft or weathered rock, as interpreted is > 1250 ft/s (Figure 5.8).

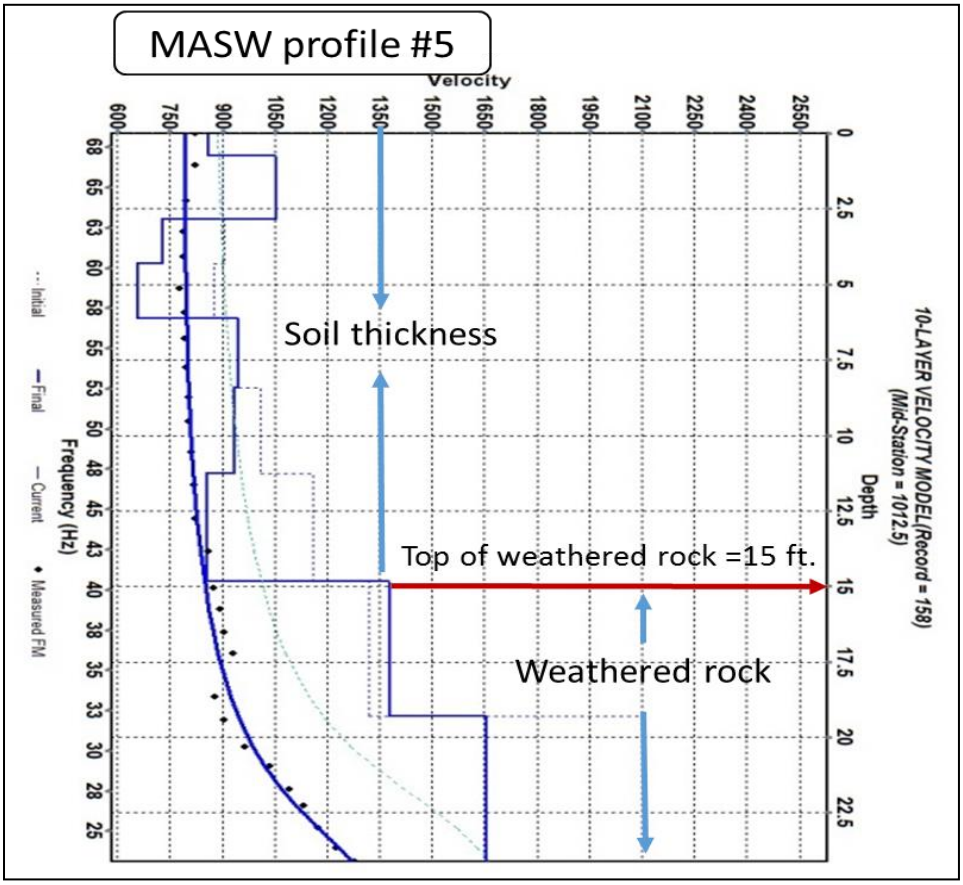

Figure 5.8. MASW shear-wave velocity profile 5 illustrating soil thickness, depth to top of weathered rock and weathered rock. Velocity is in ft/s.

At the tie point, the soil thickness as interpreted on the ERT profile 5 is ~20 ft. The soil thickness (depth to top of weathered rock) as interpreted on the MASW shear-wave velocity profile is ~15 ft. The difference between the ERT and MASW estimates of depth to top-of-rock can be attributed to the fact that the ERT estimate is based on moisture

content (resistivity) whereas the MASW estimate is based on shear strength (shear wave velocity). Also, the MASW data were acquired using a 115 ft long array of geophones. As a result, the MASW shear wave velocity profile represents the average shear wave velocity of the subsurface beneath the array of geophones as opposed to representing the shear wave velocity of the subsurface precisely at the tie point.

ERT Example 6:

ERT profile 6 is north-south oriented (Figure 5.1 & Figure 5.9). The superposed black solid line is the approximated top-of-rock, and generally considered to correspond to the 125 Ω·m contour interval.

The ERT anomaly on the ERT profile 6, which underlies a landfill, is ~ 775 ft wide at a depth of 42 ft (elevation 1180 ft) from the top-of-rock (elevation 1222 ft). The anomaly slightly broadens to ~790 ft at a depth greater than ~90 ft (elevation 1128 ft) from the top-of-rock, with a length of more than 52 ft for the anomaly. The base of the anomaly (as defined by the 125 Ω·m contact) is not observed on Figure 5.9, so the maximum depth of the anomaly cannot be determined. The minimum resistivity values (~10 Ω·m) associated with the anomaly, decrease with depth and are observed at a depth of ~80 ft (elevation 1142 ft) from the top-of-rock. Generally, resistivities of the anomaly range between 10 and < 125 Ω·m (Figure 5.9).

The anomaly underlies a landfill, which is by design, is comprised, in part, of an emplaced clay layer to prevent the leachate from contaminating subsurface soil and groundwater. Landfills are covered by a thin veneer of clayey soil and grass designed to divert rainwater run-off into a designed drainage system. The drainage system around this landfill is clay lined and designed to divert water into the drainage pathway at the toe of

the landfill. Some of the water in the drainage ditch seeps into the subsurface. Run-off from the landfill also seeps into the surface through the native soil near the toe of the landfill.

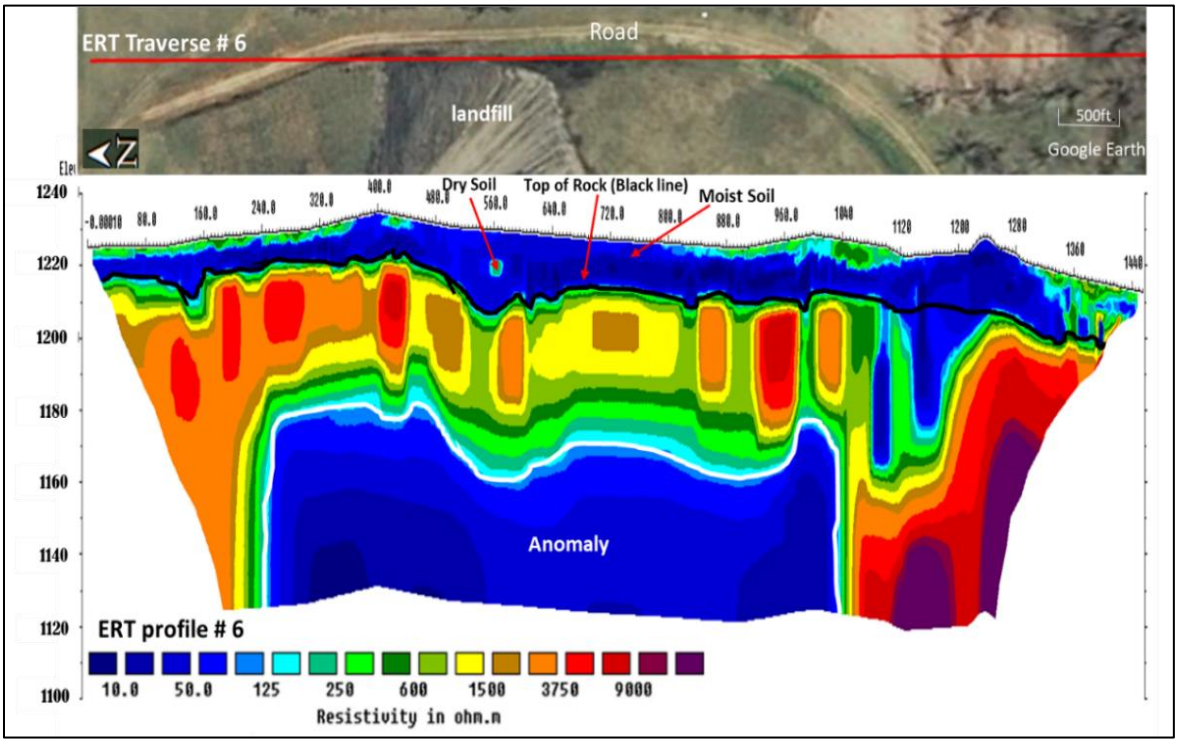

Figure 5.9. Google Earth image superposed upon the ERT profile 6 where water diverted by the landfill drainage system seeps into subsurface through pervasively fractured limestone rock. The anomaly slightly broadens below the 1180 ft elevation.

It's likely the upper subsurface rock is less conductive than the lower subsurface rock (below elevation 1180), since landfills are placed in locations with minimum porosity to avoid leachate escape into subsurface.

The ERT anomaly on the ERT profile 6 is "man-made", attributed to seepage of diverted water off the toe of the landfill by the designed water drainage system. Water seeps into subsurface via the natural vertical and horizontal pathways at the toe of the landfill (Figure 5.9).

ERT Example 7:

ERT profile 7 is west–east oriented (Figure 5.1 & Figure 5.10). The superposed black solid line is the interpreted top-of-rock and corresponds approximately to the 125 Ω·m contour interval.

ERT anomaly 1 on the ERT profile 7 is approximately 20 ft. wide at depth 76 ft (elevation 1117 ft) from the top-of-rock (elevation 1193 ft). The anomaly broadens to 35 ft wide at a depth greater than 86 ft (elevation 1107 ft) from the top-of-rock, with a length for the anomaly of more than ~10 ft. The base of the anomaly, as defined by the 125 Ω·m contact, is not observed on Figure 5.10, so the maximum depth of the anomaly cannot be determined. Resistivity values of ERT anomaly 1 on the ERT profile 7, as interpreted, decreases with depth of burial to resistivity values less than 125 Ω·m (elevation < ~1117 ft) from the interpreted top-of-rock. The minimum resistivity values are > 125 Ω·m at a depth of ~76 ft (elevation 1117 ft) from the interpreted top-of-rock (Figure 5.10).

ERT anomaly 1 on the ERT profile 7 as interpreted, is "natural" in origin, and attributed to seepage water and piped clay vertically into subsurface from the sinkhole. This sinkhole is likely formed during thousands of years (since ice age). North of the sinkhole is likely the initial location where water and clay material seeped into the subsurface and caused the sliding of the overburden. The subsurface water flow and clay has likely caused the creation of the cover collapse sinkhole. Anomaly 1 on the ERT profile 7, as interpreted (resistivity ~125 Ω·m), is caused by seepage water of the sinkhole, which percolate porous and fractured subsurface limestone rock. Soil thickness, as interpreted on the ERT profile 7 was 11 ft, and the top-of-rock (black line) was 11 ft. The minimum and maximum soil thickness varies between 5 and 35 ft. respectively.

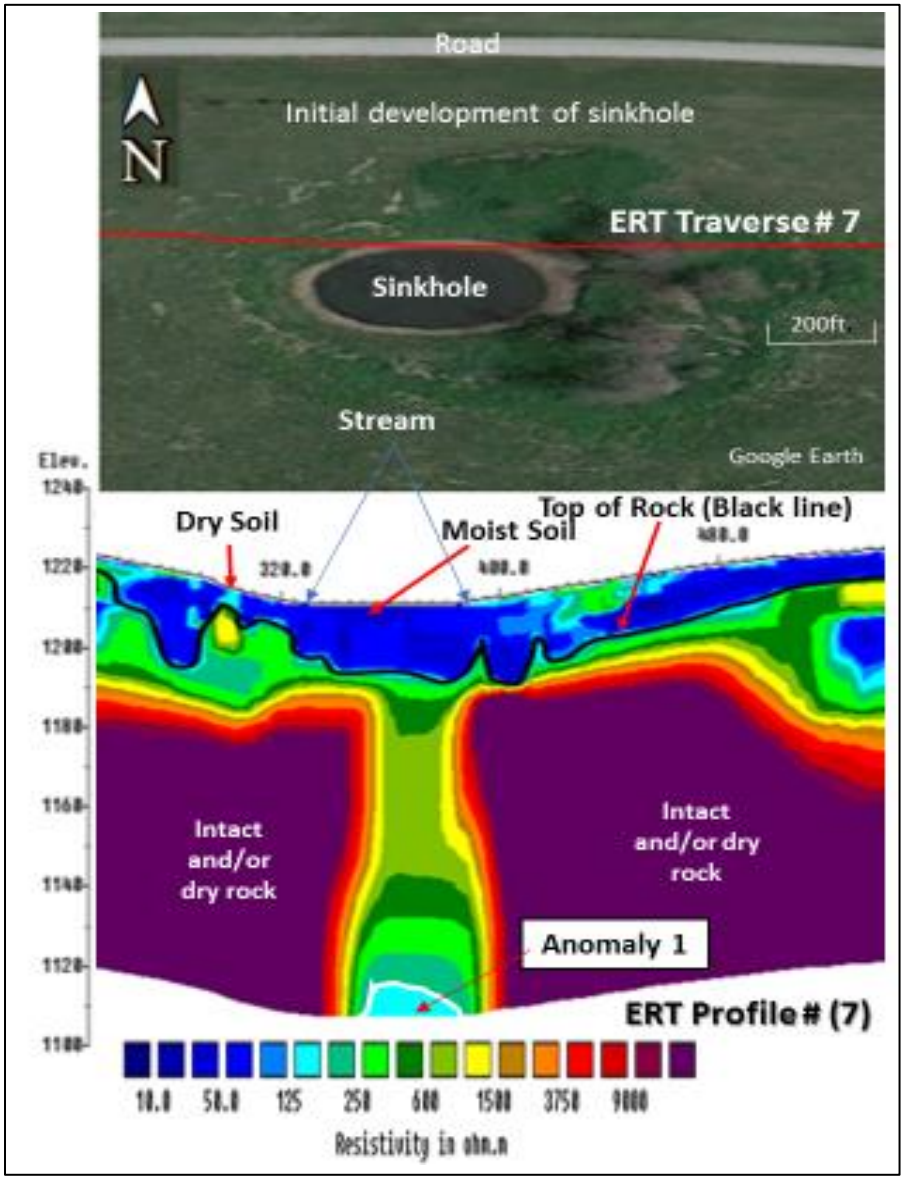

Figure 5.10. Google Earth image superposed upon the ERT profile 7 where the collected water in the sinkhole seeps to subsurface as shown in the figure with the corresponding anomaly 1 on the ERT profile.

Based on the discussion and interpretation of the seven (7) ERT profile examples of the study, Table 5.3 summarizes the “man-made” and the “natural” in origin anomaly characteristics.

The upper width is the anomaly width at the top-of-rock and the lower is the width at the bottom of the anomaly.

The depth of the anomaly is measured from the top-of-rock or from where the anomaly starts beneath the top-of-rock to the bottom of the anomaly, provided that the anomaly is not open ended.

The minimum anomaly resistivity value is the least value interpreted and the maximum is the highest resistivity values range.

The size of the anomaly is roughly estimated by the cross-sectional area of the anomaly (length x width).

The time span of the anomaly, is the interpreted time of the anomaly formation, considering that the anthropogenic activities in the study area are likely existed since ~ 50 years ago, whereas the natural anomalies has existed for thousands of years.

Hypotheses:

1- Natural in origin anomalies are larger in size than man-made anomalies.

2- Natural in origin anomalies are deeper in depth than man-made anomalies.

3- Man-made anomalies are narrower than natural in origin anomalies.

4- Man-made anomalies exist in ~50 years and the naturally occurred anomalies existed in 1000's of years.

Previous studies characterized the study area as intensively weathered, fractured and jointed carbonate rocks area, and have high tendency to absorb surface moisture from natural or anthropogenic sources.

Hypothetically, the "natural" in origin anomaly size and moisture is larger than the anthropogenically induced anomalies but as illustrated in example 7 (Table 5.3), it is likely that the seepage of water and clay into subsurface minimize the porosity and in-fill the fractures and eventually less moisture and piped clay reach deeper into subsurface.

Human intervention in many situations caused the creation of sinkholes and the creation of anomalously low resistivity values by the controlled water drainage systems for the roofs of houses and buildings and domestic water supply networks and road ditches and drainage systems of landfills.

Naturally formed anomalies in this study are mostly created due to stream beds. These anomalies usually existed during thousands of years and are hypothetically deeper, but in this study, as example 6 illustrates, man has disturbed the natural water flow direction by constructing roads in three (3) directions, that has resulted in a lateral spread of anomalously low resistivity values (Table 5.3).

Since natural anomalies in these examples, as interpreted, underlies stream beds, its width is controlled by stream banks, rainfall intensity and the soil amount and type. Soil particles settles on the surface forcing water to flow over stream banks, such as anomaly 1of example 1, example 2 and example 3. In these examples the anomalies are very large at the top and decreases with depth. The man-induced anomalies are generally small such as the anomalies associated with roads (anomaly 1 & 2, example 5). When water flow in pre-fractured and dry subsurface, naturally the in-filled soil absorb water very fast. These anomalies are usually narrower, but they grow larger if the joint is not large as in the case of example 4, in which man activity caused the expansion of the upper layer.

The extended time span (thousands of years), causes wide spread of moisture and increase in the anomaly size, as illustrated in example 1, 3 and 7; unlike the man-made, which have limited effect. The effect could increase through time and could cause the formation of sinkholes in these areas provided the increase in rainfall and the existence of bad drainage.

Table 5.3. Man-made and natural in origin anomaly characteristics

Elements of anomaly comparison	Example 1		Example 2	Example 3	Example 4	Example 5		Example 6	Example 7
	Anomaly 1	Anomaly 2				Anomaly 1	Anomaly 2		
Width (upper/lower), ft	85/50	50/0	70/40	20/40	15/80	35/60	50/40	775/790	20/35
Depth, ft	18	14	20	62	>90	>70	38	>52	>10
Resistivity (min/max) Ω·m	75/125	25/50	100/125	75/150	10/50	25/75	50/75	10/125	<125/>125
Size, sq.ft	~900	~260	~1100	~1200	>3,500	>3,200	~1520	>35,500	>200
Time span (years)	1000s	~50	1000s	1000s	~50	~50	~50	~50	1000s
Cause of the anomaly (anthropogenic/natural)	natural	man-made	natural	natural	man-made	man-made	man-made	man-made	natural

6. CONCLUSIONS

The primary objective of the research was to determine the cause of identified zones of high moisture content within bedrock and to differentiate anomalously conductive zones that were mostly “man-made” from those that were mostly of “natural” origin. Field observations and air photographs were used for this purpose.

Herein, seven ERT profiles are presented. Five of the low resistivity bedrock anomalies identified on these ERT profiles are classified as primarily “man-made”; the other 4 are classified as primarily “natural” in origin. ERT anomalies that can be attributed to natural causes, such as water-filled sinkholes and surface drainage pathways were differentiated from anomalies that were caused by man-made factors (attributable to surface features such as drainage ditches, gravel lots, and the engineered drainage systems around landfills). Based on the assessment of the entire ERT data set, it is concluded that there are no significant statistical differences between the ERT signatures of the “man-made” and “natural” zones of high moisture content. Determinations about the cause of low resistivity zones identified on ERT data is best done based on field observations and air photographs.

The study formulated four hypotheses about the natural and man-made anomalies in terms of the anomaly size, depth, the time span it took to create and width. These hypotheses could be a future research subject to cover the entire region.

REFERENCES

1. Al Saaideh, A. S. (2017). “Imaging a Fly ash Landfill Using non-invasive technologies (ERT and MASW)”, PhD, Missouri University of Science and Technology.

2. Alfuqara, D. A. A. (2017). "2-D and 3-D mapping of soil and rock structure in karst terrain of southwestern Missouri using the non-invasive electrical resistivity tomography method (ERT)".

3. Anderson, Neil, lecture notes, 2017.

4. Anderson, Neil, 2016, unpublished report.

5. Anderson 2015.

6. Anderson, N. L. (2006). "Interpretation of Electrical Resistivity and Acoustic Surface Wave Data Acquired at Nixa Sinkhole Study Site." unpublished report for SCI Engineering.

7. Bansah, K. and N. Anderson (2017). Factors Contributing to Karst Development in Southwestern Missouri, USA. SAGEEP 2017-30th Annual Symposium on the Application of Geophysics to Engineering and Environmental Problems.

8. Bansah, K. and N. L. Anderson (2017). Multichannel Analysis of Surface Waves: Estimating Depth to Bedrock and Acoustic Properties in Karst Terrain. 51st US Rock Mechanics/Geomechanics Symposium, American Rock Mechanics Association.

9. Bansah, K. J. and N. L. Anderson (2018). Mapping Subsurface in Karst Terrain Using 2-D Electrical Resistivity Tomography. Symposium on the Application of Geophysics to Engineering and Environmental Problems 2018, Society of Exploration Geophysicists and Environment and Engineering.

10. Bashir et al., 2018 Application of Multi-Channel Analysis of Surface Waves Method to Determine Optimum Parameter Settings in Karst Terrain in Southwest Missouri, Jan 2018 International Journal of Science and Research (IJSR).

11. Callister Jr, William D. Fundamentals of Material Science and Engineering. New York: John Wiley and Sons, Inc., 2001. 15.16.

12. El Aal, A. A. (2017). "Identification and characterization of near surface cavities in Tuwaiq Mountain Limestone, Riyadh, KSA, “detection and treatment”." Egyptian Journal of Petroleum 26(1): 215-223.

13. Environmental Protection Agency, 2018.

14. Gathers Julian Ivanov*, Choon B. Park, Richard D. Miller and Jianghai Xia, JEEG, September 2005, Volume 10, Issue 3, pp. 307–322)

15. Gibson, Paul J, and Dorothy M George. Environmental Applications of Geophysical Surveying Techniques. Hauppauge: Nova Science Publishers, 2003.

16. James W. Duley, John W. Whitfield, Ardel W. Rueff and James E. Vandike, "Geologic and Hydrologic Resources of Laclede County, Missouri, open file Report," 1992.

17. Ivanov, Julian, Choon Park, and Jianghai Xia. "MASW/SurfSeis 2 Workshop." Fort Worth: Kansas Geologic Survey, March 28, 2009.

18. Kansas Geological Survey.

19. Kidanu, S. T., et al. (2018). "Using GIS - based Spatial Analysis to Determine Factors Influencing the Formation of Sinkholes in Greene County, Missouri." Environmental & Engineering Geoscience 24(3): 251-261.

20. Kidanu, S. T., et al. (2016). "ERT-based Investigation of a Sinkhole in Greene County, Missouri." AIMS Geosciences **2**: 99-115.

21. Marescot, L., and M. H. Loke, 2004, "Using the depth of investigation index method in 2D resistivity imaging for civil engineering surveys: Proceedings of the Symposium for the Application of Geophysics to Environmental and Engineering Problems", Environmental and Engineering Geophysical Society, 589595.

22. Middendorf, M. A., Thomson, K.C., Eason, G.L., and summer, H.S., 1987, Bedrock geologic map of the Springfield 1 degree * 2 degrees quadrangle, Missouri: U.S. Geological Survey, Miscellaneous Field Studies Map MF-1830-D.

23. Missouri Department of Natural Resources, 2007.

24. Missouri Department of Natural Resources web site.

25. NEHRP, 1997, (National earthquake hazards reduction program).

26. Nwokebuihe, S. C. (2014). "The description of an effective sinkhole investigation approach: a case study of two sites in Greene County, Missouri."

27. Obi, Jeremiah Chukwunonso, "Geophysical Imaging of Karst Features in Missouri" (2016), Doctoral Dissertations, 2485 (https://scholarsmine.mst.edu/doctoral_dissertations/2485).

28. Palacky, G. (1988). "Resistivity characteristics of geologic targets." Electromagnetic methods in applied geophysics **1**: 53-129.

29. Parasnis, D.S. (1997) Principles of Applied Geophysics. Chapman & Hall, London.

30. Park, C.B. 2006. Active and passive MASW, seismic processing software for use with Microsoft windows, supplementary user's manual, v 2.0, Kansas Geological Survey.

31. Park, C. B., R. D. Miller, N. Ryden, J. Xia, and J. Ivanov, 2005, Combined use of active and passive surface waves: Journal of Environmental and Engineering Geophysics, 10, 323-334.

32. Park, C.B., Miller, R.D., and Miura, H., 2002, Optimum field parameters of an MASW survey [Exp. Abs.]: SEG-J, Tokyo, May 22-23, 2002. (PAR-02-03)

33. Porter, James, and Thomson, Kenneth, 1975. Geology, Geomorphology and Karst Development in the Nixa Karst Area, Southwestern Missouri. Geoscience Series No. 1, Department of Geography & Geology, Southwest Missouri State University, 46 pages.

34. Sharma, P. (1997)." Environmental and engineering geophysics", Cambridge University Press, Cambridge, U.K.

35. Society of Exploration Geophysicist of Japan. Application of Geophysical Methods to Engineering and Environmental Problems. Tokyo: Society of Exploration Geophysicist of Japan, 2004.

36. Van Der Hilst, Robert. "Chapter 4: Seismology." MIT Open Course Ware. 2004. http://ocw.mit.edu/NR/rdonlyres/Earth--Atmospheric--and-Planetary-Sciences/12-201Fall-2004/4813C5AE-9A5F-4440-8A49 39559A713D67/0/ch4.pdf (accessed October 25, 2009).

37. Vandike, J. E. (1993). Groundwater Level Data for Missouri: Water Year 1991-1992, Missouri Department of Natural Resources.

38. Veni, G. and Hauwert, N. (2015). Historical review and forward view of cave and karst research in Texas, in Feinberg, J., Gao, Y. and Alexander, E.C., Jr., eds. Caves and karst Across Time: Geological Society of America Special paper 516 p. 49-66, doi: 10.1130/2015.2516(05)

39. Wightman, W., et al. (2004). Application of geophysical methods to highway related problems.

40. Youssef, A. M., et al. (2016). "Natural and human-induced sinkhole hazards in Saudi Arabia: distribution, investigation, causes and impacts." Hydrogeology Journal 24(3): 625-644.

41. https://archive.epa.gov/esd/archive-geophysics/web/html/resistivity_methods.html.

42. http://augustacountyalliance.org/wp-content/uploads/2014/09/Augusta-County-Karst-101.pdf).

43. https://dnr.mo.gov/ Missouri Department of Natural Resource.

44. http://geophysicalservices.com/electrical-resistivity-tomography-imaging-supersting-ohmmapper-032517/.

45. http://geophysicalservices.com/masw-surveys-acquisition-data-processing-interpretation-091717/

46. https://www.google.com/url?sa=i&rct=j&q=&esrc=s&source=images&cd=&ved=2ahUKEwj46uWK6NzmAhUDHqwKHfiOAU0QjB16BAgBEAM&url=https%3A%2F%2Fwiki.seg.org%2Fwiki%2FElectric_resistivity_surveys&psig=AOvVaw05Ie3-xfkmI3r8QGV-EyEu&ust=1577775666997755, SEG wiki-SEG.org.

47. http://gotbooks.miracosta.edu/geology/images2/ozarks.jpg.

48. http://www.masw.com/DataAcquisition.html.

49. http://www.mdc.state.mo.us/nathis/natcom/natdiv/.

50. http://old.acogok.org/geophysical-tutorial.

51. https://www.researchgate.net/publication/228977208_MASW_horizontal_resolution_in_2D_shear-velocity_Vs_mapping/figures?lo=1" Overall procedure for the 2-D shear-wave velocity map with the MASW survey".

52. http://upload.wikimedia.org/wikipedia/commons/a/a1/Missouri_Geology Primary_Rock_Types_v1.png).

53. https://water.usgs.gov/edu/sinkholes.html Cover-subsidence sinkhole.

VITA

Hassan Abdullah Ahmed Alzahrani was born in Albaha, Saudi Arabia. He received his Bachelor of Science degree in mathematics at King Saud University, Riyadh, Saudi Arabia in 1999. Alzahrani completed a pre-master requirement course in geophysical applications at King Saud University, 2006.

Alzahrani received a master's degree in Geophysical Applications at the Department of Geology and Geophysics of King Saud University, Riyadh, Saudi Arabia in 2016, and joined the department as a faculty member.

In 2016, Alzahrani joined the PhD program in Geological Engineering at Missouri University of Science and Technology, Rolla, Missouri.

Alzahrani became a member in Saudi Society for Geosciences (SSG) in 2006, and the (AGU) and (SSA) since 2016 and has participated in the American Geophysical Union (AGU) conference of 2017, New Orleans, USA and the Seismological Society of America (SSA) conference of 2018, Miami, FL.

Alzahrani obtained a second master's degree in Geological Engineering at Missouri University of Science and Technology in December 2018 and a PhD degree in Geological Engineering from the same university in May 2020.